Atkinson, Oliver (2024) *Particle physics phenomenology at the LHC and beyond.* PhD thesis.

Particle Physics Phenomenology at the LHC and beyond

Oliver Atkinson
Supervised by Prof. Christoph Englert & Dr. David Miller

Submitted in fulfilment of the requirements for the degree of
Doctor of Philosophy

School of Physics and Astronomy
College of Science and Engineering
University of Glasgow

Abstract

The prevailing paradigm of particle physics, the Standard Model, has proven to be superbly successful since its inception, but cracks are beginning to show and plenty of phenomenological challenges have presented themselves. This thesis takes a few approaches to the study of particle physics phenomenology, using both model dependent and model independent frameworks. New states in the Higgs sector are introduced and studied first in the context of their interference patterns in the top quark sector, and then the two Higgs doublet model is examined in the face of a vast array of current and future collider searches, flavour observables, and theoretical and cosmological considerations. Machine learning techniques are applied to the Standard Model effective field theory framework to show how future colliders may be better able to constrain models of new physics, and through the use of graph neural networks, be able to pick out anomalous events from the large background of collider environments.

Acknowledgements

As it transpires, a doctorate in theoretical particle physics is no mean undertaking. Beginning such an undertaking in the midst of the worst pandemic the world has seen in the past century could only add to the thorny nature of such a task. And yet, here I submit a completed thesis, after years of research and hard graft, in the hopes of attaining a doctorate. Even if this does not result in success and the accompanying anointment, I am and will remain proud of my endeavours over the past few arduous years. I will always be able to say *I did this.*

Of course, to stress the "*I*" would be entirely disingenuous. As John Donne once wrote, no man is an island. Perhaps there is nowhere that this rings truer than in the pursuit of a PhD, in the spheres of both work and personal lives. There can be no doubt in my heart that I would never have reached this point without the relentless support of so very many people, all of whom I am incredibly lucky to have in my life, and will forever be grateful to.

Naturally, my supervisor Christoph Englert is first in my thoughts in this regard. Quite simply, without him, none of this would have been remotely possible. His depth of enthusiasm and passion for the subject matter is matched perhaps only by his knowledge. I feel incredibly lucky to have had such a wonderful person and physicist guide me through the past few years. I've also been fortunate to benefit from the experiences and advice of those who came before me; Panos and Will in particular. I hope that I have been half as useful to Kerr, Logan, Alastair and of course Wrishik in the early stages of their postgraduate studies. Akanksha and Anisha have always made the group a warm and kind place, as well as making invaluable contributions to our collaborations. Chris Bouchard, David Miller and latterly Sophie Renner and David Sutherland deserve credit for driving fascinating and important research, making the group a rich and vibrant place.

Each one of my collaborators has my deepest thanks for the hours they spent on our projects and

for the pleasure of working alongside them. Particular thanks in this regard must go to Alexander Lenz, Aleksey Rusov and Matt Black, with whom I spent several years working closely with on a series of ever more comprehensive studies of the Two Higgs Doublet Model.

Beyond the immediate circle of my collaborators and fellow department members, there are so very many wonderful people in my life. I am not at all a religious or spiritual person, but I do feel truly blessed by their presence in my life. Not all of them have been around the whole time, but all have had such a bearing on my life and my progress over the past few years that it would be remiss, bordering on rude, not to acknowledge them here. For their constant and unwavering love and support, my Dad, Mum and sister Holly have my eternal deep gratitude. Of my friends, Sam, Jake and Eddie deserve a mention for the fun and distraction they've provided, as do Abdullah, Lizzie, Ed and Maryam for, at various points, putting up with my semi-coherent ramblings and assorted foibles. I could likely write a thesis on what these people mean to me, but that falls somewhat outside the scope of this work, so a simple and heartfelt thank you will have to suffice.

I additionally acknowledge support from the Science and Technology Facilities Council (STFC).

Declaration of Originality

The material presented in this thesis is the result of my own work and research as part of the Particle Physics Theory group of the School of Physics and Astronomy at the University of Glasgow. The primary exception to this is the well established introductory material presented in Chapter 2. Otherwise, the chapters are based on the following publications, with many of the figures shown here reproduced from these works:

Chapter 3: *"On interference effects in top-philic decay chains"* [1], written in collaboration with Prof. Christoph Englert and Dr. Panagiotis Stylianou.

Chapter 4: *"Cornering the Two Higgs Doublet Model Type II"* [3], *"The flavourful present and future of 2HDMs at the collider energy frontier"* [5] and *"MUonE, muon g-2 and electroweak precision constraints within 2HDMs"* [7], written in collaboration with Mr. Matthew Black, Prof. Christoph Englert, Prof. Alexander Lenz, Dr. Aleksey Rusov and Mr. James Wynne.

Chapter 5: *"Improved constraints on effective top quark interactions using edge convolution networks"* [4], written in collaboration with Dr. Akanksha Bhardwaj, Prof. Christoph Englert, Mr. Stephen Brown, Dr. David Miller and Dr. Panagiotis Stylianou.

Chapter 6: *"Anomaly detection with convolutional Graph Neural Networks"* [2] and, to a lesser extent, *"IRC-Safe Graph Autoencoder for Unsupervised Anomaly Detection"* [6], written in collaboration with Dr. Akanksha Bhardwaj, Prof. Christoph Englert, Prof. Partha Konar, Dr. Vishal S. Ngairangbam and Prof. Michael Spannowsky.

We shall not cease from exploration
and the end of all our exploring
will be to arrive where we started
and know the place for the first time.
T.S. Eliot

Contents

List of Figures

List of Tables

Chapter 1

Introduction

There have been but few constants in the messy and millennia long history of our species, and fewer still that have continued to and indeed flourished in modern times. The will and urge to craft narratives to explain the bevy of natural phenomena that surround us is one such steady constant. From Gods and demons to ethers and ill humours, humanity has slowly and steadily demystified the cosmos. Of course, a thing is no less beautiful, no less majestic, by dint of being understood.

Perhaps this crusade is driven by some knowledge that lies deep inside each of us, that we have but a brief time upon this mortal coil, and we desire to leave some trace that lingers long beyond the ephemeral span of our years. In this we are no different to the pharaohs of old, and as such we are subject to the same follies, for in time the lone and level sands will claim and consume all that we are and all of our works. Physics is no different in this; the times change and ideas shift and switch, now one and now the other. The long march of history is marked by revelations upon revolutions, each upending the established order in a feverish blaze of the new.

At least, that's how it appears when casting our eyes back over the storied history of the field. Truthfully, progress has often been halting and gradual, a slow burn that is occasionally punctuated by paradigm shifts that rise out of decades of work by countless dedicated physicists and sometimes out of sheer good fortune.

For my part, over the past few years I have been part of a group working on the theoretical elements of particle physics, and my work [1–9] has centred around the phenomenology at the

Large Hadron Collider (LHC) and models of new physics (NP) in particular. In this thesis, I present some of this work.

After introducing the current paradigm of particle physics in Chapter 2, specific models of new physics are studied; Chapter 3 examines an addition of two singlet states and the role interference effects can play in the detection capability of their cascade decays, while Chapter 4 puts the two Higgs doublet model under the microscope using a vast collection of data. Moving to more general approaches, and motivated by the opportunities presented by novel machine learning techniques, effective field theories are the subject of Chapter 5, and the possibility of using autoencoders to uncover anomalies is outlined in Chapter 6. Things are brought to a close in Chapter 7.

Chapter 2

The Standard Model of Particle Physics

Our current understanding of the Universe can broadly be divided into two pillars, each painstakingly constructed over the past century. We need not concern ourselves with one of these pillars, that of General Relativity and the prevailing cosmological model built with that work of genius at its core. Instead, the work of this thesis rests on the other major pillar, the one that deals with the smallest of scales.

It seems passing queer that such a feat of human imagination and ingenuity, relentlessly tested and refined over decades with some of the largest scale collaborations ever seen, should come to bear the inspired moniker of the Standard Model (SM). Nonetheless, this is the model that represents the forefront of our understanding of the most fundamental constituents of the Universe and has held up under the scrutiny of some of the most precise experiments ever designed. Despite this stunning success, the SM does not represent a full comprehension of all known phenomena and it is important to first acknowledge and then attempt to address these limitations, in the hope of moving toward a more complete model. Again, the naming convention is imaginative, with models that go beyond the SM typically referred to as Beyond Standard Model (BSM) models.

This section will set out the basis of the SM, primarily focusing on the theoretical aspects and background, whilst also highlighting salient experimental measurements. This will encompass the Lagrangian formulation of the SM, with emphasis on the Higgs mechanism and the related couplings of fermionic matter. This component of the SM is of particular relevance in my thesis as much of my work has involved either extensions of the Higgs sector or interactions that stem from this sector.

On the experimental side, the numerous successes of the SM will be outlined, many of which demonstrate superb levels of precision and agreement with the SM. Of course, the SM does not answer all questions about the fundamental nature of the Universe, and we see this in several experimental measurements, in addition to a series of conceptual arguments. Extra emphasis will be placed on the anomalies which feature a number of times across my body of work, such as the anomalous magnetic moment of the muon, to ensure that the reader has the proper context when such observables are levied to investigate models of new physics. Much pedagogical literature exists on the SM, and in this chapter the presentation in Ref. [10] is broadly followed.

The SM is a quantum field theory which describes the nature and interactions of all known particles. It is in part a Yang-Mills theory [11], which is to say it is a form of non-Abelian gauge field theory which is inherently renormalisable [12, 13]. This is a key requirement of any gauge field theory that can have testable physical consequences as it must be free from the infinities in calculations that plagued theorists for much of the twentieth century. The particle content of this model consists of 12 fermions (three families each comprising a positively charged quark, a negatively charged quark, a negatively charged lepton and a corresponding neutral neutrino) and four vector bosons that mediate the forces of the SM (two for the weak force, one each for the strong force and electromagnetism) and a single scalar boson, the Higgs. The Lagrangian of the theory can be symbolically split into four parts, each of which describes a distinct element of the theory and will be outlined herein:

$$\mathcal{L}_{\text{SM}} = \mathcal{L}_{\text{Gauge}} + \mathcal{L}_{\text{Fermions}} + \mathcal{L}_{\text{Yukawa}} + \mathcal{L}_{\text{Higgs}}. \tag{2.1}$$

Expanding each of these elements to their own line and using the standard notation of $F^{\mu\nu}$ for a field strength tensor, D_μ for a covariant derivative, ψ for a fermionic field, Φ for the Higgs field and Y it's couplings yields the more familiar form of the SM Lagrangian, which can be found adorning mugs and t-shirts the world over:

$$\begin{aligned}\mathcal{L} = &-\frac{1}{4}F^{\mu\nu}F_{\mu\nu} \\ &+ i\bar{\psi}\not{D}\psi \\ &+ \bar{\psi}_{L_i}Y_{ij}\Phi\psi_{R_j} + h.c. \\ &+ |D_\mu\Phi|^2 - V(\Phi).\end{aligned} \tag{2.2}$$

2.1 Gauge Field Theories

The first two components of the SM Lagrangian comprising the gauge and fermionic parts of the theory can be grouped together and explained through Abelian and non-Abelian gauge theories. Here Abelian gauge theories are introduced through quantum electrodynamics (QED) whilst the non-Abelian side of things is illustrated by quantum chromodynamics (QCD). As a brief rundown of some pertinent concepts of group theories, note that the set of $N \times N$ unitary matrices with the group operation of matrix multiplication is denoted as $U(N)$, whilst additionally demanding that the matrices have unit determinants yields the special unitary group $SU(N)$. Impressing upon the fields the requirement of invariance under some local, or gauge, transformation, leads to the rich phenomenological maelstrom of the SM.

2.1.1 Quantum Electrodynamics

The simplest physically relevant theory one can construct in this formalism is QED, for which only two particles are required; an electron ψ and a photon A_μ. To begin construction of a gauge invariant Lagrangian, one must first define some gauge transformation, parameterised by $\alpha(x)$, along with some arbitrary coupling g, yielding $\psi \to e^{ig\alpha(x)}\psi$. Note that in this case, one can cutely point out that the gauge transform $e^{ig\alpha(x)}$ is equivalent to the action of a 1×1 unitary matrix – in other words, this is a demonstration of a $U(1)$ gauge theory. Given that such a matrix will clearly commute with itself, we are dealing with an Abelian gauge field theory here.

A complication arises when one attempts to introduce kinetic terms into the Lagrangian of such a theory, as to do so invokes forms such as $\partial_\mu\psi$, which will not be invariant under the gauge transform. To overcome this issue, the covariant derivative is introduced;

$$D_\mu = \partial_\mu - igA_\mu, \tag{2.3}$$

from which one derives the transformation of the gauge field: $A^\mu \to A^\mu - \frac{1}{g}\partial^\mu \alpha(x)$. Crucially, we have now coupled the gauge field to the fermion field, thereby giving rise to interaction terms between the two. In order to ensure the gauge fields are true dynamical fields, one must also bestow upon them kinetic terms, which is done via the field strength tensor $F_{\mu\nu} = \partial_\mu A_\nu - \partial_\nu A_\mu$, which is pulled from the commutator of the covariant derivative. Combining all the terms for the electron of mass m and the massless photon we arrive at the QED Lagrangian,

$$\mathcal{L}_{\mathrm{QED}} = -\frac{1}{4}F^{\mu\nu}F_{\mu\nu} + \bar{\psi}(i\not{D} - m)\psi, \tag{2.4}$$

using the standard notation of $\not{D} = \gamma^\mu D_\mu$ and $\bar{\psi} = \psi^\dagger\gamma^0$. Hopefully some similarities to terms in the full SM Lagrangian of Eq. (2.2) are beginning to become apparent, even in this simplified version of a gauge field theory.

2.1.2 Quantum Chromodynamics

Moving beyond the simple $U(1)$ case of QED reveals a more vibrant set of interactions and underlying equations. Though much of the logic of QED can be applied to non-Abelian gauge field theories such as QCD [14–16], there are non-trivial changes that arise from the more complex nature of the group generators. As opposed to the scalar generator of $U(1)$, we now deal with a set of matrices T^a as the group generators. The group $SU(N)$ has in general $N^2 - 1$ generators, and thus the same number of degrees of freedom. These generators are subject to a standard normalisation convention of $[T^a, T^b] = if^{abc}T^c$, where f^{abc} is the antisymmetric structure constant. The local gauge transformation for a fermion then becomes $\psi \to U(x)\psi = e^{ig\alpha^a(x)T^a}\psi$, while there are now $N^2 - 1$ gauge fields A^a_μ, with $A_\mu = A^a_\mu T^a$.

Following the same logic as in the simple QED case, we look to find a covariant derivative that leaves the fermion kinetic terms invariant under the transformation. This takes the same form as in Eq. (2.3), but note that now A_μ has a number of independent components and transforms in the adjoint representation. This is also where we see the non-commuting properties of the group generators start to come into play. The transformation of the gauge fields can then be derived as

$$A_\mu \to A'_\mu = UA_\mu U^{-1} - \frac{i}{g}(\partial_\mu U)U^{-1}. \tag{2.5}$$

Suppressing the x dependencies of α^a for ease and writing this out in terms of components:

$$A'^a_\mu = A^a_\mu + \frac{1}{g}\partial_\mu \alpha^a - f^{abc}\alpha^b A^c_\mu. \tag{2.6}$$

As before, we look to define the field strength tensor from the commutator of the covariant derivative, and again the non-Abelian nature of the group makes itself known:

$$F^a_{\mu\nu} = \partial_\mu A^a_\nu - \partial_\nu A^a_\mu + g f^{abc} A^b_\mu A^c_\mu. \tag{2.7}$$

From $F^a_{\mu\nu}$ it should be noted that the kinetic term for the gauge fields in the Lagrangian, $-\frac{1}{4}F^{\mu\nu}F_{\mu\nu}$, will involve interaction terms between the gauge fields themselves, as a direct result of the non-Abelian nature of the group. In the Abelian case, all $f^{abc} = 0$ and QED, with its non self interacting photons, is immediately recovered.

As promised, QCD is a non-Abelian gauge theory, with the group $SU(3)$ at its core. The eight Gell-Mann matrices λ^a comprise the set of group generators; $T^a = \frac{1}{2}\lambda^a$, and so nature correspondingly obliges with eight gluons of varying colour-anticolour configurations. Following a mildly unclear convention, to distinguish the QCD field strength tensor it will herein be denoted as $G^{\mu\nu}$, whilst T^a and f^{abc} are locked in as those of $SU(3)$, with the strong force coupling being g_s. Collecting things together and ensuring that each of the flavours of quark is subject to this theory:

$$\mathcal{L}_{\text{QCD}} = -\frac{1}{4}G^{\mu\nu}G_{\mu\nu} + \sum_{f\in\{u,d,c,s,t,b\}} \bar{\psi}(i\not{D} - m_f)\psi. \tag{2.8}$$

2.2 The Electroweak Sector

One area left unaddressed so far is that of chirality. Experimental results revealed that the weak force is not only capable of violating parity, but does so with maximal effect [17], with only left-handed fermions interacting under the weak force. The fermion fields used thus far are split into their left- and right-handed components by use of projectors $P_{R/L}$, such that $\psi_{R/L} = P_{R/L}\psi = \frac{1}{2}(1 \pm \gamma_5)\psi$. The group we couch the weak force in is $SU(2)_L$, with the Pauli matrices ($\frac{1}{2}\sigma^a$) for generators, W^a_μ as the gauge fields and a coupling g. The right-handed fields transform as a singlet under this group, meaning that the mass terms seen in the above sections, which are of the form $m\bar{\psi}_L\psi_R$ will not be invariant under the $SU(2)_L$ transformation, owing to its chiral nature. This is not the only mass(ive) problem; the gauge bosons of the weak force themselves have non-zero masses, but the naive inclusion of a mass term such as $m^2 A_\mu A^\mu$ in the Lagrangian also breaks gauge invariance.

As long as things are already breaking, let's go a step further and, in a fit of spontaneity, break some symmetries. First, we need some symmetry to break; a unification of the weak and electromagnetic forces should suffice [18–20], yielding the group $SU(2)_L \times U(1)_Y$, where $U(1)_Y$ is a high energy symmetry known as hypercharge, with a single gauge field B_μ, scalar generator Y and coupling g'. The covariant derivative of this $SU(2)_L \times U(1)_Y$ group is therefore

$$D_\mu = \partial_\mu - \frac{i}{2} g W_\mu^a \sigma^a - iYg'B_\mu. \tag{2.9}$$

Now we can really start to break things, or as it has otherwise been termed, illustrate the mechanism by which masses are generated for the fundamental particles of the Universe, coming out with a unique scalar boson to boot. This is of course the Higgs mechanism, and said boson the Higgs boson, although the mechanism was independently discovered by a number of others at the same time [21–24]. To perform this symmetry breaking, we introduce a complex doublet of hypercharge 1/2, denoted by Φ and with a Lagrangian

$$\mathcal{L}_{\text{Higgs}} = (D_\mu \Phi)^\dagger (D^\mu \Phi) + \mu^2 \Phi^\dagger \Phi - \lambda (\Phi^\dagger \Phi)^2, \tag{2.10}$$

where the last two terms comprise the Higgs potential $V(\Phi)$. Critically, this potential has a non-zero minimum, when $|\Phi| = \frac{\mu}{\sqrt{2\lambda}} = v/\sqrt{2}$, defining v as the vacuum expectation value (VEV). Thus we have [21]

$$\Phi = \frac{1}{\sqrt{2}} \begin{pmatrix} 0 \\ v+h \end{pmatrix}, \quad \langle \Phi \rangle = \frac{1}{\sqrt{2}} \begin{pmatrix} 0 \\ v \end{pmatrix}. \tag{2.11}$$

Expanding the covariant terms of Eq. (2.10) and, for now, discarding the h field terms yields

$$\begin{aligned} (D_\mu \Phi)^\dagger (D^\mu \Phi) \ni \frac{g^2}{8} \begin{pmatrix} 0 & v \end{pmatrix} &\begin{pmatrix} \frac{g'}{g} B_\mu + W_\mu^3 & W_\mu^1 - iW_\mu^2 \\ W_\mu^1 + W_\mu^2 & \frac{g'}{g} B_\mu - W_\mu^3 \end{pmatrix} \begin{pmatrix} \frac{g'}{g} B_\mu + W_\mu^3 & W_\mu^1 - iW_\mu^2 \\ W_\mu^1 + W_\mu^2 & \frac{g'}{g} B_\mu - W_\mu^3 \end{pmatrix} \begin{pmatrix} 0 \\ v \end{pmatrix} \\ = \frac{g^2 v^2}{8} &\left((W_\mu^1)^2 + (W_\mu^2)^2 + \left(\frac{g'}{g} B_\mu - W_\mu^3 \right)^2 \right). \end{aligned} \tag{2.12}$$

These are mass terms for three gauge bosons, which were previously not possible. To attain physical mass eigenstates of these bosons, we perform a rotation parameterised by the Weinberg angle θ_{w} such that $\tan\theta_{\mathrm{w}} = \frac{g'}{g}$ [19]:

$$\begin{pmatrix} A_\mu \\ Z_\mu \end{pmatrix} = \begin{pmatrix} \cos\theta_{\mathrm{w}} & \sin\theta_{\mathrm{w}} \\ -\sin\theta_{\mathrm{w}} & \cos\theta_{\mathrm{w}} \end{pmatrix} \begin{pmatrix} B_\mu \\ W_\mu^3 \end{pmatrix}, \tag{2.13}$$

where we additionally define $W_\mu^\pm = \frac{1}{\sqrt{2}}(W_\mu^1 \mp iW_\mu^2)$ as the electrically charged weak bosons. Further cranking the mathematical handle, we can read off the masses of these four bosons after these redefinitions as

$$m_W = \frac{gv}{2}, \qquad m_Z = \frac{gv}{2\cos\theta_W} = \frac{m_W}{\cos\theta_W}, \qquad m_A = 0. \tag{2.14}$$

After this process of electroweak symmetry breaking (EWSB), the $W^\pm$ and Z bosons mediate the weak force, whilst we have recovered the massless photon A_μ of QED. From this we see that the electromagnetic coupling strength is set by $e = g\sin\theta_{\mathrm{w}} = g'\cos\theta_{\mathrm{w}}$, and then, from the covariant derivative, that the electric charge of a particle is given by $Q = Y + \frac{1}{2}\sigma^3$ [25, 26].

Whilst a massive gauge boson has three degrees of freedom, a massless boson has only two, so it appears that no fewer than three additional degrees of freedom have been created by symmetry breaking and the subsequent acquisition of mass by the weak bosons. In fact, the three non-physical degrees of freedom of the Higgs doublet become the longitudinal polarisations of the now massive vector gauge bosons, leaving only the single physical field in the Higgs doublet. Or, as it is often put, the gauge bosons have eaten the degrees of freedom of the Higgs doublet.

Returning to the Higgs Lagrangian of Eq. (2.10), this additional dynamical field h also has a mass term; $m_h = \sqrt{2}\mu$. This is the Higgs boson, the only known scalar boson and the last piece of the SM, finally discovered at the LHC in 2012, with a mass of 125 GeV [27, 28].

2.3 The Fermion Sector

This is all very well, but we are still yet to address the issue of fermion masses raised at the start of the previous section. The Higgs mechanism comes to our aid in this too however. Under $\mathrm{SU}(2)_L$ the right-handed fermions form a set of singlets, $u_R^i = (u_R, c_R, t_R)$ for the up-type quarks and similarly for the down-type quarks and leptons. Note that the SM does not include right-handed neutrinos, though the neutrino masses are known to be non-zero, which infers their existence. The left-handed fermions form sets of doublets of SU$(2)_L$:

$$L^i = \begin{pmatrix} \nu_{eL} \\ e_L \end{pmatrix}, \begin{pmatrix} \nu_{\mu L} \\ \mu_L \end{pmatrix}, \begin{pmatrix} \nu_{\tau L} \\ \tau_L \end{pmatrix}, \qquad Q^i = \begin{pmatrix} u_L \\ d_L \end{pmatrix}, \begin{pmatrix} c_L \\ s_L \end{pmatrix}, \begin{pmatrix} t_L \\ b_L \end{pmatrix}. \tag{2.15}$$

Defining $\tilde{\Phi} = i\sigma_2\Phi^*$ we can write down a Lagrangian which is invariant under the full SM gauge group $SU(3) \times SU(2)_L \times U(1)_Y$ for the quark masses (a similar leptonic counterpart exists),

$$\mathcal{L}_{\text{Yukawa}} = -Y^d_{ij}\bar{Q}^i\Phi d^j_R - Y^u_{ij}\bar{Q}^i\tilde{\Phi}u^j_R + h.c., \tag{2.16}$$

where $Y^{u,d}_{ij}$ are Yukawa couplings, comprising two general complex 3×3 matrices $Y^{u,d}$ and the indices i, j run over the three generations [29]. At this point, we are dealing with eigenstates under the weak interaction but would prefer instead to have the more physical mass eigenstates to work with. To do so, we first once again turn to EWSB and then look to diagonalise the Yukawa matrices, to leave straightforward mass terms with $m_\psi = \frac{v}{\sqrt{2}}y_\psi$ for a Yukawa coupling y_ψ:

$$\mathcal{L}_{\text{Mass}} = m^d_j(\bar{d}^j_L d^j_R + \bar{d}^j_R d^j_L) - m^u_j(\bar{u}^j_L u^j_R + \bar{u}^j_R u^j_L). \tag{2.17}$$

This diagonalisation has quite considerable consequences, in that whilst the required rotations do not affect the couplings of the fermions to Z_μ and A_μ, the $W^\pm_\mu$ couplings are sensitive to the flavour rotations. As a result, flavour-changing interactions are possible via the weak force, which are also known as flavour-changing charged currents. The fact that the neutral gauge boson interactions are left unchanged means that no flavour-changing neutral currents (FCNC) are admitted to the SM phenomenology at tree level. From the matrix diagonalisation process, one can define a single complex 3×3 unitary matrix V, the elements of which are indicative of the strength of the flavour-changing interaction between quarks of different flavours. This is the Cabibbo-Kobayashi-Maskawa (CKM) matrix [30, 31]. Writing the resulting relevant Lagangrian terms for these interactions down:

$$\mathcal{L}_{\text{CKM}} = \frac{g}{\sqrt{2}}(\bar{u}^i_L W^+_\mu \gamma^\mu V_{ij} d^j_L + \bar{d}^i_L W^-_\mu \gamma^\mu V^\dagger_{ij} u^j_L). \tag{2.18}$$

The nine real degrees of freedom of the CKM matrix can be cut down significantly by absorption into the rotation of the quark fields, leaving four degrees of freedom. There are several ways to write these down, such as the four Wolfenstein parameters [32], or three rotation angles and a single phase, the last of which is the source of charge-parity (CP) violation in the SM [31]. The same dance can be done in the lepton sector to yield mass terms for the charged leptons and a similar matrix that parameterises the flavour-changing interactions, the Pontecorvo–Maki–Nakagawa–Sakata (PMNS) matrix results, but we need not concern ourselves with the details of this as it requires right-handed neutrinos, which are not in the SM.

Bringing everything together from the electroweak and fermion sectors, QCD and the Higgs component, we finally arrive back at the Lagrangian of Eq. (2.2).

2.4 Higgs Phenomenology

The behaviour of the Higgs boson has been fairly fundamental to my work for the past few years and this section will provide a few details on the situation at the LHC, and the underlying relevant physics for the Higgs boson at this collider.

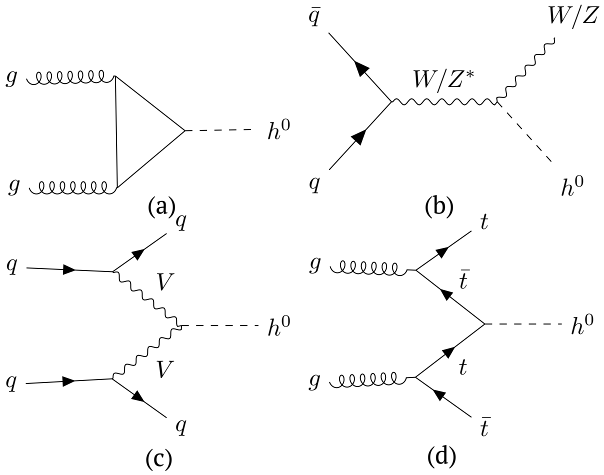

Figure 2.1: Production mechanisms of the SM Higgs boson at the LHC; (a) gluon-gluon fusion, (b) vector boson associated (W, Z Bremsstrahlung), (c) vector boson fusion and (d) top associated prodcution.

There are four main production mechanisms of the Higgs boson at the LHC, each of which is shown in Fig. 2.1. The analytic calculations are set out in the seminal work Ref. [33]. The fusion of gluon bosons is the dominant mechanism at the LHC, accounting for over 80% of the SM

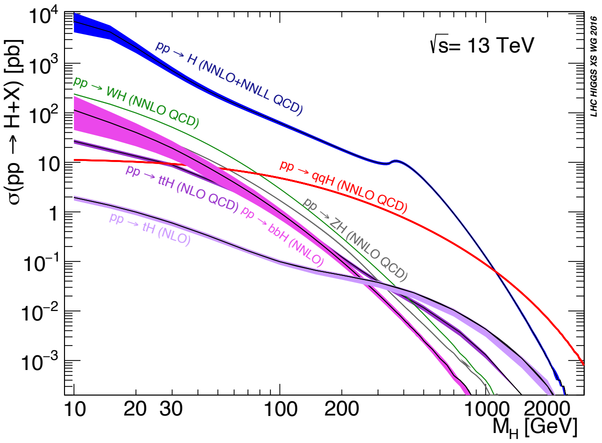

Figure 2.2: Production cross sections of the SM Higgs, reproduced from Ref. [34] .

production cross section for the observed 125 GeV Higgs and proceeds through a loop of heavy quarks, where the amplitude is naturally dominated by the top quark contributions. The other channels of note are, in decreasing order of cross section for the SM Higgs, weak boson fusion, which produces two jets in addition to the Higgs, associated production with a vector boson and finally associated production with a pair of top quarks. The relevant cross sections as a function of the Higgs mass at the LHC are shown in Fig. 2.2, which has been reproduced from the thorough work of the LHC Higgs working group in Ref. [34].

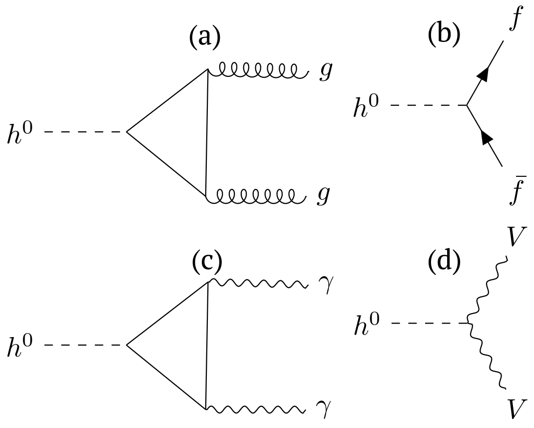

Figure 2.3: Decay channels of the SM Higgs boson at the LHC; (a) to a pair of gluons, (b) to fermions, (c) the diphoton channel and (d) to vector bosons.

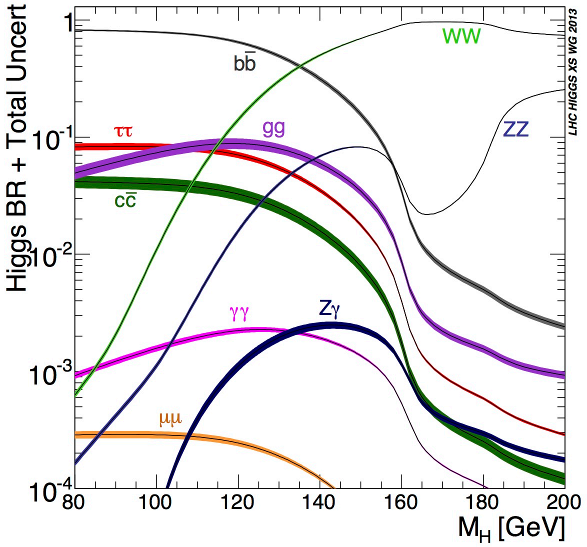

Figure 2.4: Branching ratios of the SM Higgs, reproduced from Ref. [35].

Turning to the decays of the Higgs boson, the most pertinent channels are depicted in Fig. 2.3, with the branching ratios as a function of the Higgs mass displayed in Fig. 2.4. Whilst the couplings of the Higgs to the top quark are large, the decay to a pair of top quarks is not kinematically possible as $m_t = 173$ GeV, and the largest branching ratio is that of a pair of b quarks. However, this is a challenging channel to detect at the LHC, owing to the large QCD background in the hadron collider environment. In contrast, whilst the diphoton decay is distinctly sub-leading in terms of branching ratio, its clear experimental signature makes it much more relevant for Higgs investigations, and indeed in the original discovery of the Higgs boson [27, 28]. Similar phenomenological arguments apply to the decay to a pair of Z bosons.

2.5 Jet Physics

The environment at the LHC is inherently messy from a phenomenological perspective, with a huge number of interactions, decays and further decays leading to a vast number of particles detected, and indeed not detected, in the detectors themselves. In particular, a tenet of QCD is that quarks cannot be observed in isolation as they are coloured particles. The isolated quarks produced in the underlying interaction then undergo hadronisation, forming into mesons and baryons with no net colour. These then decay in turn to further hadrons, leading to a spray of particles in the detector. The particles in these sprays are collectively known as jets, and it is these jets that are typically studied.

There is no single unifying definition of a jet in mathematical terms, with three main algorithms being deployed to combine the final state particles, known as the k_t [36], anti-k_t [37] and Cambridge-Aachen algorithms [38]. Any jet algorithm is required to be infrared and collinear safe, which is to say that the outcomes must be stable if a low energy particle or a particle close to the direction of travel is introduced. Much has been written about jet clustering and the implications for LHC physics, with some excellent examples being Refs. [39–42] but this level of detail is not necessary here.

It is worth being familiar with some of the basic observables of jet and collider physics though, as they crop up in numerous places throughout this work. The coordinate system typically deployed in collider physics uses the pseudorapidity η, which describes how close a particle is to the beam axis, with $\eta = 0$ being perpendicular to the jet axis, and the azimuthal angle ϕ. The nature of the LHC detectors means that the range of observable η is finite, and is typically taken to be $|\eta| < 5$ when working with collider data. In terms of the physical properties of the jet, the primary observable is the transverse momentum, p_T. Further observables are introduced throughout where relevant.

2.6 Challenges to the SM

Thankfully, the grand edifice of the SM is distinctly incomplete. Whilst it is certainly the best model in the game, it is equally certainly not a full description of the fundamental nature of the Universe, and there are some glaring issues that it is unable to address. In this section, some of the more pertinent examples of these issues are briefly introduced and explored by way of motivation for BSM models. There is of course the question of gravity, one of the four fundamental forces of the Universe and the one that dominates the large scale evolution of the cosmos. Gravity is not given a sniff in the SM, which is entirely valid at the tiny scales that the SM proclaims to describe, but is clearly unsuitable for a full understanding of the Universe. The masses of neutrinos are not explicitly accounted for in the SM formalism set out above, but a straightforward extension with right-handed neutrinos can account for the experimental fact that the neutrinos oscillate and thus have mass [43–52], so this need not be a major concern and will not be addressed again here.

2.6.1 Baryogenesis and the Sakharov Criteria

Despite making many people very angry and being widely regarded as a bad move, the Universe does in fact exist. More specifically, the Universe contains more baryonic matter than antimatter, with everything we perceive and indeed are, consisting of the former. There are no antimatter galaxies or constellations in the sky, no little green antimatter aliens. Whilst this may seem rather self-evident, it speaks to a fundamental asymmetry in the very earliest instants of creation, albeit on a very small scale, which must be accounted for in any accurate model. This is where the Sakharov criteria come in [53]. Developed by the winner of the 1975 Nobel Peace Prize Andrei Sakharov, these criteria set out the necessary conditions that must be met during the early baryogenesis period of the Universe to generate the observed asymmetry. BSM models can then be evaluated within this context, to examine if they can succeed in meeting the criteria. For a review see, for example, Ref. [54].

The first of these criteria is enjoyably straightforward; baryon number conservation must be violated. Clearly, any model that seeks to create more baryons than anti-baryons must not keep the net number of baryons the same. Secondly, both charge and CP symmetries must be violated. This again allows for processes that produce baryons to produce an unequal number of anti-baryons of opposing charge, and then for differing quantities of baryons of one handedness and anti-baryons of the opposing handedness to be produced. Finally, reactions must occur outside of thermal equilibrium, so that the baryon producing processes are not cancelled out by their reverse processes. This is typically codified as the requirement for a model to have a strong first order phase transition, but may be achieved through other processes such as leptogenesis.

How then does the SM stack up against these three criteria? Much as in other areas, pretty well, but still decidedly leaving something to be desired. Baryon number violation is possible through non-perturbative sphaleron mediated interactions [55]. The electroweak interactions provide avenues for both charge and CP violation as mentioned above, and the latter can be quantified using the CKM matrix elements [56]. However, the level of CP violation seen experimentally in SM interactions is insufficient for baryogenesis, and so additional sources of CP violation must be sought in BSM models. As for the final condition, if the electroweak phase transition (EWPT) of the SM proves to be strongly of the first order (a SFOEWPT) then all is well. Alas, this is only possible if the SM Higgs mass is below around 70 GeV [57], which it is not, and so NP must again be deployed to meet this condition. Models with modifications to the Higgs sector are particularly interesting in this regard - see Chapter 4 for a comprehensive study of one such model.

2.6.2 The Darkness

The asymmetry in antimatter compared to matter is not the only oddity in the heavens. Dark matter (DM) stands somewhat in contrast to the baryon asymmetry though, in that there is an unexplained abundance of dark matter, to the extent that it accounts for around five times as much of the energy density of the Universe as baryonic matter [58]. DM has only been confirmed to interact gravitationally, making such particles challenging to observe at traditional detectors like the LHC. Evidence for the existence of DM has been building for some 50 years and the fact of its existence is no longer a topic of debate [59–69]. However, the precise nature of exactly what DM is, on a fundamental, particle level remains an area of very active research, with reviews of the plethora of candidates in Refs. [70, 71]. One thing that all these candidates have in common (apart from memorable acronyms like WIMP, MACHO and SIMP), is that they require BSM physics, either as new particles or for example, modified gravity or primordial black holes.

Even more unknown is dark energy. This rather mysterious form of energy is widely accepted to dominate the total energy density of the Universe, with its effects seen through astronomical observations such as the unexpected acceleration of the expansion of the Universe [72, 73]. There is little in the way of concrete consensus on the fundamental nature of dark energy and though it is evidently beyond the SM, it is also beyond the scope of this work.

2.6.3 Anomalous Magnetic Moment of the Muon

One particular observable that deserves highlighting in this section is the anomaly of the anomalous magnetic moment of the muon, which has been a source of much attention in recent years. The potential energy of a particle in a magnetic field $\overrightarrow{B}$ is given by $E = -\overrightarrow{\mu} \cdot \overrightarrow{B}$ for a magnetic moment $\overrightarrow{\mu}$:

$$\overrightarrow{\mu} = \frac{e}{2m} g \overrightarrow{S}, \tag{2.19}$$

where $\overrightarrow{S}$ is the spin angular momentum. The Dirac equation [74] gives the magnetic moment of the leptons as $g = 2$, but there are higher orders of quantum loop level effects that give slight deviations from this value. This is the anomalous magnetic moment, which is defined by

$$a_\mu = \frac{g-2}{2}. \tag{2.20}$$

This can be measured very precisely for electrons and muons, and the former agrees incredibly well with predictions. The latter however has shown significant disagreements with the SM predictions in recent measurements at Fermilab [75] and a previous Brookhaven National Laboratory measurement [76]. A question mark does remain however in just how significant this disagreement is, with the headline figure of 4.2σ coming from the SM prediction in the White Paper of Ref. [77] from data driven approaches, in turn based on Refs. [78–97] and the combined experimental value. On the other hand, a lattice QCD evaluation from the BMW Collaboration [98] improves the precision of the lattice calculations used in the White Paper [99–107] to put the disagreement at 1.6σ. In either case, it is worth putting a_μ under the microscope as a possible sign of NP. This is done in some detail in Sec. 4.7.

2.7 Effective Field Theories

Whilst there are clear signs that BSM physics must exist, no one model has particularly strong evidence supporting it. There is of course always the possibility that there are indeed more things in heaven and Earth than are (currently) dreamt of in our philosophy, and as such model independent frameworks should be explored. The current dearth of evidence for new states can be taken as an indication of a separation between the energy scales that can be probed directly at the LHC and that of the NP particles. The effects of the NP can still be captured and, crucially, expressed in a model independent mathematical fashion known as effective field theories (EFTs).

Denoting the energy scale of the BSM physics as Λ, the NP effects can be integrated out and left as a consistent extension of the SM through operators $\mathcal{O}$ with more than four mass dimensions [108], where four dimensional operators correspond to the SM. Truncating the expansion at some order of Λ^{-1}, viable deformations on these operators, constructed from SM fields, can be found from the LHC data. An instructive example, and one that is pertinent in Chapter 5, is that of the SM effective field theory, SMEFT. Whilst the model is defined up to infinite dimensions, for amplitude calculations the expansion is often terminated at order Λ^{-2} as contributions to the amplitude are suppressed beyond this by the higher orders of Λ in the denominator.

The Lagrangian is thus [109–114]

$$\mathcal{L}_{\mathrm{SMEFT}} = \mathcal{L}_{\mathrm{SM}} + \sum_i \frac{C_i}{\Lambda^2}\mathcal{O}_i, \tag{2.21}$$

where C_i is the Wilson coefficient (WC) of the operator $\mathcal{O}_i$. There is only a single valid dimension five operator, the Weinberg operator [115], but this only concerns neutrino masses and thus is of no relevance to this work and will not be discussed further, so only the dimension six operators need be considered. In the most generic formulation, there are some 2499 such operators, which may well make this approach seem hopeless. Thankfully, a few assumptions can be made to vastly reduce the size of the basis of operators that need be considered to a much more manageable 59 in the Warsaw basis [113]. This has been studied intensely in the literature across a wide range of sectors [116], and will form the basis of Chapter 5. By constraining the WC of an operator, one can place model agnostic limits on the effects of NP, and this is the typical goal of investigations in the EFT formalism, but they can also be used as a tool to study specific models, with the weak effective field theory deployed in this fashion in Chapter 4.

Chapter 3

Interference Effects in Cascade Decays of Top-philic Extended Higgs Sectors

As set out in the previous chapter, there are no clear and obvious discrepancies between SM predictions and the experimental measurements at the LHC. One interpretation of this lack of a smoking gun signal is that there must be a large gap between the energies which the LHC can probe, the TeV scale, and the energy scale of BSM physics. This is the primary motivation behind the EFT formulation (see Sec. 2.7), which provides a framework for systematic classification of deviations from the SM. Looking at the situation another way, if the BSM physics sits around the energy scales available to the LHC, then the fact that there are no concrete signals of the BSM particles can be taken as a sign that the agreement should be interpreted as an avenue to set constraints on the parameters of the BSM models.

Models that extend the Higgs sector of the SM to include new scalar particles offer a particularly opportune avenue for exploration in this regard, as they provide solutions to some of the shortcomings of the SM, from new dark matter candidates to opening up viable parameter spaces for a SFOEWPT. Assuming that these new exotic states are capable of being produced through gluon fusion, then their subsequent decay to a pair of top quarks is a search channel worthy of consideration.

The literature on such extensions and searches in this channel [117–129] show that there can be large interference effects between the BSM process and the irreducible SM background, which can have grave implications of the discovery potential of such channels, particularly for Higgs sector extensions that lie in the parameter space that remains compatible with the current non detection of such states [130]. From an experimental perspective, searches for resonance structures will overestimate the sensitivity to BSM signals unless they account for these interference effects in a model dependent fashion. On the theoretical side, the effects render the use of Breit-Wigner propagators unsuitable as an approximation due to the distortion of the distribution. The alterations to the Breit-Wigner distribution of a model dependent BSM state have been studied before in the literature [131–136], but in this chapter the focus is on recovering the sensitivity to the new states in those cases where the interference effects are particularly problematic. One process well suited for study in this respect is an asymmetric cascade decay [137, 138], as such processes are less impacted by destructive interference, opening up a robust avenue for BSM searches in models that allow for such decays [139, 140].

In this particular chapter, the two singlet extended SM is used, introducing two new Higgs bosons, $H_{2,3}$, with $m_{H_3} > m_{H_2} > m_h$ for a SM-like h; a detailed discussion can be found in Ref. [137]. This allows for a detailed analysis of the signal-signal and background-signal interference, as the decay $H_3 \to H_2 h$ can be large, whilst the decays of the new Higgses to a pair of top quarks are subject to large interference effects, rendering the cascade decay $H_3 \to H_2 h, H_2 \to t\bar{t}, h \to b\bar{b}$ a channel of note, though not without its challenges [138]. Looking ahead to the High Luminosity LHC (HL-LHC), the effects are extrapolated to the expected performance of an integrated luminosity of 3/ab, in such a parameter space that the cascade decays can be observed with statistical significance.

3.1 The Two Singlet Extended SM

As briefly outlined above, the extension of the SM by two singlets is a physically motivated model for this investigation, the details of which are set out in this section. In addition to the Higgs doublet of the SM, H, two real singlet scalar fields, S_1 and S_2 are introduced, which give rise to CP-even BSM structures only [141]. Such a model has been well studied in the literature, owing to its ability to ameliorate the issues of dark matter and the SFOEWPT (see Sec. 2.6) [142–149].

Two new discrete $\mathbb{Z}_2$ symmetries are imposed;

$$\mathbb{Z}_2^{(S_1)} : \; S_1 \to -S_1, \; S_2 \to S_2, \tag{3.1}$$

$$\mathbb{Z}_2^{(S_2)} : \; S_1 \to S_1, \; S_2 \to -S_2, \tag{3.2}$$

with the potential, having only real coefficients, given by

$$\begin{aligned} V(H, S_1, S_2) = -\mu_H^2 H^\dagger H - \frac{1}{2}\mu_{S_1}^2 S_1^2 - \frac{1}{2}\mu_{S_2}^2 S_2^2 + \lambda_H (H^\dagger H)^2 + \lambda_{S_1} S_1^4 + \lambda_{S_2} S_2^4 \\ + \lambda_{HS_1} H^\dagger H S_1^2 + \lambda_{HS_2} H^\dagger H S_2^2 + \lambda_{S_1 S_2} S_1^2 S_2^2. \end{aligned} \tag{3.3}$$

Following the conventional pattern of EWSB (see Sec. 2.2), each of the scalars has a non-zero VEV, and the weak bosons become massive as in the SM. The breaking of the $\mathbb{Z}_2$ symmetries leaves a total of three scalar bosons, ϕ_{H,S_1,S_2}, which can be transformed to the mass eigenstates; massive CP-even neutral scalars $H_{1,2,3}$, where convention dictates $m_{H_3} \geq m_{H_2} \geq m_{H_1}$, via a 3×3 orthogonal mixing matrix R such that

$$\begin{pmatrix} H_1 \\ H_2 \\ H_3 \end{pmatrix} = R \begin{pmatrix} \phi_H \\ \phi_{S_1} \\ \phi_{S_2} \end{pmatrix}. \tag{3.4}$$

This matrix can in turn be parameterised with three mixing angles $\theta_{1,2,3} \in [-\pi/2, \pi/2]$, using $s_{\theta_i} = \sin(\theta_i), c_{\theta_i} = \cos(\theta_i)$:

$$R = \begin{pmatrix} c_{\theta_1} c_{\theta_2} & s_{\theta_1} c_{\theta_2} & s_{\theta_2} \\ -s_{\theta_1} c_{\theta_3} - c_{\theta_1} s_{\theta_2} s_{\theta_3} & c_{\theta_1} c_{\theta_3} - s_{\theta_1} s_{\theta_2} s_{\theta_3} & c_{\theta_2} s_{\theta_3} \\ s_{\theta_1} s_{\theta_3} - c_{\theta_1} s_{\theta_2} c_{\theta_3} & -s_{\theta_1} s_{\theta_2} c_{\theta_3} - c_{\theta_1} s_{\theta_3} & c_{\theta_2} c_{\theta_3} \end{pmatrix}. \tag{3.5}$$

The lightest of these bosons is taken to be the observed 125 GeV Higgs boson, which is thus denoted as h herein. Finally, the requiring of a minimum of the potential [150] leaves only seven parameters of the model. These are the masses of the two new scalar bosons, the VEVs of their corresponding singlets and the three mixing angles.

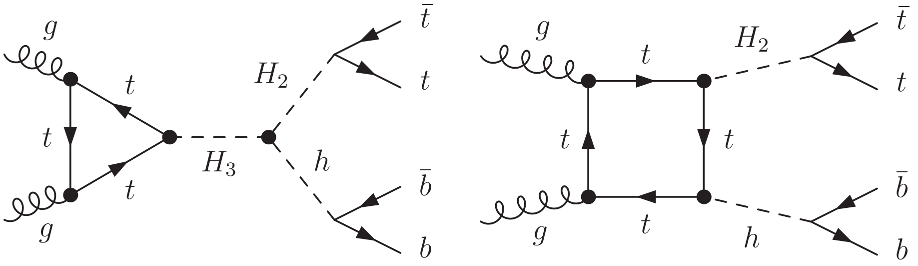

(a) (b)

Figure 3.1: Representative Feynman diagrams contributing to the resonant (a) and non-resonant (b) BSM signal. H_3 on-shell signal-signal interference arises from interference between diagrams (a) and (b). Not depicted are background topologies that contribute to $t\bar{t}b\bar{b}$ production in the SM.

Of particular note are the trilinear couplings between the three Higgs bosons, which are denoted by λ_{ijk} $(i, j, k \in \{h, H_2, H_3\})$, as these couplings allow for interactions between these bosons, with the cascade decay naturally being crucially dependent on this coupling, given by

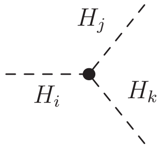

$$= -i\lambda_{ijk} = iS_{ijk}\frac{\partial^3\mathcal{L}}{\partial H_i \partial H_j \partial H_k}, \tag{3.6}$$

with the Lagrangian given as Eq. (1) in [1] and S_{ijk} being a combinatorics factor to ensure consistency of conventions. The Feynman diagrams for the cascade decay and an interfering process can be seen in Fig. 3.1.

Scanning over the seven parameters of the model allows for the exploration of the cascade decay of interest here, but some constraints must be placed on these parameters for the scan to yield meaningful results. Clearly, the cascade channel must be kinematically accessible; $m_{H_3} \geq m_{H_2} + m_h$, $m_{H_2} \geq 2m_t$. To be specific, the parameters are varied randomly with a uniform prior such that $m_{H_2} \in [m_t, m_t + 200 \text{ GeV}]$, $m_{H_3} \in [m_h + m_{H_2}, m_h + m_{H_2} + 500 \text{ GeV}]$ to allow sufficient kinematic space for the cascade decay. Additionally, the phenomenology of the 125 GeV scalar must replicate that of the SM Higgs within the current experimental bounds, which is enforced by coupling modifiers $\kappa \geq 0.9$. The requirements of perturbativity and positivity are met by following the constraints detailed in Refs. [137, 151, 152], with all $|\lambda_i| < \pi$ from the former.

The generated points are checked against the electroweak oblique corrections [153, 154], with the vast majority of points falling into the permitted range from Ref. [155] once the selection criteria have been satisfied. By looking to maximise $\sigma_{H_3} \times \mathcal{B}(H_3 \to H_2 h)$, with a lower limit of 4 fb, parameter regions in which the cascade decay is of particular note can be identified, allowing for more thorough examination of the interference effects. The results of the Higgs Cross Section Working Group [34, 35, 156] are used to account for higher order effects by extrapolation of the SM Higgs width, which is valid as the new scalars mix with the lighter scalar of the model. The non-resonant three body decays of $H_{2,3}$ are computed, but found to be negligible; a situation identifiable with the new scalars decaying like the SM Higgs or through the cascade. This scan shows that the maximal cross section regions have $m_{H_3} \approx m_{H_2} + m_h$, yielding a large branching fraction for the decay $H_3 \to H_2 h$.

3.2 Interference Effects

The interference effects can now be examined using the valid points from the above scan. The effects in the $pp \to H_{2,3} \to t\bar{t}$ and $pp \to H_{2,3} \to hh$ channels are also discussed, as these process can proceed through diagrams such as those shown in Fig. 3.1. In this fashion, the impacts of interference in both the s-channel and box topologies can be studied, with the former being of note due to the trilinear Higgs couplings depicted in Fig. 3.6. To pin down the extent to which interference affects each channel the mass of the heavy scalar is reconstructed from the decay states and the cross section for each channel evaluated within the range $m_{H_i}^{\text{reco}} \in [m_{H_i} - 0.15 m_{H_i}, m_{H_i} + 0.15 m_{H_i}]$ for the reconstructed mass $m_{H_i}^{\text{reco}}$, with $i = 2, 3$. The analytical and numerical calculations are performed using a combination of VBFNLO [157, 158], FEYNARTS, FORMCALC [159], and LOOPTOOLS [160–163]. The UV divergences are found to be finite and the calculations were independently cross checked.

To examine the impact of interference effects, the ratio of combined signal, σ_S, and interference, σ_I, cross section to the signal cross section is shown in the following plots for various sources of intereference. Signal-background interference in the top pair final states is a relevant effect, as can be seen in Fig. 3.2, which is also illustrated in Ref. [130]. The $H_3 \to t\bar{t}$ channel has a low signal, due to the asymmetric cascade decay being large as a conscious result of the parameter choices. This small signal rate puts this channel particularly at risk from interference effects, although as the cross sections are already small, the truly notable element, that of the discovery potential, is left relatively unchanged. On the other hand, as the second row of Fig. 3.2 illustrates,

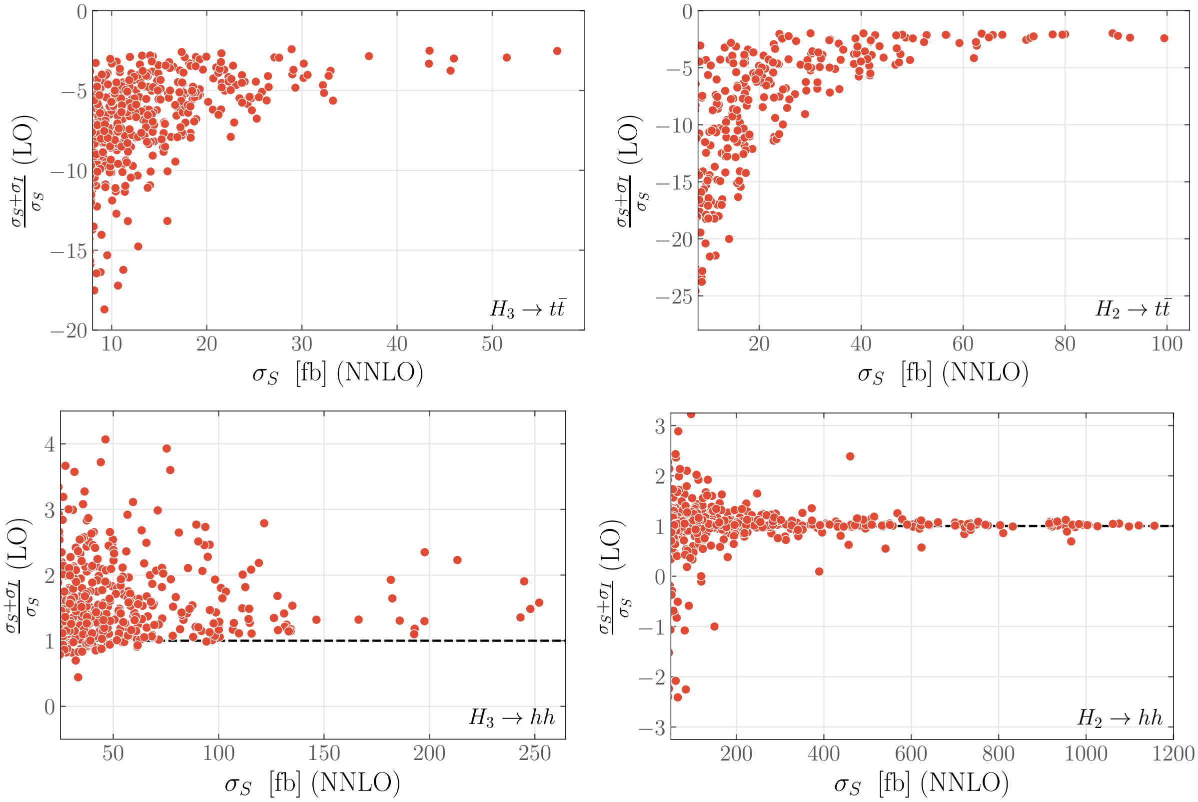

Figure 3.2: Scatter plots highlighting the importance of signal-signal interference for the resonance search $H_i \to t\bar{t}, hh$ in the parameter region selected by the scan criteria detailed in the text.

the di-Higgs decays suffer less from this signal-signal interference, particularly for large cross sections, thereby motivating the symmetric decay modes as viable search candidates, which is given further consideration in Ref. [137].

For the asymmetric cascade decays, beginning with the signal-background interference case depicted in Fig. 3.3, a similar picture emerges, in that the width is small (due to additional branching ratio and combinatric factors for the signal channel) compared to the resonance mass and so interference is not a limiting factor. Signal-signal interference can be more significant, owing to the richer multi-Higgs tapestry of this channel; see Fig. 3.4. These effects must be accounted for should a BSM discovery be made, though the effects do not egregiously impact the discovery potential when the cross sections are large and thus a discovery is more likely.

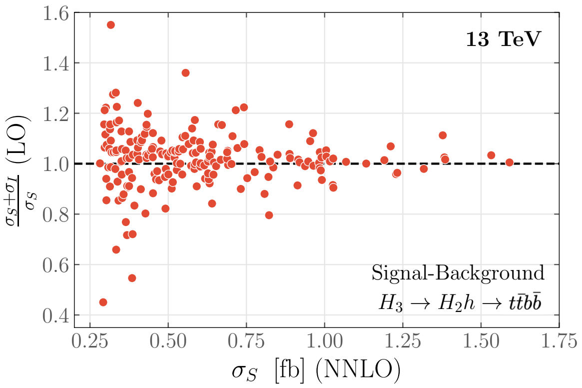

Figure 3.3: Cross section of the signal only case and impact of signal-background interference in the cascade decay $H_3 \to H_2 h \to t\bar{t}b\bar{b}$ at 13 TeV.

The unfortunate fact remains that the nature of these decays, of scalars to quarks, makes them hard to detect at the LHC, see Ref. [138], even when the interference effects are relatively small. Looking to the future, the Future Circular Collider (FCC-hh), which will operate at a centre of mass energy of 100 TeV, will give a dramatically increased cross section to examine. As shown in Fig. 3.5 the qualitative features translate well to the FCC-hh, so the latter may have the potential to provide additional information on potential discoveries in asymmetric cascade decays without significant impact from signal-background interference.

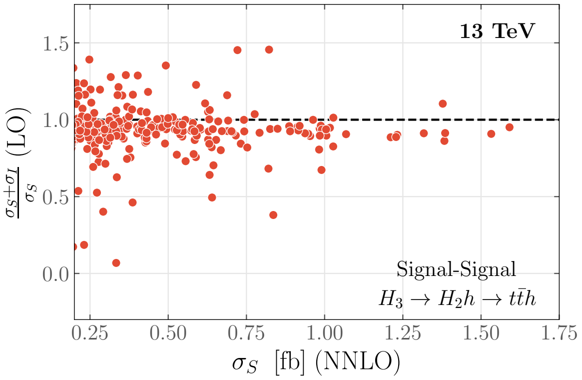

Figure 3.4: Importance of signal-signal interference for $H_3 \to H_2 h$ resonance searches. Included in this comparison are interference contributions with propagating $H_{i\neq 3}$, Fig. 3.1(a), as well as non-resonant $gg \to H_2 h$ amplitude contributions that arise from the box topologies of Fig. 3.1(b).

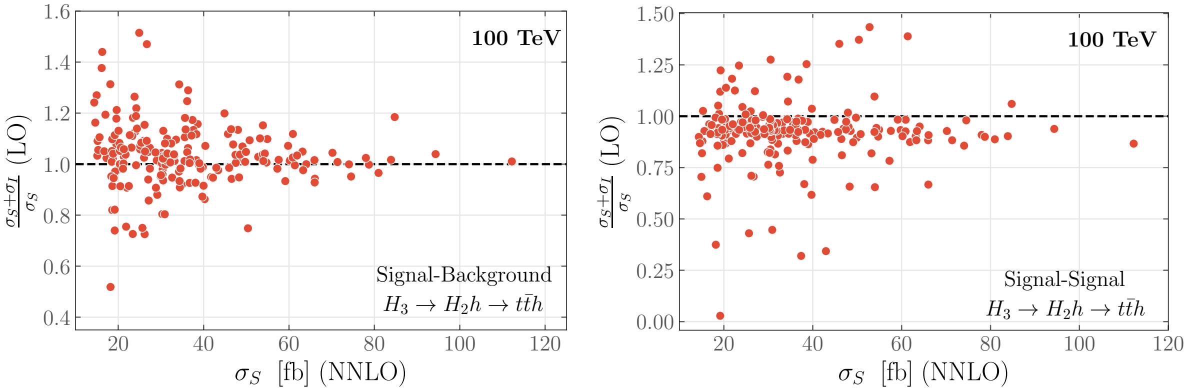

Figure 3.5: Similar to Figs. 3.3 and 3.4, but for an FCC-hh centre-of-mass energy 100 TeV.

3.3 Impact on Significance

Narrowing down the focus, now the possible sensitivity limitations from interference effects will be examined for 13 TeV collisions at the HL-LHC, scanning over m_{H_3} and m_{H_2} and deploying machine learning techniques to do so. Neural networks play a major role in cutting edge collider physics and can significantly boost the sensitivity of experiments, with efficacy in the cascade decays like those examined in this chapter [138].

In order to concentrate on parameter regions where the sensitivity to cascade decays is large and thus of interest, the branching ratios are fixed as $\mathcal{B}(H_3 \to H_2 h) \sim 0.5$ and $\mathcal{B}(H_2 \to t\bar{t}) \sim 1$, by choice of the trilinear coupling and widths. Fully-showered and decayed events are considered using PYTHIA8 [164], with the showered events saved in the HEPMC format [165] and the decay proceeding as $H_2 \to t\bar{t} \to \ell^+\ell^- b\bar{b} + \not{E}_T$ and $h \to bb$. Jets are reconstructed in MADANALYSIS [166–169] using the anti-kT algorithm [37] with a radius of 0.4, as implemented in FASTJET [170, 171]. Selected jets must satisfy $p_T(j) > 20$ GeV and $|\eta(j)| < 4.5$ with b-jet candidates required to present within the central element of the detector to be tagged, i.e. $|\eta(b)| < 2.5$, with the associated b-tagging efficiency taken to be 0.8 (see e.g. Ref. [172]). Whilst this opens the door for mistagged light quark jets in the background, this avenue need not be explored as this issue remains in experimental collider analyses. For an event to be considered in this analysis, four b-jets must be tagged, in addition to two leptons with $p_T(\ell) > 5$ GeV and $|\eta(\ell)| < 2.5$ that can be considered isolated. The isolation criteria are such that a lepton is considered isolated if the sum of transverse momenta of jets within $R = \sqrt{(\Delta\eta)^2 + (\Delta\phi)^2} = 0.3$ of the lepton is less than 20% of the lepton's p_T. The missing transverse momentum is identified as opposite to the sum of four-momenta of jets and leptons. No detector effects are included. A total of 30000 events for both background and signal cases, without interference, are generated subject to these criteria.

The dominant backgrounds are from $pp \to t\bar{t}b\bar{b}$, while $pp \to t\bar{t}(Z/h \to b\bar{b})$ is also significant, while processes with pairs of gauge bosons ($pp \to bb\bar{b}\bar{b}W^+W^-$ and $pp \to bb\bar{b}\bar{b}ZZ$) have reduced rates compared to the rest of the processes. The cross sections of $t\bar{t}b\bar{b}$, $t\bar{t}h$ and $t\bar{t}Z$ are rescaled with K-factors of 1.8 [173], 1.17 [34] and 1.2 [174] respectively to account for QCD corrections.

The goal of the neural network implementation is to classify events as either signal or background and thereby allow selection of the final signal region. The network is built using KERAS [175] and comprises a Long Short-Term Memory (LSTM) layer of 45 units, with tanh activation and a dropout of 0.1 to avoid overfitting. A sigmoid function is used as the recurrent activation of the LSTM, while the Adam algorithm [176] is used to minimise the categorical cross-entropy and optimise the network, with a learning rate of 0.001 and an output layer activated with the softmax [177] function.

The event data is split into training, validation and testing sets, consisting of 81%, 9% and 10% respectively, of the full dataset. Events are fed into the network in batches of 200 apiece, using the four-momenta (in terms of E, p_T, η, ϕ) of the b-jets and leptons of the event, along with the missing transverse momentum. At every point in the parameter space, a network is trained for 100 epochs, unless it meets the early stopping condition of the loss not decreasing for ten consecutive epochs. Meanwhile, the learning rate decays by a factor 0.1 with a patience of three epochs.

To minimise background systematics the neural network score threshold is selected at each point in the mass parameter space so σ_S/σ_B remains large, where σ_S is the signal cross section without interference effects and σ_B is the background cross section. It is the cut on this network score that defines the search region, with the models used to evaluate the quantity of events with either positive or negative weighting that pass from an interference only sample of events. The significance is then defined as the ratio $S/\sqrt{B}$, for S signal and B background events in the given search region.

This significance, along with the attendant change due to interference effects, is shown in Fig. 3.6, which illustrates how the impact of the interference effects on the discovery potential of this channel at the HL-LHC is small and should not be considered a limiting factor, with effects of

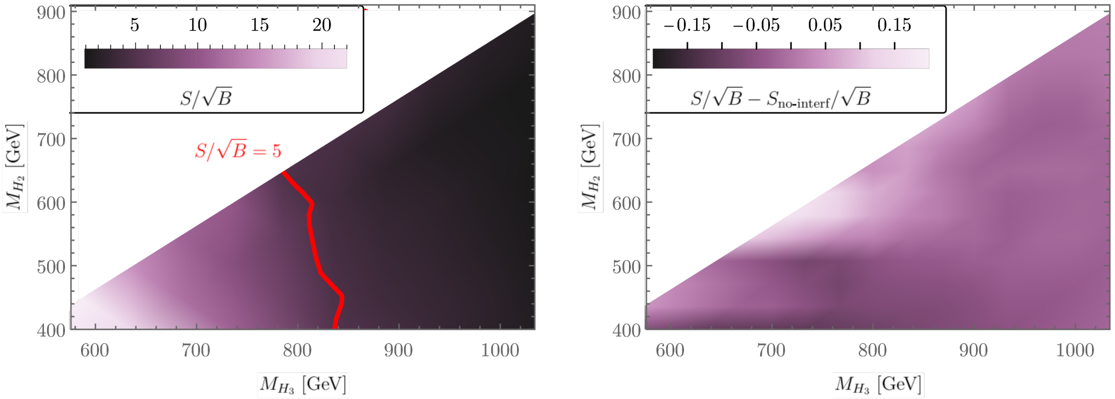

Figure 3.6: On the left, the significance $S/\sqrt{B}$ is displayed for an integrated luminosity of 3/ab. The scan over the masses was performed by assuming no CP-odd contributions and fixing the widths and trilinear couplings such that $\mathcal{B}(H_3 \to H_2 h) \sim 0.5$. The cross sections were normalised to the rates of Ref. [138]. The difference in significance arising from the inclusion of interference is shown on the right, where $S_{\text{no-interf}}$ is the number of events for the signal process without the effects of interference. Theoretical or experimental systematics in this comparison are not included in this comparison.

.

less than 5% when $\mathcal{B}(H_3 \to H_2 h)$ is large. This stands in contrast to the results in the $t\bar{t}$ channel, as discussed in Sec. 3.2. It's worth pointing out at this juncture that the network used here is not trained using any particular characteristics of the interference effects, meaning that these results should generalise, at least qualitatively, if not in terms of overall significance, to other analyses. This is a product of the interference effects being subdominant.

3.4 Conclusions

This chapter has provided a first look at some of the methods used to investigate BSM physics, both through the introduction of a simple and natural SM extension in the two singlet model, and in a machine learning implementation to further probe the behaviour of this model in collider environments, themes which recur throughout this work. In general, interference effects can play a major, if vexing role, in the sensitivity of BSM searches, as they can seriously limit the sensitivity that can be achieved at collider experiments. This can be a particular challenge when the otherwise most prominent decay channels suffer adverse effects, such as in the case of $t\bar{t}$ resonances in top-philic extensions of the scalar sector.

In the case of asymmetric cascade decays in the two singlet extension of the SM, the interference effects have been shown here to be largely absent. Following this result through to fully showered and hadronised final states the significance of detecting this final state in regions of sizeable branching ratio is not limited by signal-background interference. Sensitivity can be further enhanced using machine learning techniques, boosting the possibility of a BSM discovery in this channel at the LHC and beyond. If such a discovery is made, then the $H_3 \to H_2 h$ channel can become sensitive to signal-signal interference, thereby opening up a rich new vein to explore the BSM physics on display. In such a scenario, the machine learning techniques used in this chapter will also come in use, as the interference sample is not used when performing the categorisation. Thus, the asymmetric cascade decays of multi-Higgs models offer a rich phenomenology which may yet bear fruit in experimental searches and as such should be closely monitored for signs of new physics at the LHC and future colliders.

Chapter 4

Comprehensive Studies of the Two Higgs Doublet Model

The decade and counting of searches since the discovery of the SM Higgs have not yet yielded any concrete signs of NP or any unexpected particles, in stark contrast to the ballooning and, at the time discombobulating, particle zoo of the 1960s, which awoke such a passionate fervour aimed at overhauling the accepted models. This flies somewhat in the face of the numerous signs that NP must exist, from the collection of hints across a slew of anomalies in measurements to the larger signs such as dark matter and the need to satisfy all of the Sakharov criteria, as set out in Sec. 2.6.1.

The Two Higgs Doublet Model (2HDM) is a relatively straightforward and appealing BSM model that has been well studied in the literature. Some of the appeal of this model is due to the possibility it may be able to resolve some of these issues with the SM, including some of a conceptual nature, see e.g. Ref. [178]. From a theoretical perspective, 2HDMs could provide the missing amount of CP violation to explain the baryon asymmetry in the Universe and generate a first order phase transition in the early Universe, as required by the Sakharov criteria [53]. In addition, they have favourable phenomenological properties regarding the UV completion of the SM [3, 5, 130, 179–188]. By dint of similar implementation of the SM EWSB mechanism (see Sec. 2.2), they avoid the issues of fine-tuning with electroweak precision measurements that can arise in higher dimensional representations of electroweak $SU(2)_L \times U(1)_Y$ breaking [189]. Further, 2HDMs often appear in more complex BSM models, especially supersymmetric theories.

On a perhaps more prosaic level, the studies of the SM Higgs have shown it to behave much like, well, the expected SM Higgs. However, this is not an ironclad identification, with current experimental constraints only placing bounds of $\sim 10\%$ [190, 191] on the possible deviations of the Higgs bosons' couplings. This leaves sufficient scope for some NP in the Higgs sector. The modifications of these couplings, or indeed the presence of the new particles invoked by the 2HDM may also be able to alleviate the anomalies in experimental measurements. Sticking with the experimental side of things, there are a number of avenues by which the 2HDM may be constrained or, even more tantalisingly, observed.

This all provides ample motivation to explore, in depth, the 2HDM. This is the focus of this chapter, which pulls together a great deal of work that has occupied a significant proportion of my efforts over the course of my studies, crystallising in the trio of papers Refs. [3, 5, 7], each of which builds upon the last. Whilst these works examine different types of the 2HDM in turn, each categorised by their Yukawa couplings, this work moves sector by sector and examines all four types of 2HDM in each sector, in order to provide a detailed look at the 2HDM from all angles. By examining the model using both EFT and resonant search approaches, all bases are covered. This chapter therefore provides a good example of an in-depth study of a specific BSM model in the face of all current experimental data and theoretical considerations; a key element of modern particle physics phenomenology. The 2HDM also appears tangentially in the more recent work Ref. [9].

Whilst there are, as of yet, no direct signatures of new particles, the vast wealth of experimental measurements collected can be put to good use in constraining the parameter space available to models of NP, through the contributions of the proposed new Higgs bosons to the calculations. Here over 270 observables are leveraged to narrow down the possible parameter values for the 2HDM, using the most recent measurements at all possible stages. This comprises the most comprehensive study of the 2HDM that I am aware of, extending such works as Refs. [192, 193]. Additionally the many direct searches for BSM signals at colliders are collected in order to further constrain the parameter space, and going further these bounds are extrapolated with a view to the future of experimental particle physics at the HL-LHC. The complementary nature of these direct searches with the indirect constraints from the measured observables is also highlighted as this demonstrates the power of bringing all possible data sources together. Moreover, this leaves us with a clear view of the regions of parameter space that deserve specific scrutiny at future experiments. There are even more avenues from which one can scrutinise the model, such as delivering the required SFOEWPT and explaining the particularly notable anomaly of the anomalous magnetic moment of the muon, and these are also given due consideration.

One of the most influential papers in the 2HDM literature is Ref. [192] from 2009, which examined the 2HDM of Type II, finding that this 2HDM does not outperform the SM and setting a lower bound on the new charged Higgs boson mass of 316 GeV. More recently, in 2017, Ref. [193] used HEPfit to bring a significant number of observables from different sectors, including electroweak precision observables, Higgs data, a handful of flavour observables and theoretical considerations to bear on the 2HDM. This resulted in a lower mass bound on the charged Higgs boson of 740 GeV, with only small deviations from the alignment limit permitted, the latter driven largely by theoretical considerations. Extending this analysis confirms the finding of Ref. [193] in that the wrong sign limit, which is discussed in detail in Sec. 4.3, is disfavoured for the Type II 2HDM.

One of the central pillars of this analysis of the 2HDM is the Python program package flavio [194], which provides a framework to examine flavour observables in the face of current data, and so has been widely used for such observables in this chapter. In order to include the effects of NP in flavio, the Wilson coefficients of the relevant dimension-6 operators of the appropriate EFT are taken as inputs (see Sec. 2.7). Specifically, the Weak Effective Theory, WET, is used for energy scales below the electroweak scale, with the SMEFT used above this scale. For a full list of operators in the flavio basis for each effective theory, see the documentation of the WCxf package [195]. When considering the flavour observables, the relevant NP contributions to the WET operators make use of five active flavours, except in the case of the anomalous magnetic moment of the muon, for which three active flavours are used.

After calculating the NP contributions to the appropriate WCs flavio can be used to perform a scan over the relevant parameter space to determine which regions are allowed and which are excluded by the observables in question. The package flavio expresses experimental measurements and input parameters as various one- and two-dimensional probability distribution functions, while theoretical uncertainties are included by performing the calculation of each predicted value a number of times, here taken to be 10^4, for values of the input parameters that have been randomly selected within their probability distributions. The standard deviation of the predicted values is then taken as the theoretical uncertainty. Throughout, the "fast likelihood" method provided by flavio is used for creating likelihood functions as $\mathcal{L} = e^{-\chi^2(\xi)/2}$, where ξ, the set of fit parameters that contribute, are taken to be their central values, with the combined theoretical and experimental covariance matrix used in the fit. Further details for the interested reader can be found in the relevant FLAVIO documentation [194], with a useful companion website also available[1].

On its own however, FLAVIO does not provide the holistic treatment of the 2HDM that this chapter strives toward, though it does provide a solid theoretical and computational framework that can be exploited to the desired ends. For instance, the Higgs signal strengths are best studied alone, using the full analytical expressions, but it is possible to use the FLAVIO framework to subsequently construct likelihoods and consistently combine experimental measurements. This then allows for the inclusion of the Higgs signal strengths into a global fit. Similarly, the purely theoretical considerations and electroweak precision observables cannot be expressed in terms of the dimension-6 operators required for proper use of FLAVIO. Instead, the results given here are taken from Monte Carlo scans of the full parameters, with the likelihood functions and experimental correlations for the electroweak precision observables then integrated into the global fit through some modifications to the FLAVIO package.

The chapter is organised as follows. The theoretical basis of the 2HDM is given in Sec. 4.1, with the theoretical constraints of perturbativity, vacuum stability and unitarity, which together act to enforce mass degeneracy in each of the new Higgs bosons, independently of the type of 2HDM, studied in Sec. 4.2. In Sec. 4.3, the signal strengths of the SM Higgs become the focus, and what these can tell us about the parameter space remaining to the 2HDM, with a particular emphasis on the so-called wrong sign limit, which is only possible in certain types of 2HDM and has been the subject of some debate in the literature. A large number of flavour observables comprise Sec. 4.4, along with the global fit to all constraints. Beyond this, the LHC has performed numerous searches for BSM Higgs states over the years, and this data can be couched in terms of constraints on the 2HDM parameter space and further extrapolated to the expected performance of the HL-LHC in Sec. 4.5. These dovetail nicely with the flavour constraints to provide complimentary limits. Other sections include an examination of the possibility of the 2HDM being able to facilitate the SFOEWPT required by the Sakharov criteria (Sec. 4.6), the anomalous magnetic moment of the muon (Sec. 4.7), and the impact of the MUonE experiment (Sec. 4.8). Matters are brought to a close in Sec. 4.9.

---

[1] https://flav-io.github.io

4.1 The Two Higgs Doublet Model

In another shocking twist of the vibrant nomenclature of physics, the two Higgs doublet model invokes two Higgs doublets. This stands in contrast to the SM, with its paltry single doublet, making use of the conjugate of said doublet to give mass to both up- and down-type quarks, as outlined in Sec. 2.2. Instead, two distinct complex scalar doublets are deployed to this end,

$$\Phi_i = \begin{pmatrix} \phi_i^+ \\ (v_i + \phi_i^0 + iG_i^0)/\sqrt{2} \end{pmatrix}, \tag{4.1}$$

with $i = 1, 2$. The process of EWSB occurs much as in the SM, with the weak bosons acquiring mass and the Higgs VEV giving rise to mass terms for fermions in the full Lagrangian. There are of course some differences. First, the two doublets acquire different VEVs, which can be related to the original SM VEV v as $v^2 = v_1^2 + v_2^2$. Secondly, and of more phenomenological interest, is the resultant particle spectrum. As both of the doublets have four degrees of freedom, there are a total of 8 in this construction. As EWSB proceeds as before, three of these are said to be “eaten” when they become the longitudinal polarisations of the now massive weak bosons, leaving a total of five, corresponding to five physical states. Thus, by introducing a single additional doublet, an additional four Higgs bosons come into play. Two of these five are charged scalars, $H^\pm$, two are neutral scalars, H^0, h^0 and one is a neutral pseudoscalar, A^0. With H^0 as the heavier of the two neutral scalars and no scalar observed below the SM Higgs mass of 125 GeV, here it is assumed that h^0 is this SM-like particle.

The potential for the 2HDM studied here is given by [196]

$$\begin{aligned} V(\Phi_1, \Phi_2) = {} & m_{11}^2 \Phi_1^\dagger \Phi_1 + m_{22}^2 \Phi_2^\dagger \Phi_2 - m_{12}^2 (\Phi_1^\dagger \Phi_2 + \Phi_2^\dagger \Phi_1) + \frac{\lambda_1}{2} (\Phi_1^\dagger \Phi_1)^2 + \frac{\lambda_2}{2} (\Phi_2^\dagger \Phi_2)^2 \\ & + \lambda_3 (\Phi_1^\dagger \Phi_1)(\Phi_2^\dagger \Phi_2) + \lambda_4 (\Phi_1^\dagger \Phi_2)(\Phi_2^\dagger \Phi_1) + \frac{\lambda_5}{2} \left[(\Phi_1^\dagger \Phi_2)^2 + (\Phi_2^\dagger \Phi_1)^2 \right], \end{aligned} \tag{4.2}$$

where the lambda basis has been used. This potential opens up an avenue for tree level flavour changing neutral currents, through terms in which fermions may couple to both doublets, but such interactions are experimentally ruled out. To overcome this difficulty a $\mathbb{Z}_2$ symmetry is imposed, such that each fermion type couples only to a single doublet [197]. In terms of the charges under the $\mathbb{Z}_2$ symmetry, Φ_1 is positively charged and Φ_2 is negatively charged, and between them the fermions can have four possible non-trivial arrangements, which dictate which doublet each class

Model	I	II	X	Y
u_R	Φ_2	Φ_2	Φ_2	Φ_2
d_R	Φ_2	Φ_1	Φ_2	Φ_1
e_R	Φ_2	Φ_1	Φ_1	Φ_2

Table 4.1: Types of 2HDM with natural flavour conservation.

of fermions couples to. These four possible configurations correspond to four different types of 2HDM, which are set out in Table 4.1, and will be referred to as e.g. 2HDM-II. Note that by convention Φ_2 always couples to the up-type quarks, and also that the 2HDM-X and 2HDM-Y are sometimes known as the lepton-specific and flipped models respectively. The $\mathbb{Z}_2$ symmetry is softly broken by the m_{12}^2 term so as to prevent the problem of domain walls.

The set of λ_i comes in handy for enforcing theoretical constraints, which are explored in Sec. 4.2, in addition to probing the nature of the EWPT in Sec. 4.6, but the more useful set of parameters is the mass basis. To transform between the two bases, note that the parameters m_{11}^2 and m_{22}^2 are related to v_1 and v_2 as [181]

$$m_{11}^2 = m_{12}^2 \frac{v_2}{v_1} - \lambda_1 \frac{v_1^2}{2} - (\lambda_3 + \lambda_4 + \lambda_5)\frac{v_2^2}{2}, \tag{4.3}$$

$$m_{22}^2 = m_{12}^2 \frac{v_1}{v_2} - \lambda_2 \frac{v_2^2}{2} - (\lambda_3 + \lambda_4 + \lambda_5)\frac{v_1^2}{2}. \tag{4.4}$$

Expressions that yield the masses of the Higgs bosons can then be found as [198]

$$\begin{aligned} m_{H^0}^2 = {} & \frac{m_{12}^2}{\sin\beta\cos\beta}\sin^2(\beta-\alpha) \\ & + v^2\left[\lambda_1\cos^2\alpha\cos^2\beta + \lambda_2\sin^2\alpha\sin^2\beta + \frac{\lambda_3+\lambda_4+\lambda_5}{2}\sin 2\alpha\sin 2\beta\right], \end{aligned} \tag{4.5}$$

$$\begin{aligned} m_{h^0}^2 = {} & \frac{m_{12}^2}{\sin\beta\cos\beta}\cos^2(\beta-\alpha) \\ & + v^2\left[\lambda_1\sin^2\alpha\cos^2\beta + \lambda_2\cos^2\alpha\sin^2\beta - \frac{\lambda_3+\lambda_4+\lambda_5}{2}\sin 2\alpha\sin 2\beta\right], \end{aligned} \tag{4.6}$$

$$m_{A^0}^2 = \frac{m_{12}^2}{\sin\beta\cos\beta} - \lambda_5 v^2, \tag{4.7}$$

$$m_{H^\pm}^2 = \frac{m_{12}^2}{\sin\beta\cos\beta} - \frac{\lambda_4+\lambda_5}{2}v^2. \tag{4.8}$$

This mass basis shifts the focus to a total of 8 parameters; the four particle masses, the mixing angles α and β, the softly $\mathbb{Z}_2$ breaking term m_{12}, and the VEV v. As mentioned above, h^0 is identified as the observed SM-like Higgs, and additionally the VEV is taken to be that of the SM, so $v = 246$ GeV. Furthermore, m_{12} can be put aside for now as it plays no role in the analyses of Sec. 4.3 and Sec. 4.4. The angles α and β, describing the mixing of the neutral and charged Higgs fields, respectively, satisfy the relations [198]:

$$\tan\beta = \frac{v_2}{v_1}, \tag{4.9}$$

$$\tan 2\alpha = \frac{2\left(-m_{12}^2 + (\lambda_3+\lambda_4+\lambda_5)v_1v_2\right)}{m_{12}^2\left(v_2/v_1 - v_1/v_2\right) + \lambda_1 v_1^2 - \lambda_2 v_2^2}. \tag{4.10}$$

By taking the alignment limit, in which $\cos(\beta-\alpha)$ is small, a limit of which much more hay will be made in Sec. 4.3, the λ_i can be expressed in terms of the physical parameters in a relatively simple form [199, 200]:

$$v^2\lambda_1 = m_{h^0}^2 - \frac{\tan\beta(m_{12}^2 - m_{H^0}^2\sin\beta\cos\beta)}{\cos^2\beta}, \tag{4.11}$$

$$v^2\lambda_2 = m_{h^0}^2 - \frac{m_{12}^2 - m_{H^0}^2\sin\beta\cos\beta}{\tan\beta\sin^2\beta}, \tag{4.12}$$

$$v^2\lambda_3 = m_{h^0}^2 + 2m_{H^+}^2 - m_{H^0}^2 - \frac{m_{12}^2}{\sin\beta\cos\beta}, \tag{4.13}$$

$$v^2\lambda_4 = m_{A^0}^2 - 2m_{H^+}^2 + \frac{m_{12}^2}{\sin\beta\cos\beta}, \tag{4.14}$$

$$v^2\lambda_5 = -m_{A^0}^2 + \frac{m_{12}^2}{\sin\beta\cos\beta}. \tag{4.15}$$

After EWSB, the Yukawa component of the Lagrangian can be written as [196, 201]

$$\begin{aligned}\mathcal{L}_{\text{Yukawa}}^{\text{2HDM}} &= -\sum_{f=u,d,\ell}\frac{m_f}{v}\left(\xi_h^f\,\bar{f}fh + \xi_H^f\,\bar{f}fH - i\xi_A^f\,\bar{f}\gamma_5 fA\right) \\ &\quad - \left[\frac{\sqrt{2}V_{ud}}{v}\bar{u}\left(m_d\,\xi_A^d P_R - m_u\,\xi_A^u P_L\right)dH^+ + \frac{\sqrt{2}}{v}m_\ell\,\xi_A^l(\bar{\nu}P_R\ell)H^+ + \text{h.c.}\right],\end{aligned} \tag{4.16}$$

where the coupling strengths ξ depend upon the type of 2HDM in question, with a breakdown of these given in Table 4.2.

Model	I	II	X	Y
ξ_h^u	$\cos\alpha/\sin\beta$	$\cos\alpha/\sin\beta$	$\cos\alpha/\sin\beta$	$\cos\alpha/\sin\beta$
ξ_h^d	$\cos\alpha/\sin\beta$	$-\sin\alpha/\cos\beta$	$\cos\alpha/\sin\beta$	$-\sin\alpha/\cos\beta$
ξ_h^l	$\cos\alpha/\sin\beta$	$-\sin\alpha/\cos\beta$	$-\sin\alpha/\cos\beta$	$\cos\alpha/\sin\beta$
ξ_H^u	$\sin\alpha/\sin\beta$	$\sin\alpha/\sin\beta$	$\sin\alpha/\sin\beta$	$\sin\alpha/\sin\beta$
ξ_H^d	$\sin\alpha/\sin\beta$	$\cos\alpha/\cos\beta$	$\sin\alpha/\sin\beta$	$\cos\alpha/\cos\beta$
ξ_H^l	$\sin\alpha/\sin\beta$	$\cos\alpha/\cos\beta$	$\cos\alpha/\cos\beta$	$\sin\alpha/\sin\beta$
ξ_A^u	$\cot\beta$	$\cot\beta$	$\cot\beta$	$\cot\beta$
ξ_A^d	$\cot\beta$	$-\tan\beta$	$\cot\beta$	$-\tan\beta$
ξ_A^l	$\cot\beta$	$-\tan\beta$	$-\tan\beta$	$\cot\beta$

Table 4.2: Coupling strengths ξ in each type of 2HDM between the Higgs particles and fermions.

To go into further detail about the aforementioned alignment limit, it is perhaps most instructive to pick a specific example and demonstrate the nature of this limit, whilst pointing out that this applies to each of the four types of 2HDM studied here. In short, the alignment limit recovers exactly the phenomenology of the SM Higgs for the h^0 boson and is achieved by setting $\cos(\beta-\alpha)=0$. To see this, note that, focussing on the gauge and Yukawa couplings of h^0, the relevant Lagrangian terms can be written as [202]:

$$\mathcal{L}_{h^0} = \kappa_V \frac{m_Z^2}{v} h^0 Z_\mu Z^\mu + \kappa_V \frac{2m_W^2}{v} h^0 W_\mu^+ W^{\mu-} - \sum_{f=u,d,\ell} \kappa_f \frac{m_f}{v} h^0 \bar{f} f, \tag{4.17}$$

with a slight change of notation, switching the ξ_i for κ_i in order to match the experimental conventions for Higgs coupling modifiers for the observed Higgs. Following Table 4.2 and through some trigonometric manipulation, these coupling modifiers in the 2HDM-II are given by

$$\begin{aligned} \kappa_V &= \sin(\beta-\alpha), \\ \kappa_u &= \sin(\beta-\alpha) + \cot\beta\cos(\beta-\alpha), \\ \kappa_{d,\ell} &= \sin(\beta-\alpha) - \tan\beta\cos(\beta-\alpha). \end{aligned} \tag{4.18}$$

Clearly the SM case, $\kappa_i = 1$, can be recovered when $\cos(\beta-\alpha)=0$, a result that holds for each of the 2HDM types. Note that κ_V is type independent. As a result, it makes more sense to tweak the parameter basis studied, replacing α and β with $\cos(\beta-\alpha)$ and $\tan\beta$.

4.2 Theoretical and Electroweak Precision Constraints

The requirements of pertubativity can be expressed straightforwardly in the lambda basis as $|\lambda_i| \leq 4\pi$, but it is important to be aware that this is not a direct experimental constraint after the fashion of those explored in the rest of this chapter, but rather a statement about the ability to perform calculations within the framework of the model. As such, the choice of 4π as a limit is somewhat arbitrary, with a bound of 4 being used in some other works [203, 204], but the results found are independent of this choice, and so the less conservative limit is chosen to allow exploration of more extreme parameter regions.

Additional perturbativity constraints can be gleaned from the Yukawa sector of Eq. (4.16). Again picking out the 2HDM-II as a particularly instructive example this yields bounds of

$$\begin{aligned} \frac{\sqrt{2}\,V_{tb}\,m_t\cot\beta}{2v} &\leq \sqrt{4\pi} \quad \Rightarrow \quad \tan\beta > 0.14\,, \\ \frac{\sqrt{2}\,V_{tb}\,m_b\tan\beta}{2v} &\leq \sqrt{4\pi} \quad \Rightarrow \quad \tan\beta < 300\,. \end{aligned} \tag{4.19}$$

These bounds inform the choice of the range of $\tan\beta$ explored in this chapter; a choice is made to explore within a lower bound $\tan\beta = 10^{-1.5} \approx 0.03$ and an upper bound of $\tan\beta = 10^{2.5} \approx 300$ across each type of 2HDM.

The conditions for a stable vacuum are applied as set out in Ref. [205], whilst demanding the vacuum to be the global minimum of the potential [206]. The conditions from tree-level unitarity, see Refs. [207, 208][2], are also considered, alongside next–to–leading order (NLO) unitarity and the condition that NLO corrections to partial wave amplitudes are suppressed relative to leading order (LO) contributions, see Refs. [203, 204]. The key result from the enforcement of these conditions is also independent of the type of 2HDM examined and is shown in Fig. 1 of Ref. [3], with the main takeaway being that the masses of the new Higgses must obey a degree of mass degeneracy, which becomes particularly strict for masses above 1 TeV.

The expressions for the electroweak precision observables (EWPOs) S, T, and U [153, 154] in the 2HDM (derived from Ref. [210]) are given explicitly in Appendix C of Ref. [3]. Whilst S and T correspond to distinct dimension-6 operators in the EFT expansion, U corresponds to a dimension-8 operator and so is suppressed by a factor Λ^2/m_Z^2 compared to S and T [211, 212]. As a result, NP has generally small effects on this parameter and the common approach is therefore

---

[2] For a similar discussion in an alternative lambda basis see Ref. [209].

to set $U = 0$ in BSM fits, as detailed in Refs. [155, 213], and this is done here. This leads to a reduction in the experimental uncertainties for T as T and U are correlated as they are both concerned with charged weak currents. The EWPOs are included in the global fit of all observables.

4.3 Higgs Signal Strengths

This section deals with the signal strengths of the observed SM-like Higgs boson, h^0, which are defined in such a way as to give rapid insight into how closely or otherwise this observed boson does indeed match the phenomenology of the SM case. Deviations from this behaviour open the way for modifications to the nature of h^0, such as it truly being the lighter neutral boson of the 2HDM. As the cross section and branching ratio of a given channel cannot be measured separately without making further assumptions, the two are combined into the signal strength measurement. So, for a given Higgs production mode i of cross section σ_i and a decay channel f with a branching fraction $\mathcal{B}_f$, the signal strength is given by

$$\mu_i^f = \frac{(\sigma_i \cdot \mathcal{B}_f)_{\text{Exp.}}}{(\sigma_i \cdot \mathcal{B}_f)_{\text{SM}}}. \tag{4.20}$$

Clearly, the expectation from the SM is that all of these measurements resolve to unity, with discrepancies indicating possible hints of BSM physics at play. Unfortunately, small cross sections and branching fractions make some channels too experimentally challenging to observe at the LHC, but 31 channels do not suffer from this problem and so are included in this analysis. These measurements, from Refs. [191, 214–219], are collected in Table 4 of Ref. [3]. When only a single combined measurement is measured experimentally this is assumed to correspond to the gluon fusion production, as this is by far the dominant Higgs production mechanism at the LHC (see Sec. 2.4). When correlation matrices are provided, these are additionally included in the analysis, and when multiple recent measurements are available for a single channel, an average is taken; steps which give useful boosts to the sensitivity. As the observed Higgs matches the SM predictions to within $\sim 10\%$, one would naively expect to find that the 2HDM is driven towards the alignment limit.

The modifications to the couplings of h^0 that arise in the 2HDM as compared to the SM, as given in Table 4.2 can then be probed using these measurements. In particular, the parameters on which these coupling modifiers depend can be examined, which, for the purposes of this chapter, are $\tan\beta$ and $\cos(\beta-\alpha)$. This is done by this by performing a fit using analytical calculations of the signal strengths in the 2HDM as functions of the input parameters from expressions given in Ref. [33] and directly feeding the resulting 2HDM predictions into the FLAVIO framework, along with the experimental measurements, to ensure a consistent approach between this analysis and the flavour observables of the following section. The results presented in Fig. 4.1, with the goal of constraining the $\tan\beta - \cos(\beta-\alpha)$ plane, with contours shown up to the 5σ level to make sure the wrong sign limit regions are visible, where applicable (see below). The contributions of the additional new Higgs bosons to the loop-level processes have been neglected as they are negligible for the allowed masses found in Sec. 4.4. Similar analyses have been performed in Refs. [193, 199, 202, 220, 221].

In the 2HDM-I case, sizeable deviations from the alignment limit are allowed, increasingly so for increasing $\tan\beta$, with an ultimate limit at the 2σ confidence level of $|\cos(\beta-\alpha)| \leq 0.21$ for sufficiently large $\tan\beta \geq 10$. In contrast, for the 2HDM-II the alignment limit must be closely followed; at 2σ $|\cos(\beta-\alpha)| \leq 0.050$, with the maximum allowed value of $\cos(\beta-\alpha)$ occurring at $\tan\beta \approx 1$. Due to the dependence of $\kappa_{d,\ell}$ on $\tan\beta$ in this model, the maximum value falls significantly once away from $\tan\beta \approx 1$, such that at large values of $\tan\beta$, the alignment limit must be strictly followed and it is valid to set $\cos(\beta-\alpha) = 0$. In the 2HDM-X, putting aside the question of the wrong sign limit for just a moment, $|\cos(\beta-\alpha)| \leq 0.10$ at 2σ, which falls rapidly once $\tan\beta$ is away from ~ 1, with only very small $\cos(\beta-\alpha)$ allowed for extreme values of $\tan\beta$. The leptonic decays of h^0 are still important here as they restrict $\cos(\beta-\alpha)$ to be small for large values of $\tan\beta$, which differentiates these results from the 2HDM-I. Finally, for the 2HDM-Y, in which the quark sector matches that of the 2HDM-II, the contours are very similar between the two types, with $|\cos(\beta-\alpha)| \leq 0.049$ at 2σ, indicating a lack of sensitivity to the lepton couplings in this analysis.

4.3.1 The Wrong Sign Limit

As alluded to above, and visible as a dashed red line on Fig. 4.1, there is another limit of interest in addition to the alignment limit. This is known as the wrong sign limit, in which the coupling modifiers have the same magnitude at unity, but with configurations of the lepton and down-type quark couplings taking values of -1. This has been touted as a possible way a fourth sequential chiral generation of fermions may yet remain hidden in the current LHC data [222], even as such a model, without any further BSM additions, has been definitively ruled out [223–225]. In the 2HDM-II the couplings with the negative sign are posited to be those to the down-type quarks

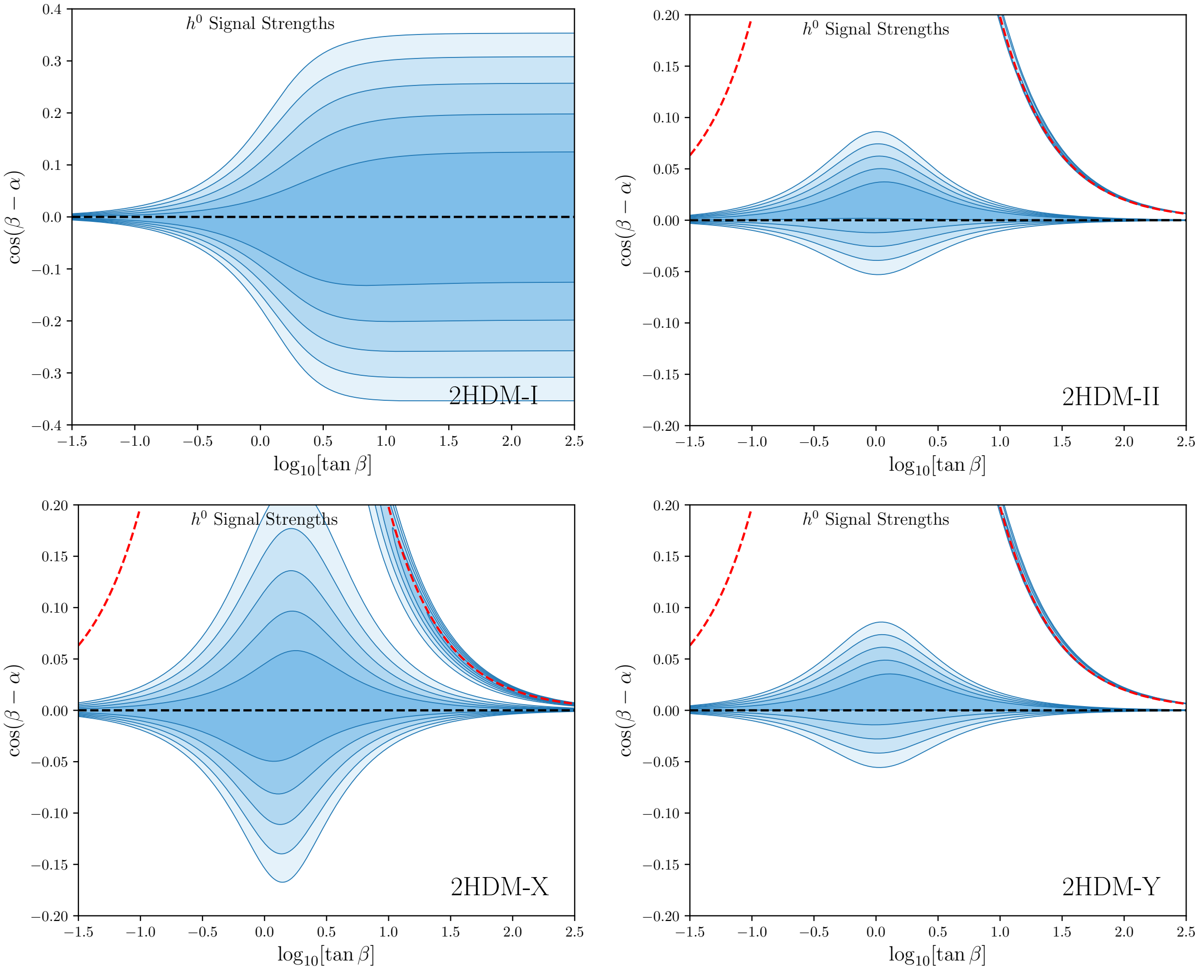

Figure 4.1: Contour plot of the allowed 2HDM parameter space for each type of 2HDM, with the contours indicating the allowed regions at confidences of 1, 2, 3, 4, 5σ from dark to light. The alignment and wrong sign limits (where applicable) are shown as black and red dashed lines respectively. Note that the range of $\cos(\beta-\alpha)$ shown is twice as large for 2HDM-I.

and leptons, in the 2HDM-X the leptons only and in the 2HDM-Y the down-type quarks only. Referring again to Table 4.2 and to Eq. (4.18), enforcing the wrong sign limit yields

$$\cos\left(\beta-\alpha\right)=\sin 2\beta=\frac{2\tan\beta}{1+\tan^2\beta}\,, \tag{4.21}$$

which is the form depicted in Fig. 4.1. No such limit exists in the 2HDM-I due to the structure of this type of 2HDM, with all fermions coupling to the same Higgs doublet.

Perhaps of most note in the investigation of this limit is that the wrong sign limit is found to be excluded up to 2.7σ in the 2HDM-II, a result that improves over the exclusion found in works such as Refs. [199, 216, 226], owing to the larger dataset leveraged here. The case for the 2HDM-Y has the wrong sign allowed up to 2.6σ, with the similarity to the 2HDM-II result arising as a consequence of the two types having the same quark sector couplings and there being a relative lack of sensitivity to the sign of the lepton coupling modifiers. The latter is due to the lepton contributions being less important in this sector than those of the quarks, especially in the case of the loop level processes through which sensitivity to the sign of the coupling modifiers comes. In particular, the leptons do not contribute at all to the important gluon fusion production calculations, while their contributions to the diphoton and $Z\gamma$ decays are orders of magnitude lower than those from the quarks and the $W^{\pm}$ boson for a SM-like h^0. For the 2HDM-X, the wrong sign limit is allowed at all confidence levels examined, which can again be attributed to the lack of sensitivity to the sign of κ_ℓ.

As the 2HDM-II is the most commonly studied of the 2HDM types, it is perhaps prudent to drill further down into the details of the wrong sign limit for this specific model. To do so, the coupling modifiers are examined directly, i.e. independently of the forms given in Eq. (4.18), which is worth stressing. This is done in the $\kappa_u - \kappa_{d,\ell}$ plane, where κ_V has been fixed to its value from the best fit point of a fit performed on all the κ_i, found to be $\kappa_V = 1.036$.

The results from this fit are shown in Fig. 4.2, with the alignment and wrong sign limits shown in black and red respectively. This does not directly exclude $\kappa_d = -1$, in line with the current lack of sensitivity to the sign of κ_d at the LHC. However, then looking to generate κ_u and κ_d values within the 2σ allowed region close to $\kappa_d = -1$ by using Eq. (4.18), the only solutions require $|\cos(\beta - \alpha)| \gtrsim 0.96$. Clearly, such extremal values of $\cos(\beta - \alpha)$ are not compatible with the best fit fixed value of $\kappa_V = 1.036$ in the 2HDM, so this 2σ allowed region in the $\kappa_u - \kappa_{d,\ell}$ plane cannot be attained in the 2HDM-II. So, whilst the general principle of $\kappa_d = -1$ is not excluded, the wrong sign limit in full can be excluded up to 2.7σ in the 2HDM-II. More generally, when $\kappa_{d,\ell} = -1$, any small deviation from $\kappa_u = 1$ has a large impact, pushing $\cos(\beta - \alpha)$ to the incompatible regions of the parameter space. Further clarity on the wrong sign limit may be achieved through future collider data [227, 228].

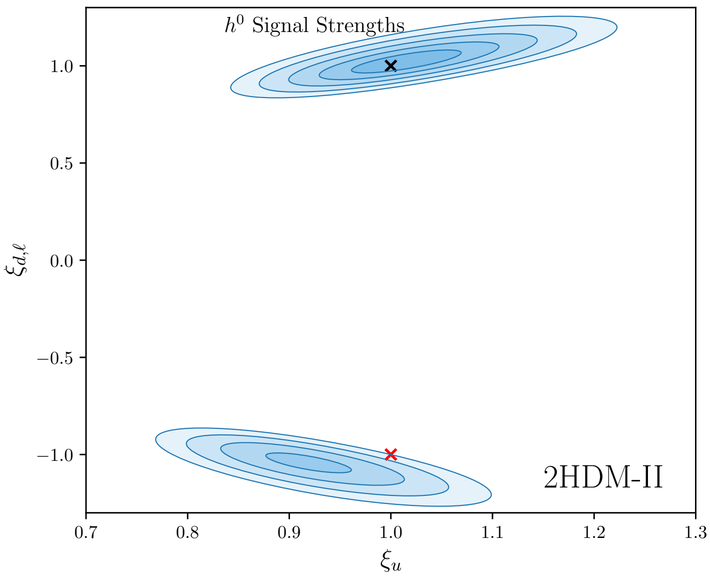

Figure 4.2: Contour plot of the coupling constant modifiers, in which κ_V is fixed to its best fit value with marks for the alignment (wrong-sign) limit in black (red). The contours indicate the allowed space at 1, 2, 3, 4, 5σ from dark to lighter.

4.4 Flavour Observables

The flavour sector comprises the brunt of the observables that are fed into the global fit. This section of the chapter proceeds one class of observable at a time, highlighting the mechanisms through which the 2HDM contributes to each process and how this can be used to constrain the parameter space of the model. Whilst there are additional complexities to consider in some cases, it is the $\tan\beta - m_{H^\pm}$ plane that is constrained here, with contours shown up to 5σ when regions of note are only visible at this level and 2σ otherwise. As a general and overly simplified rule of thumb, the 2HDM contributions come from $H^\pm$ acting in addition to the SM $W^\pm$ in mediating interactions. The observables considered here are listed in detail with SM predictions and experimental measurements collated from Refs. [77, 98, 191, 213–215, 217–219, 229–266] in the ancillary materials of Ref. [7], and it is to there that the interested reader is directed. As has already been remarked upon, the lepton couplings are, for the most part, less significant than the quark sector couplings, and so the contour plots shown are for the more commonly studied 2HDM of Types I and II, which has the additional benefit of reducing inefficiencies and clutter as compared to showing the plots for every observable for each four 2HDM types. The global fits for all four types are shown when all observables are combined.

It is worth drawing the reader's attention to one particular subtlety regarding the CKM matrix. Conventionally, the CKM matrix elements are extracted from experimental measurements of semi-leptonic decays, with the inherent assumption that the branching ratio measured is that of the SM. If nature has in fact manifested the 2HDM, then this assumption falls down. In the case of leptonic meson decay in the 2HDM,

$$\mathcal{B}_{\text{2HDM}} = \mathcal{B}_{\text{SM}} \times (1 + \delta_{\text{2HDM}})^2, \tag{4.22}$$

where δ_{2HDM} is the 2HDM correction factor, and so the extracted CKM element, acting under the SM assumption, will be out by a factor $(1 + \delta_{\text{2HDM}})$. Similar arguments hold for semi-leptonic meson decays. The accepted CKM accepted values are commonly taken from leptonic and semi-leptonic tree-level decays. Scanning across the 2HDM parameter space considered here using the tree level parameterisation for V_{us}, V_{ub} and V_{cb} and CKM unitarity, it is found that the impact of these effects on the CKM elements is negligible in the regions allowed by the other constraints considered below. Thus it is safe to use the measured values. Were the 2HDM discovered, there would be some small modifications but these need not be accounted for here.

4.4.1 Leptonic and Semi-leptonic Tree-Level Meson Decays

First off, the tree-level (semi-)leptonic flavour-changing charged transitions will be examined, wherein the 2HDM contributes through the effective operators

$$\mathcal{O}_{S-P} = (\bar{u} P_L\, d)(\bar{\ell} P_L \nu_\ell), \qquad \mathcal{O}_{S+P} = (\bar{u} P_R\, d)(\bar{\ell} P_L \nu_\ell). \tag{4.23}$$

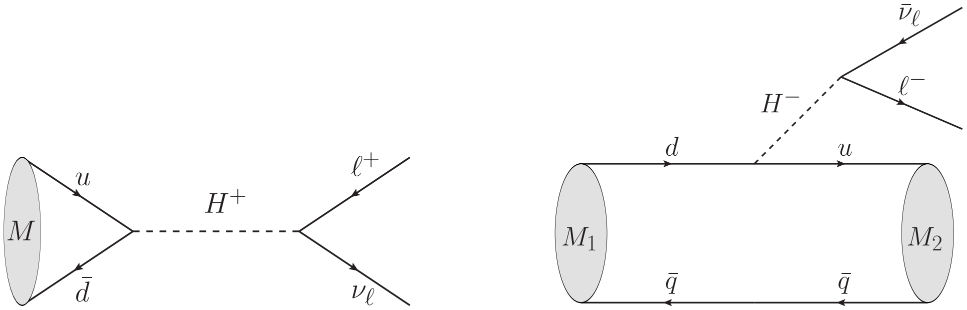

Figure 4.3: Diagrams contributing to leptonic (left) and semi-leptonic (right) decays in the 2HDM.

The precise form of the WCs for these operators depends on the type of 2HDM, with the full expressions and relevant basis translations given in Refs. [3, 201, 267–269]. For the relevant Feynman diagrams, again pointing out that much of this section proceeds with the replacement of the charged weak bosons with the charged Higgs bosons, see Fig. 4.3.

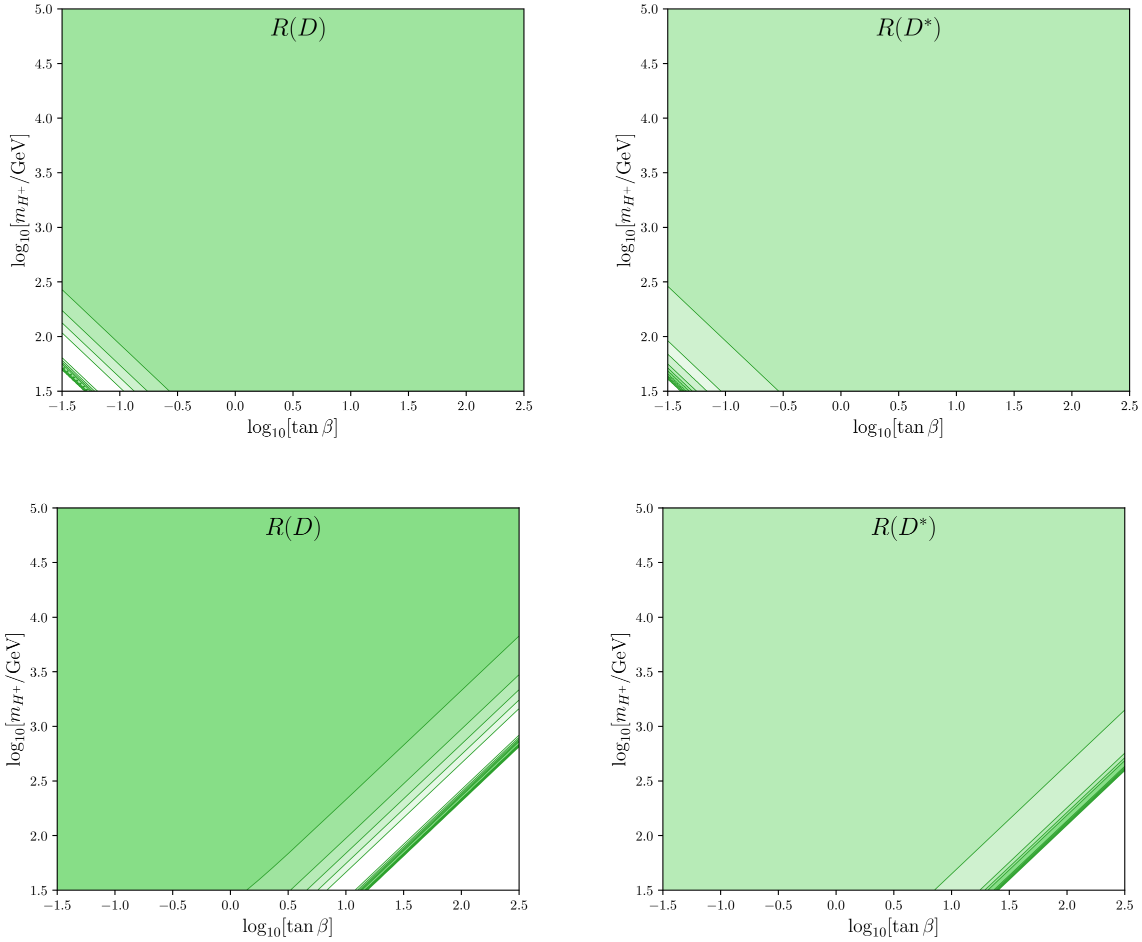

Figure 4.4: Contour plot of the allowed parameter space for the 2HDM-I (top) and 2HDM-II (bottom) in the ($\tan\beta - m_{H^\pm}$) plane, originating from $R(D)$ (left) and $R(D^*)$ (right). Contours are shown at 1, 2, 3, 4, 5σ confidence from darkest to lightest.

First on this path sit the Lepton-Flavour Universality (LFU) observables

$$R(D^{(*)}) \equiv \frac{\mathcal{B}(B \to D^{(*)}\tau\bar{\nu}_\tau)}{\mathcal{B}(B \to D^{(*)}\ell\bar{\nu}_\ell)}, \tag{4.24}$$

where $\ell = e, \mu$, wherein lie possible hints of LFU violation [270, 271], with the combined measurements sitting at a tension of 3.2σ with the SM [234]. This can occur in the 2HDM through the couplings of the charged Higgs to leptons, which depends on the lepton mass.

The resulting contour plots in the 2HDM parameter space for Types I and II are shown in Fig. 4.4. For the 2HDM-I, even though $R(D)$ is 1.2σ away from the SM, much of the space is allowed only within 2σ, whereas $R(D^*)$ can only be accommodated at or above 2.8σ, in line with its SM tension. Looking at both observables, they drive a best fit point down to $m_{H^\pm} \sim 1\,\mathrm{GeV}$, well outside of the feasible parameter space for the 2HDM, while within the parameter space they exhibit a combined minimum tension of 3.5σ between the 2HDM-I and the data. This is because the 2HDM contributions to the semi-leptonic $b \to c\ell\bar{\nu}_\ell$ transitions are of opposing sign to the SM and so $R(D)$ and $R(D^*)$ are forced further away from the data, save for the narrow region in which the 2HDM contributions are twice that of the SM. The situation is similar in the other types of 2HDM; in the 2HDM-II the combined tension exceeds that of the SM, at 3.5σ. In Fig. 4.5, the combined fit to all the tree-level flavour-changing charged currents is shown.

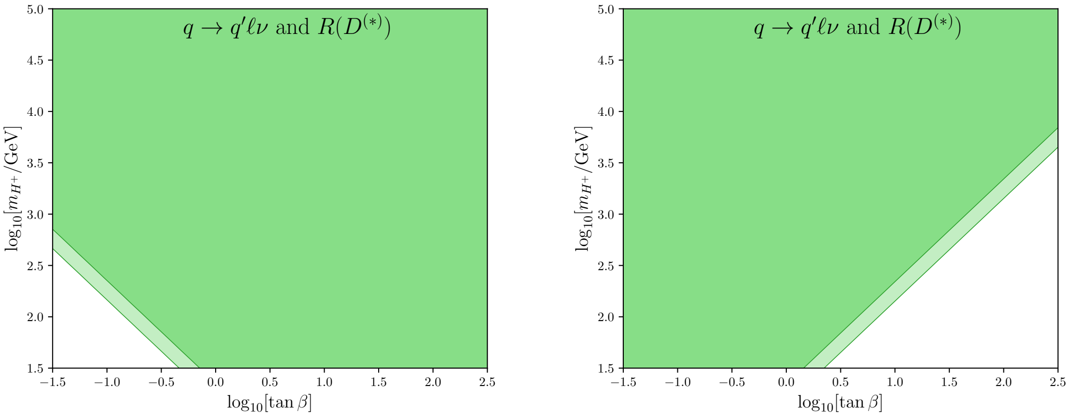

Figure 4.5: Contours of the allowed regions for the 2HDM-I (left) and 2HDM-II (right) in the $(\tan\beta - m_{H^\pm})$ plane, from the combined tree-level leptonic and semi-leptonic decays of B, B_s, D, D_s, K, and π mesons and the hadronic decays of τ leptons to K and π mesons with ν_τ addition to $R(D)$ and $R(D^*)$. The lighter contour is the 2σ confidence level, the darker 1σ.

4.4.2 Neutral B-Meson Mixing

The neutral mesons $B_{s,d}$ undergo mixing, and the mass difference between the light and heavy eigenstates has been very well measured experimentally, at the level of $\sim \mathcal{O}(0.1\%)$ [213, 272] for both $\Delta m_{d,s}$, making these observables of significant interest in flavour physics [273]. The relevant Feynman diagrams, known as box diagrams, in the 2HDM, are shown in Fig. 4.6. That said, there are some wrinkles on the theoretical prediction side, with the uncertainties mainly stemming from the non-perturbative determinations of the matrix elements of the $\Delta B = 2$ operators. The values used are the averages presented in Ref. [273] from combining heavy quark effective theory (HQET) sum rules [274–276] and lattice calculations [277–279], yielding a theory precision of $\mathcal{O}(5\%)$. The perturbative SM corrections are known and implemented to NLO-QCD accuracy [280].

The dominant contributions in the 2HDM come from the top quark to charged Higgs boson coupling, as the mass suppression renders the contributions from the down-type quarks less relevant. As the couplings between the up-type quarks and $H^\pm$ are the same in each type of 2HDM, the resulting fits to $\Delta m_{d,s}$ are similar across the board. The operators in question are defined (for $q = d, s$) as

$$
\begin{aligned}
\mathcal{O}_1^{(\prime)} &= (\bar{q}^\alpha \gamma^\mu P_{L(R)} b^\alpha)(\bar{q}^\beta \gamma_\mu P_{L(R)} b^\beta), && \\
\mathcal{O}_2^{(\prime)} &= (\bar{q}^\alpha P_{L(R)} b^\alpha)(\bar{q}^\beta P_{L(R)} b^\beta), & \mathcal{O}_4 &= (\bar{q}^\alpha P_L b^\alpha)(\bar{q}^\beta P_R b^\beta), \\
\mathcal{O}_3^{(\prime)} &= (\bar{q}^\alpha P_{L(R)} b^\beta)(\bar{q}^\beta P_{L(R)} b^\alpha), & \mathcal{O}_5 &= (\bar{q}^\alpha P_L b^\beta)(\bar{q}^\beta P_R b^\alpha),
\end{aligned}
\tag{4.25}
$$

with α and β denoting the colour indices.

The expressions of the 2HDM contributions are well established in the literature [201, 281, 282], with those given for the Wilson coefficients $C_k^{(\prime)}$ in Ref. [201] used here, and then converted to

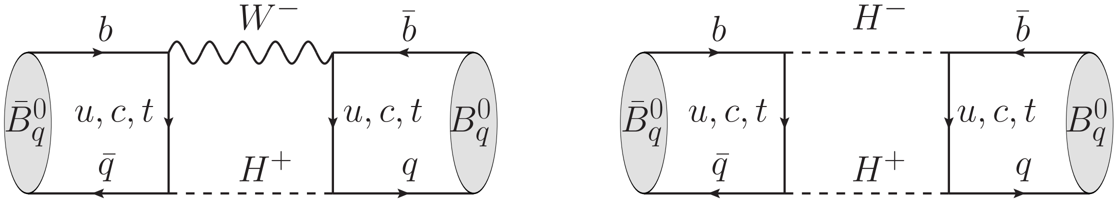

Figure 4.6: Examples of box diagrams describing B_d- and B_s-meson mixing in the 2HDM.

the FLAVIO WET basis [195] as

$$\begin{aligned} C^{bqbq}_{VLL(RR)} &= C_1^{(\prime)}, & C^{bqbq}_{SLR} &= C_4, \\ C^{bqbq}_{SLL(RR)} &= C_2^{(\prime)}, & C^{bqbq}_{VLR} &= -\frac{1}{2}C_5. \end{aligned} \tag{4.26}$$

At leading order in QCD, there is no need to consider the contributions from the $\mathcal{O}_3^{(\prime)}$ operators [201]. The resulting contours are shown in Fig. 4.7, showing weak lower bounds on $\tan\beta$ for lower charged Higgs boson masses in both cases, with some additional exclusion at high $\tan\beta$ in the 2HDM-II case.

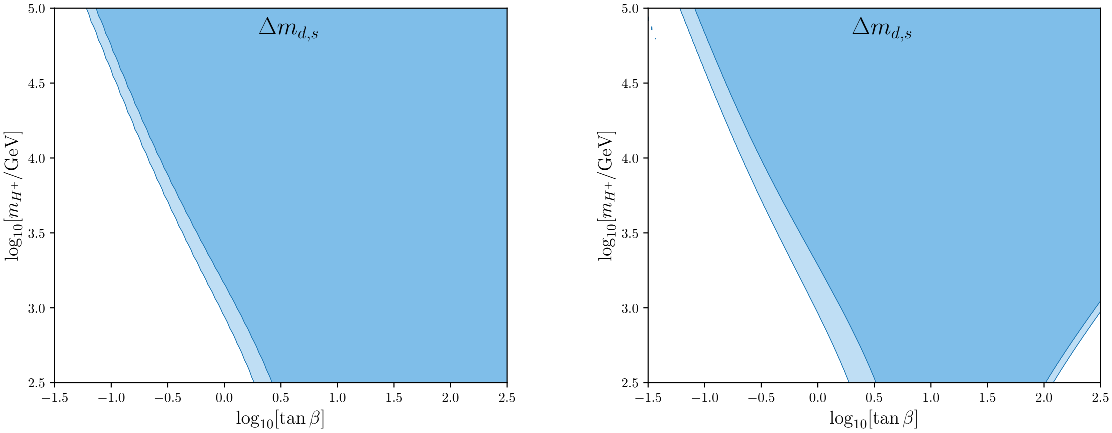

Figure 4.7: Contour plot of the allowed parameter space for the 2HDM-I (left) and 2HDM-II (right) in the $(\tan\beta - m_{H^\pm})$ plane for the combined fit to $\Delta m_{d,s}$. The darker contour indicates allowed parameter space at 1σ confidence, and the lighter at 2σ.

4.4.3 Loop level $b \to s, d$ Transitions

This is a phenomenologically rich sector that encompasses FCNC and processes that have warranted a great deal of study in both the SM and BSM models, owing to apparent tensions between experimental averages and the theoretical predictions in several observables [238, 254–256, 271]. Some examples of these processes are shown in Fig. 4.8.

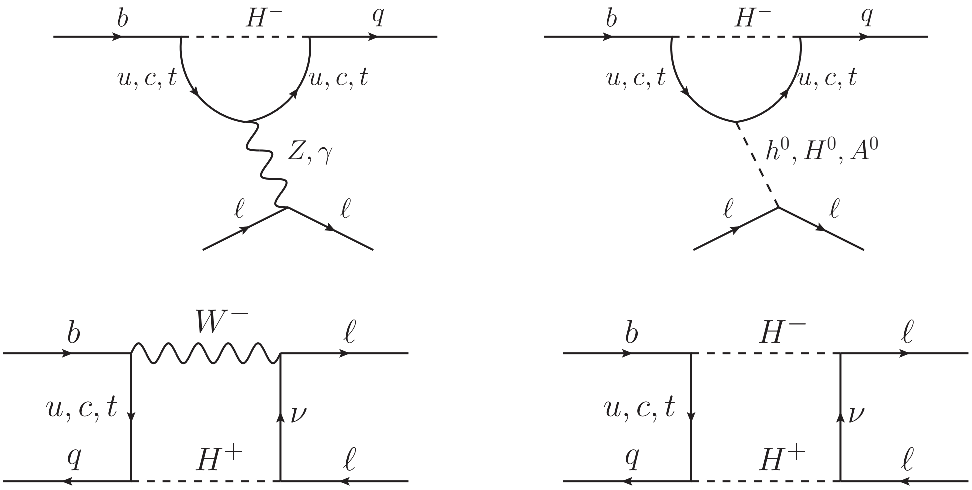

Figure 4.8: Example of diagrams (penguins and boxes) describing the $b \to q\ell^+\ell^-$ transitions in the 2HDM.

The operators of interest are (for $q = d, s$)

$$\begin{aligned}
\mathcal{O}_7^{(\prime)} &= \frac{e\, m_b}{16\pi^2} \big(\bar{q}\sigma^{\mu\nu} P_{R(L)} b\big) F_{\mu\nu}, & \mathcal{O}_8^{(\prime)} &= \frac{g_s\, m_b}{16\pi^2} \big(\bar{q}\sigma^{\mu\nu} P_{R(L)} T^a b\big) G^a_{\mu\nu}, \\
\mathcal{O}_9^{(\prime)} &= \frac{e^2}{16\pi^2} (\bar{q}\gamma_\mu P_{L(R)} b)(\bar{\ell}\gamma^\mu \ell), & \mathcal{O}_{10}^{(\prime)} &= \frac{e^2}{16\pi^2} (\bar{q}\gamma_\mu P_{L(R)} b)(\bar{\ell}\gamma^\mu \gamma_5 \ell), \\
\mathcal{O}_S^{(\prime)} &= \frac{e^2}{16\pi^2} (\bar{q} P_{L(R)} b)(\bar{\ell}\ell), & \mathcal{O}_P^{(\prime)} &= \frac{e^2}{16\pi^2} (\bar{q} P_{L(R)} b)(\bar{\ell}\gamma_5 \ell),
\end{aligned} \tag{4.27}$$

and their forms in the 2HDM can be found in Ref. [201], where it should be noted that $\mathcal{O}_{10}^{(\prime)}$, $\mathcal{O}_S^{(\prime)}$, $\mathcal{O}_P^{(\prime)}$ depend on several 2HDM parameters, in addition to $\tan\beta$ and the charged Higgs boson mass.

Radiative Decay $\bar{B} \to X_s\gamma$

Of particular note in the context of the 2HDM is the radiative decay $\bar{B} \to X_s\gamma$, which is capable of setting a lower limit on the mass of the charged Higgs boson, most notably in the 2HDM-II. The relevant Feynman diagram for the underlying penguin process is shown in Fig. 4.9. On the theory side, this is known to next–to–next–to–leading order (NNLO) in QCD [283] (based on the previous Refs. [284, 285]) in the SM, with an experimental average provided by Ref. [234], deriving from Refs. [286–288].

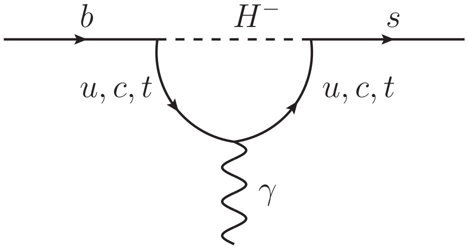

Figure 4.9: One loop penguin contributions to $b \to s\gamma$ in the 2HDM.

The results from this single observable are shown in Fig. 4.10. In the 2HDM-I the constraints on the charged Higgs boson mass are strongly correlated with $\tan\beta$ and so a firm lower mass bound cannot be established in such models. In contrast, as one would expect, $\bar{B} \to X_s\gamma$ does provide a clearer lower mass bound on the charged Higgs boson in the 2HDM-II, with $m_{H^\pm} \gtrsim 790$ GeV at 2σ, which is a key constraint, and this bound becomes stricter with lower $\tan\beta$.

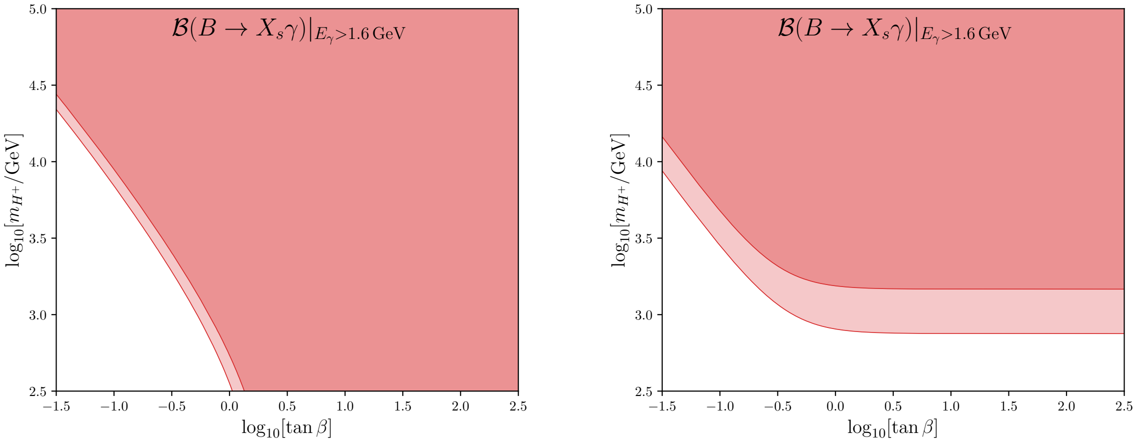

Figure 4.10: Contour plot of the allowed parameter space for the 2HDM-I (left) and 2HDM-II (right) in the $(\tan\beta - m_{H^\pm})$ plane for the radiative decay $B \to X_s\gamma$. The lighter contour indicates the allowed parameter space at 2σ confidence level while the darker contour corresponds to 1σ.

Leptonic $B_{d,s} \to \mu^+\mu^-$ Decays

An additional complexity arises when the FCNC leptonic meson decays $B_{d,s} \to \mu^+\mu^-$ are considered. These processes are particularly sensitive to scalar operator contributions, which makes them ideal for the study of the 2HDM, especially with the wealth of recent experimental measurements available for $B_s \to \mu^+\mu^-$ (with an upper limit set on $B_d \to \mu^+\mu^-$) [289–294], which are combined in Ref. [238]. However, this comes with the penalty of being sensitive to the 2HDM parameters not yet touched on in this section, as well as $\tan\beta$ and $m_{H^\pm}$, so the values of $\cos(\beta-\alpha)$, m_{H^0} and m_{A^0} come into play here. From the results in Sections 4.2 and 4.3, it is valid to take two limits which return the fits to the 2D parameter space explored above, namely the alignment and mass degeneracy limits; $\cos(\beta-\alpha) = 0$ and $m_{H^\pm} = m_{A^0} = m_{H^0}$.

On the theoretical side, the SM prediction takes its lead from perturbative calculations [295–297] and the determinations of the non-perturbative decay constants, such as those performed in Refs. [298–300]. In the 2HDM, previous studies, such as Ref. [301], have concerned themselves primarily with the large $\tan\beta$ limit, in which $\tan\beta \gg \sqrt{m_t/m_b}$, as in this limit the 2HDM contributions can often be simplified. However, much of the parameter space that must needs be examined here lies outwith this limit, and so the more general expressions for the 2HDM contributions as given in Ref. [201] are preferred here.

The results, depicted in Fig. 4.11, are similar for the 2HDM-I to those from $\bar{B} \to X_s\gamma$, with a strong correlation between $\tan\beta$ and $m_{H^\pm}$. In the 2HDM-II the situation is notably different, with the charged Higgs boson mass again having a lower limit, at around 630 GeV at the 2σ level. Whilst this is not as strong a bound as that found from $\bar{B} \to X_s\gamma$, it does increase for both lower and higher values of $\tan\beta$ and so can play an important role in the global fit.

Semi-leptonic $b \to s\ell^+\ell^-$ Transitions

Again, for these observables, all the operators listed in Eq. (4.27) must be accounted for, and thus the alignment and degenerate mass limits are deployed to ensure consistency in the examination of the $\tan\beta - m_{H^\pm}$ plane. Further LFU observables come under scrutiny here, with [302]

$$R_{K^{(*)}} \equiv \frac{\mathcal{B}[B \to K^{(*)}\mu^+\mu^-]}{\mathcal{B}[B \to K^{(*)}e^+e^-]}, \tag{4.28}$$

where the branching fractions are integrated over bins of squared dilepton invariant mass q^2. These have been the focus of quite some attention in recent years [303–310] as a result of measurements previously displaying deviations of up to 3.1σ in R_{K^+} [254–256] from the SM. This focus is helped in part by the comparatively clean nature of these observables in theoretical calculations, as nearly all of the thorny hadronic effects cancel out when taking the ratio, leaving the SM values of $R_{K^{(*)}}$

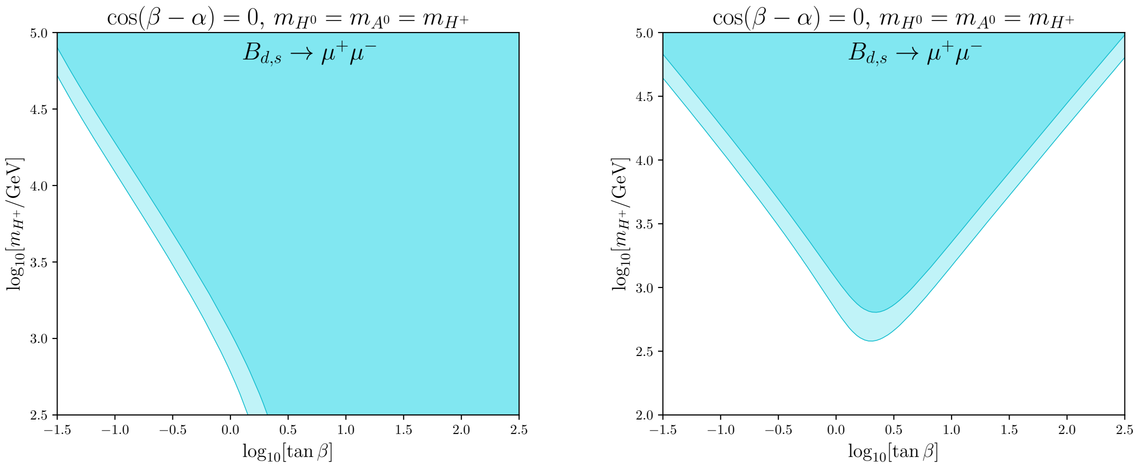

Figure 4.11: Contours of the allowed parameter space for the 2HDM-I (left) and 2HDM-II (right) in the $(\tan\beta - m_{H^\pm})$ plane for the fit to $(B_{d,s}\to\mu^+\mu^-)$, in the alignment and degenerate mass limits. The darker contour indicates the allowed space at 1σ confidence, and the lighter at 2σ.

very close to 1 with tiny uncertainties [311]. The electromagnetic corrections for $R_{K^{(*)}}$ worked out in Ref. [303] were found to be very small, at $\approx 1-2\%$. Model-independent analyses [271, 312–315] show these processes favour vector-like NP in $\mathcal{O}_{9,10}$ for resolution of these deviations. More recently, the tension in these observables has been eliminated due to improvements in the systematic effects, and the current results agree with the SM within 1σ [316].

The results for the 2HDM-I for a combination of all 10 $R_{K^{(*)}}$ bins are shown in the alignment and degenerate mass limits on the left of Fig. 4.12. The majority of the parameter space is allowed at the 1σ level, though there is a disconnected region that arises from the fine-tuning solution wherein the 2HDM-I contributions cancel to zero and the SM result is again recovered. Despite this, a realised 2HDM-I would only increase the tensions between experiment and prediction as compared to the SM, so the 2HDM model comes up short in this respect.

A slightly different approach is required in the 2HDM-II, and it this that is displayed on the right of Fig. 4.12. The 2HDM-II is unable to accommodate the experimental values for the 10 $R_{K^{(*)}}$ bins within the physically relevant parameter space, and so instead the three other pertinent parameters have been fixed to their best fit values from a fit to the 10 $R_{K^{(*)}}$ bins. These values are $\cos(\beta-\alpha) = 0.001$, $m_{H^0} = 250\,\mathrm{GeV}, m_{A^0} = 9.2\ \mathrm{GeV}$. The resulting plot shows that the 2HDM-II can only explain the current experimental values when the charged Higgs boson mass is

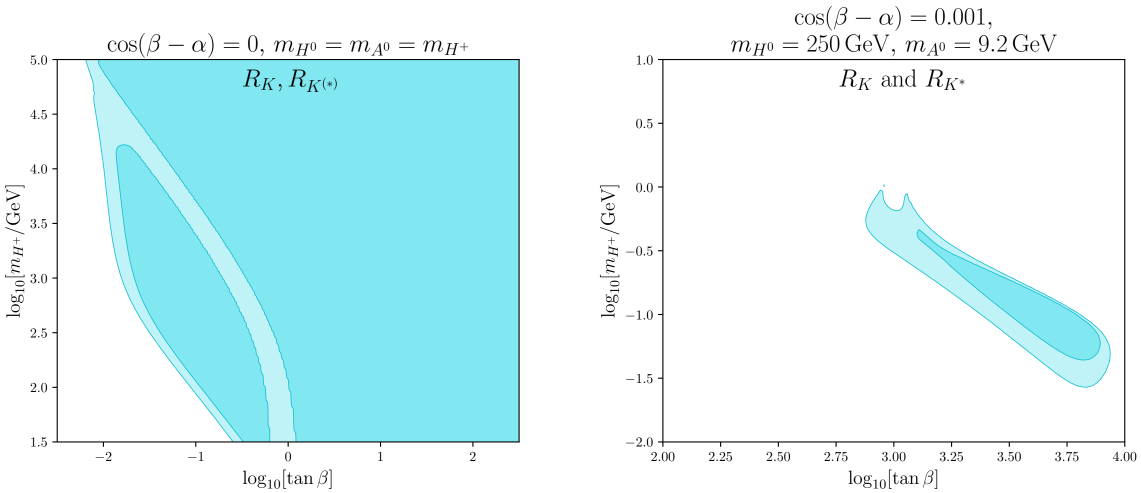

Figure 4.12: Contour plot of the allowed parameter space for the 2HDM-I (left) and 2HDM-II (right) in the $(\tan\beta - m_{H^\pm})$ plane for the $R_{K^{(*)}}$ observables. The lighter contour indicates the allowed parameter space at 2σ confidence level while the darker contour corresponds to 1σ.

very low and $\tan\beta$ is very high; below the GeV level and above around 500 respectively. These contours stand in stark disagreement with the constraints found in other sectors, and furthermore, the relevant WC expressions depend on the assumption that the charged Higgs boson has a mass of at least the electroweak scale [201], so the constraints at such low masses must be called into question from a purely theoretical perspective. As a consequence of this notable discrepancy, the $R_{K^{(*)}}$ and the similarly afflicted LFU ratios $R(D^{(*)})$ are excluded in the global fit of Sec. 4.4.4 and in the consideration of the remaining $b \to s\ell^+\ell^-$ observables below.

A good deal of further $b \to s\ell^+\ell^-$ observables are considered in the overall fit, some of which also currently display tensions with the SM predictions, which reinforces the interest in this sector as a primary indicator of the presence of NP. As such, there have been a number of works examining the BSM implications in detail; see Refs. [238, 261, 304, 306, 309, 310, 312, 313, 317–325]. In short, these processes favour NP contributions from $\mathcal{O}_{9,10}^{(\prime)}$, so the 2HDM is unable to resolve the $R_{K^{(*)}}$ due to the 2HDM contributing primarily to the scalar currents. As a result, the LFU violating observabales are less sensitive to the 2HDM, compared to their LFU non-violating counterparts

Continuing with the approach of fixing the parameters to their best fit values before performing the scan, one sees that the 2HDM-I contributions can reduce the current level of tension between experiment and predictions in a swathe of the $b \to s\ell\ell$ observables including, among others, binned angular observables in $B \to K^*\ell\ell$. A large section of the parameter space is again permitted within the 1σ region, and the 2HDM-I is able to outperform the SM. There arises an additional constraint on $\tan\beta$ in this scenario, with $\tan\beta \gtrsim 0.14$ at 2σ, which is compatible with the bound from the theoretical considerations in Sec. 4.2. The 2HDM-II case shown in Fig. 4.13 is rather dissimilar, as now an upper bound on the charged Higgs boson mass at the 1σ level is generated.

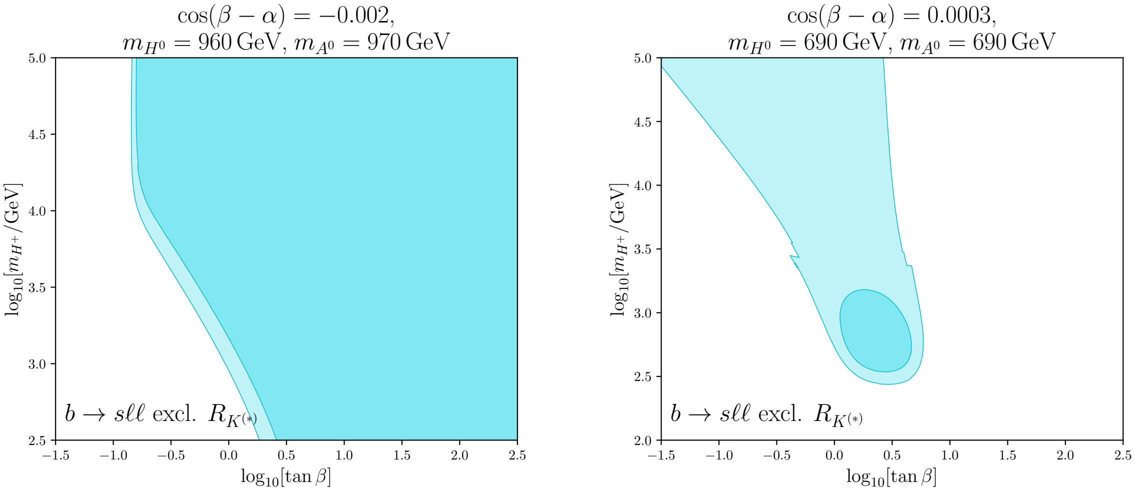

Figure 4.13: Contour plot of the allowed parameter space for the 2HDM-I (left) and 2HDM-II (right) in the $(\tan\beta - m_{H^\pm})$ plane for the leptonic $B_{d,s} \to \mu^+\mu^-$ decays and the semi-leptonic $b \to s\ell^+\ell^-$ observables excluding the $R_{K^{(*)}}$ observables. The lighter contour indicates the allowed parameter space at 2σ confidence level while the darker contour corresponds to 1σ.

4.4.4 Global Flavour Fits

At last, the observables are now in place to be combined into a global fit, including flavour observables, Higgs signal strengths, and the EWPOs. It is prudent to exclude the LFU ratios $R(D^{(*)})$, $R_{K^{(*)}}$ and take the limits of alignment and degenerate masses, as discussed above, while m_{12} has no impact in the flavour sector. Including the LFU ratios $R(D^{(*)})$, $R_{K^{(*)}}$ yields similar contours, however the quality of the best fit point is much reduced. The fits for all four types of 2HDM are shown in Fig. 4.14.

In the 2HDM-I, much of the low $\tan\beta$ region is found to be excluded, although a firm lower bound cannot be stated as there is a clear correlation with the masses of the new Higgses. Turning to the Higgs masses, in this scenario and parameter region only a bound at the 1σ level can be found; $m_{H^\pm} \leq 83.4$ TeV. The constraints on $\cos(\beta-\alpha)$ can be found by fixing the masses to the best fit values, where it is found that, at the 2σ level $|\cos(\beta-\alpha)| \leq 0.14$.

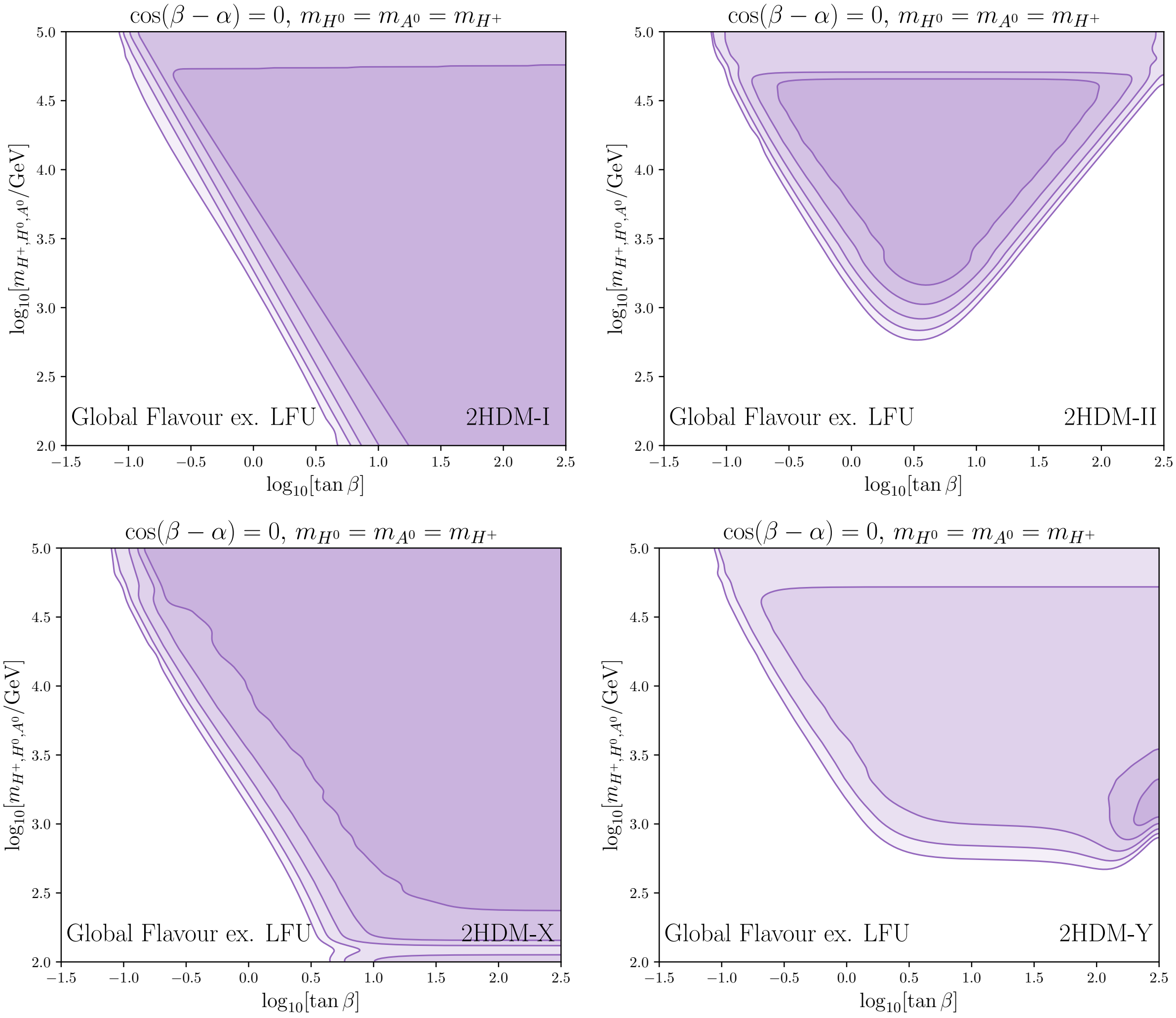

Figure 4.14: Combined fit of all flavour observables (excluding LFU), Higgs signal strengths, and EWPOs in the 2HDM (in the $\tan\beta - m_{H^\pm}$ plane), taken in the limits of alignment ($\cos(\beta-\alpha)=0$) and degenerate masses ($m_{H^0}=m_{A^0}=m_{H^\pm}$). Contours are shown representing allowed parameter space at 1, 2, 3, 4, 5σ confidence from darkest to lightest.

For the case of the 2HDM-II, the bounds on $\cos(\beta-\alpha)$ can be improved on compared to the Higgs signal strengths alone; $|\cos(\beta-\alpha)| \leq 0.04$ at the 2σ level. The best fit further favours values of $m_{H^\pm} \approx m_{H^0} \approx m_{A^0} \approx 2.3$ TeV and $\tan\beta \approx 4$. Upper bounds on the Higgs masses can also be found, at least up to the 2σ level, beyond which there are no limits found within the examined parameter region. Additionally, there is a lower bound of $m_{H^\pm} \geq 860$ GeV, with notable correlation between the Higgs masses and $\tan\beta$.

For the 2HDM-X, the constraints are distinctly similar to those of the 2HDM-I, leaving a large degree of freedom for the 2HDM parameters. In particular, the masses can stray as low as the electroweak scale, at which point the question of the validity of the WC expressions must be raised [201]. Again, there is a clear correlation between the masses and $\tan\beta$, but when $\tan\beta$ is large, the couplings to the quark sector become small and sensitivity is lost.

The 2HDM-Y is the most constrained of the types of 2HDM within the 2σ region, with a small allowed region in the parameter space that is examined here. Beyond this exclusion level, the mass constraints bear a resemblance to those of the 2HDM-II, with which it shares the quark sector couplings, which are key for the crucial $\mathcal{B}(\bar{B} \to X_s\gamma)$ channel.

4.5 Collider Constraints

Thus far the focus has been on indirect methods of constraining the possible parameter values of the 2HDM, but there have also been vast and numerous efforts to directly detect BSM states, after the fashion of previous particle discoveries. The main challenge is combining each of these individual searches in a consistent framework so that the huge array of search data can be leveraged together. Thankfully, this ground has already been trod, with the package HiggsBounds [326–332] developed to this end. The package 2HDecay [159, 333–337] is used in tandem with this to calculate the branching ratios and decay widths for each of the 2HDM bosons at some value of the 2HDM parameters. This data is then fed into HiggsBounds in a consistent fashion to check how the parameter point stacks up in the face of the search data. There are additional wrinkles to this analysis chain that warrant further consideration. In particular, the channel of charged Higgs boson production in association with $t\bar{b}$ has been key in searches for the 2HDM, and in this case MadGraph5_aMC@NLO [338] can be used to generate the cross section in this channel and then the result interfaced with HiggsBounds. Additional input includes the couplings of Higgs bosons, as shown in Tab. 4.2, with the degenerate mass and exact alignment limits taken, allowing use of $m_{12}^2 = m_{H^0}^2 \sin\beta\cos\beta$ (see Eq. (4.29)).

This approach can be pushed further, and the future performance of the HL-LHC can be examined in this context. With the considerable planned upgrades, it is expected that the integrated luminosity will reach $\mathcal{L}_{\text{HL-LHC}} = 3\ \text{ab}^{-1}$. This will clearly boost the discovery potential of the experiment, with the typical approach being to scale the cross section limits by a factor $\sqrt{(\mathcal{L}_0/\mathcal{L}_{\text{HL-LHC}})}$ for a search with a reference luminosity $\mathcal{L}_0$. Though there are limits to this assumption [339], it is the most practical approach when dealing with the wealth of data across many channels and searches used here.

The extrapolation is not this straightforward for a few reasons. First up, a number of the searches that can be used to constrain the 2HDM focus on the behaviour of h^0, seeking to make precision measurements of the relevant signal strengths. In these cases, the bounds are set to match the values expected of a SM Higgs, as this is, for phenomenological purposes, the nature of h^0 when in the exact alignment limit and with the mass set to 125 GeV as is the case here. This is addressed by using the work in Ref. [34] to match the SM predictions. Whilst the main directly quantifiable change in moving from the current state of LHC operations to the HL-LHC is the luminosity upgrade, some of the search data in HiggsBounds is from the first full run of the LHC, during which collisions were performed at a centre of mass energy of $\sqrt{s} = 7 - 8$ TeV, in contrast to the run 2 value of 13 TeV, while the HL-LHC will also operate at $\sqrt{s} = 13 - 14$ TeV. As such, the increased cross sections from the energy boost at the HL-LHC compared to the run 1 LHC data must be reflected in tandem with the improved limits from the luminosity gain (see also Ref. [182]). Again Ref. [34] is put to work for h^0 extrapolations, while for the BSM searches MadGraph5_aMC@NLO [338] is used to calculate the increase in the production cross sections as a function of the BSM Higgs mass and the search data limits are then scaled accordingly.

To perform the scan, 50000 points within the examined 2HDM parameter space are randomly generated and fed through the analytical apparatus. The resultant datasets are shown in Fig. 4.15, where orange points are allowed by current data but excluded by the extrapolated dataset while blue points are allowed by both. In the following, the main channels that give the exclusion in each region are outlined. First, note that the historic baseline sensitivity from the Large Electron–Positron Collider (LEP) [340] excludes charged Higgs boson masses below 72.5 GeV and 80 GeV for the Type I and Type II 2HDM models respectively.

For the 2HDM-I it is the leptonic decay of neutral Higgses, such as $H^0 \to \mu^+\mu^-$ as studied in Ref. [341], that exclude lower particle masses at low values of $\tan\beta$, with the sensitivity to $H^+ \to \tau^+\nu_\tau$ peaking at ~ 85 GeV [342]. Then, in terms of increasing mass, it is the decay

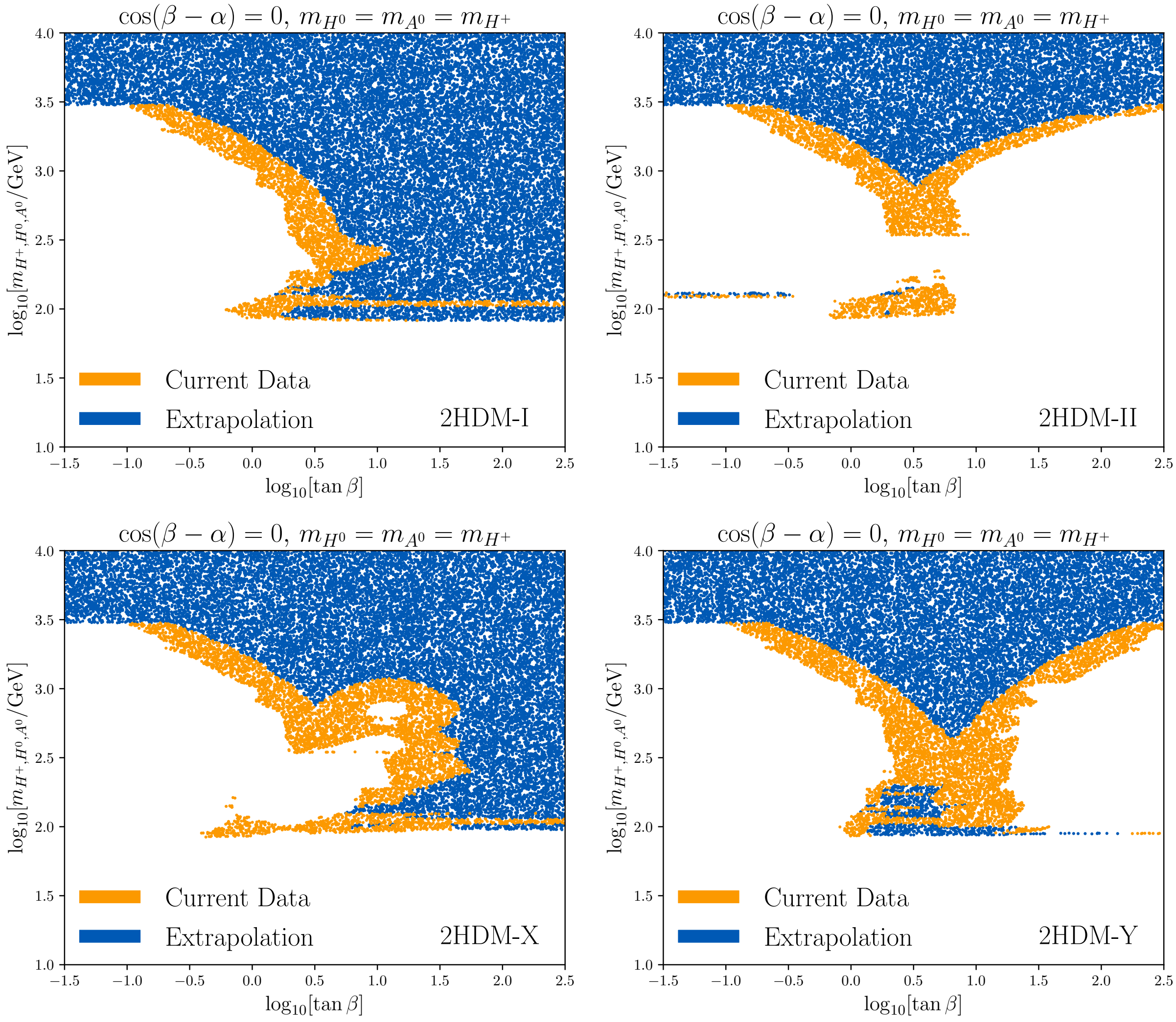

Figure 4.15: Scans of the 2HDM parameter space with randomly generated points shown in blue if allowed by the current and extrapolated bounds, and in orange if currently allowed but expected to be excluded by the HL-LHC.

$H^+ \to t\bar{b}$ [343] that excludes the new Higgs states from ~ 250 GeV until falling cross sections lead to a loss of sensitivity at ~ 2.5 TeV, beyond which point all sensitivity is lost. As $\tan\beta$ increases, the exclusion limit from this channel falls, as the H^+tb coupling is proportional to $\cot^2\beta$[3]. In the

---

[3] The relevant Yukawa coupling is $2((m_t\xi^u_{H^+})^2+(m_b\xi^d_{H^+})^2)/v^2$, where $\xi^{u,d}_{H^+}=\xi^{u,d}_A$ in Tab. 4.2.

moderate $\tan\beta$ region it is the $H^0/A^0 \to 4b$ [344] channel that gives the exclusion at low masses, with the kink at ~ 100 GeV due to $\mathcal{B}(H^+ \to \tau^+\nu_\tau)$ falling to zero as $\mathcal{B}(H^+ \to t\bar{b})$ rises to one here, with $\mathcal{B}(H^+ \to t\bar{b}) \approx 1$ once $m_{H^\pm} \gtrsim m_t$. Then, as a result of the heavy neutral Higgs bosons' couplings also falling with rising $\tan\beta$, the $H^0 \to \ell\ell$ channels become less notable. As mentioned above, there is a flat cut-off from $H^+ \to qq/\tau^+\nu_\tau$ [340]. As one would expect, extrapolating to the expected HL-LHC performance does lead to some improvement in the constraints, but in this case the effect is only notable for low and moderate $\tan\beta$, as the couplings to the new Higgs states are reduced in this region and beyond this the primary constraint is from the LEP, which is not subject to the extrapolation.

Moving to the 2HDM-II, the most significant channels at low $\tan\beta$ are $H^0 \to \gamma\gamma$ and $H^+ \to t\bar{b}$, which give similar levels of exclusion [343, 345, 346], with greater sensitivity in $H^+ \to t\bar{b}$ as the masses of the new Higgses increases, before the production cross sections reduce as the masses rise further. In the moderate $\tan\beta$ range, masses up to around 90 GeV are ruled out by $H^+ \to \tau^+\nu_\tau$. The exclusionary power of this channel then falls as the branching ratio decreases, with a general lack of sensitivity in the region of $\tan\beta$ of order 1 and masses of ~ 100 GeV, with this allowed region nearly, if not entirely, ruled out in the extrapolation to the HL-LHC. It is then the $H^0 \to \tau^+\tau^-$ channel that steps in to exclude masses beyond this region [347], and indeed up to high masses in the large $\tan\beta$ region, exceeding the limits from $H^+ \to t\bar{b}$. The extrapolation gives a notable improvement, except for the aforementioned small allowed region with masses of ≈ 95 GeV and $\tan\beta \approx 2$, beyond which the direct search limits are expected to be able to compete with those from the flavour sector.

Lower mass bounds on the new Higgs bosons are found at 82 GeV and 86 GeV in the Type I and II 2HDM respectively. Whilst these are less stringent than those found from the combined flavour observables fit in Sec. 4.4.4, they improve at low $\tan\beta$ in both models and also at high $\tan\beta$ in the 2HDM-II, owing to the dependence of the couplings of these models on $\tan\beta$, in line with what is seen in the flavour sector.

As for the case of the 2HDM-X, in the low $\tan\beta$ range, the neutral heavy Higgses decaying to b quarks dominate the exclusion up to the top quark mass threshold [344, 348], at which point it is the well studied $H^+ \to t\bar{b}$ channel that takes over as the primary exclusion channel. This continues until $m_{H^\pm}$ is too large for the charged Higgs boson to be produced with a significant cross section [343]. In the central $\tan\beta$ range, the LEP results and then the $H^+ \to \tau^+\bar{\nu_\tau}$ channel exclude masses below around 100 GeV [349]. Beyond this mass, the branching fractions fall for this channel to the point where it is no longer able to give exclusion regions, while $H^0 \to \tau^+\tau^-$ is responsible for the remaining exclusion in this region [347]. It would be reasonable to expect that these leptonic decays become ever more exclusionary with increasing $\tan\beta$ as the lepton couplings are proportional to $\tan\beta$. However, in this type of 2HDM, the quark couplings are much reduced at large $\tan\beta$, meaning that the new Higgs bosons can almost be considered as entirely decoupled from the quark sector, resulting in minimal production cross sections. This leaves the high $\tan\beta$ region almost unconstrained, save for the LEP bound [344]. The extrapolation to the HL-LHC combats this issue somewhat, with the most pronounced improvements in the moderate $\tan\beta$ region from these leptonic decays.

Finally, turning to the 2HDM-Y, the situation is similar to the outcomes of the 2HDM-II study, with the leptonic decays of H^0 excluding masses below the top mass at low $\tan\beta$ [341, 350], and then the $H^\pm \to t\bar{b}$ channel once again provides the primary exclusion above the top mass [343]. The relatively low branching ratios in the moderate $\tan\beta$ region leave little exclusion potential here, in the current data at least, but the extrapolation can address this to a significant extent, ruling out a swathe of this parameter space through improved limits from $H^+ \to t\bar{b}$ and $H^0 \to b\bar{b}$. At high $\tan\beta$, $H^0 \to b\bar{b}$ gives the exclusion up to ~ 250 GeV [351], beyond which $H^+ \to t\bar{b}$ is once again the most sensitive channel.

4.5.1 Comparison with Flavour Constraints

To make the comparison between the flavour sector and the direct collider constraints more concrete, the two can be overlaid, using the same axes as in Fig. 4.15. It is worth stressing that this does not comprise a statistical combination of the results as HiggsBounds is not used here to give a combined level of exclusion from all the data, but to assess if each point is excluded by one search in particular.

For the 2HDM-I the LEP data is able to outperform the flavour sector when $\tan\beta$ is large, as the flavour sector lacks sensitivity in this region. The complementary nature of these two approaches is also evident in that the flavour bounds are more restrictive for low $\tan\beta$ regions, a result which holds across all four types of 2HDM. In the extrapolation to the expected HL-LHC data, the collider constraints can become competitive with the flavour sector in setting a minimum mass bound. For the 2HDM-X, the collider searches, particularly the $H^0 \to \tau^+\tau^-$ channel in the HL-LHC extrapolation, are more sensitive than the flavour sector and can rule out a portion of the 1σ region from the flavour observables, though both approaches lack sensitivity above

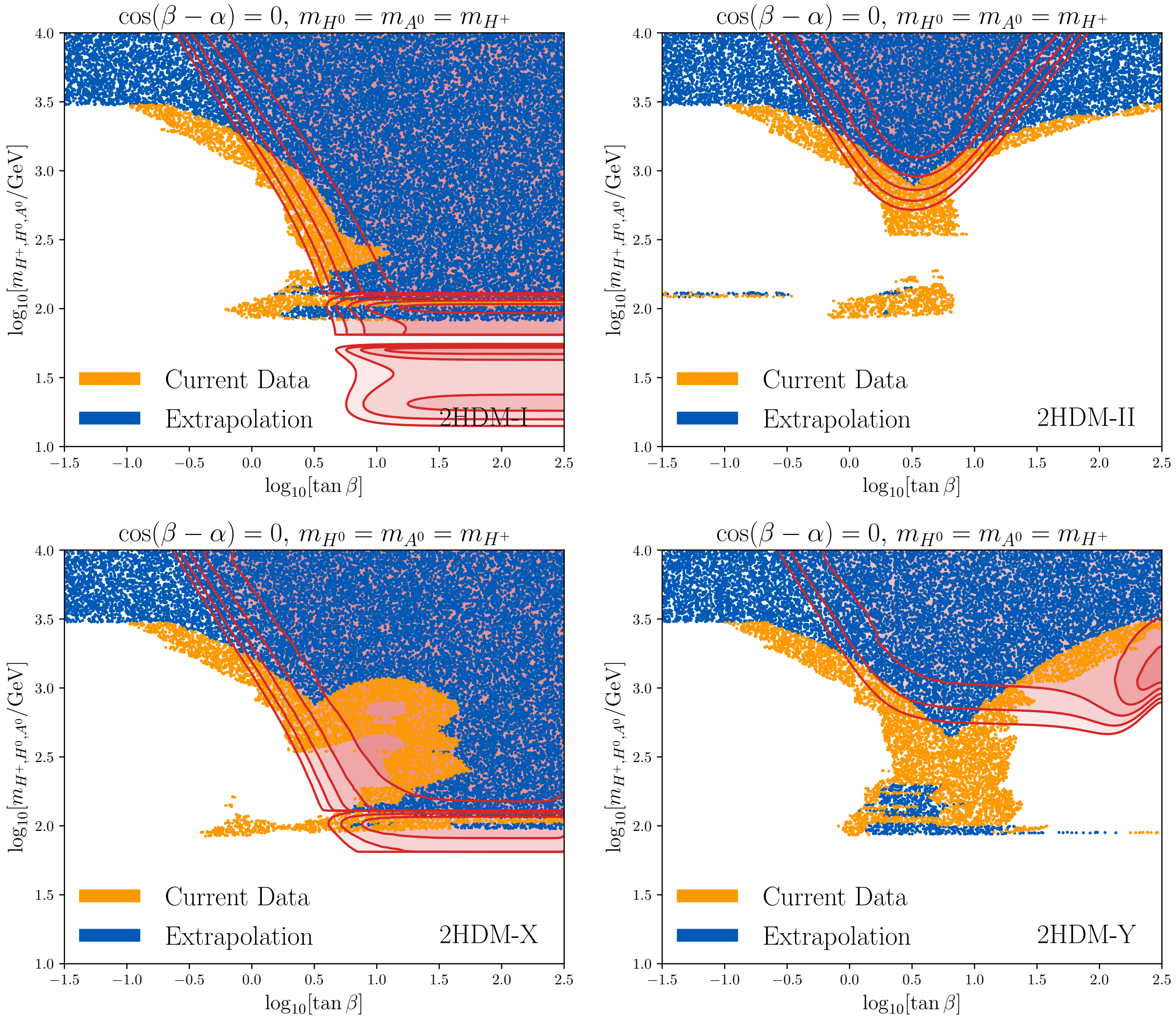

Figure 4.16: Scans of the 2HDM parameter space with randomly generated points shown in blue if allowed by the current and extrapolated bounds, and in orange if currently allowed but expected to be excluded by the HL-LHC and contours from the flavour sector at 1, 2, 3, 4, 5σ confidence, from darkest to lightest.

masses of 100 GeV when $\tan\beta$ is large. Moving to the 2HDM-Y case, the comparison between the two sectors is particularly telling, with current collider data excluding all of the 1σ region from the flavour constraints, and the majority of the 2σ region, which the extrapolation very nearly entirely excludes. These results demonstrate the high degree of complementarity between the datasets and indicate where future searches should focus their efforts for 2HDM studies.

4.6 Electroweak Phase Transition

As outlined in Sec. 2.6.1, one of the conditions for the observed baryon asymmetry of the Universe is a SFOEWPT, which is not possible with the measured value of the Higgs mass and thus requires some NP. This is well trod ground in the realm of the 2HDM, with a focus on the 2HDM-II in Refs. [181, 184, 352], finding a SFOEWPT possible for Higgs masses below a TeV, with indications that a mass split between the new Higgs bosons is more favourable to the prospects of a SFOEWPT, though this is immediately in some degree of tension with the theoretical considerations of Sec. 4.2. Some of the other works that explore the SFOEWPT in the context of the 2HDM include Refs. [179, 180, 183, 185–187, 353, 354]

Here, the package BSMPT [355, 356] is deployed to this end, which calculates the strength of the EWPT at a given point in parameter space and has detailed documentation available[4]. This package takes input in terms of the lambda basis, rather than the mass basis that has been focussed on thus far here. For the most part, the conversion between the two is already established; see Eqs. (4.11)-(4.15), but m_{12}^2 is also required in this basis. This hurdle can be overcome by turning to vacuum stability, which, in the alignment limit, confers the sufficient but not necessary condition of [200]

$$m_{12}^2 = m_{H^0}^2 \sin\beta\cos\beta \cap m_{h^0}^2 + m_{H^\pm}^2 - m_{H^0}^2 > 0 \cap m_{h^0}^2 + m_{A^0}^2 - m_{H^0}^2 > 0. \tag{4.29}$$

Whilst this is only valid when $\cos(\beta-\alpha)$ is small and $m_{H^0} \lesssim m_{A^0}, m_{H^\pm}$, these conditions are in line with the mass degeneracy and alignment limits that have been adopted thus far. The strength of the EWPT is determined by

$$\xi_c = \frac{\omega_c}{T_c}, \tag{4.30}$$

where ω_c is the high-temperature VEV ($\omega_c^2 = \omega_1^2(T_c) + \omega_2^2(T_c)$ and $\omega_i(T=0) = v_i$) at the critical temperature T_c. A SFOEWPT is defined as having $\xi_c > 1$, and it is only when this is the case that BSMPT returns a positive result.

Across the four types of 2HDM, the differing Yukawa structures have minimal impact on the strength of the EWPT for points with the same parameters, and so the main consideration is how compatible a SFOEWPT is with the results of the global parameter constraints in each of these models. Some results are shown for the 2HDM-II in Tab. 4.3. In general, the SFOEWPT is

---

[4] https://phbasler.github.io/BSMPT/

$\tan\beta$	Mass Basis (GeV)			Lambda Basis			m_{12}^2	ω_c	T_c	ξ_c
	$m_{H^\pm}$	m_{H^0}	m_{A^0}	λ_3	λ_4	λ_5	(GeV^2)	(GeV)	(GeV)	
4.2	50000	50000	50000	0.26	0	0	5.6×10^8	0.66	162	0.004
4.2	2320	2320	2320	0.26	0	0	1.2×10^6	23	162	0.14
4.2	2320	2250	2280	10.8	-8.3	-2.2	1.1×10^6	31	186	0.17
1.0	2320	2320	2320	0.26	0	0	2.7×10^6	23	162	0.14
10	2320	2320	2320	0.26	0	0	5.3×10^5	24	162	0.15
4.2	860	710	860	8.03	-3.9	-3.9	1.1×10^5	142	175	0.81
4.2	860	690	860	8.95	-4.3	-4.3	1.1×10^5	177	176	1.00
4.2	680	470	680	8.22	-4.0	-4.0	5.0×10^4	211	149	1.42
4.2	570	320	570	7.60	-3.7	-3.7	2.3×10^4	226	126	1.79
4.2	490	250	490	6.12	-2.9	-2.9	1.4×10^4	207	126	1.64
4.2	490	490	490	0.26	0	0	5.4×10^4	24	161	0.15

Table 4.3: Table of results for the EWPT in the 2HDM-II in the alignment limit, employing the condition of Eq. (4.29). In this limit, as follows from Eqs. (4.11)-(4.15), one finds: $\lambda_1 = \lambda_2 = m_{h^0}^2/v^2 = 0.26$, i.e. $\lambda_{1,2}$ are fixed and independent of the Higgs masses and $\tan\beta$ (and therefore not shown in the table). In addition, one finds that $\lambda_{3,4,5}$ are independent of $\tan\beta$, and $\lambda_3 + \lambda_4 + \lambda_5 = m_{h^0}^2/v^2 = 0.26$.

possible when the masses of the new Higgs bosons are below around 850 GeV, with an additional requirement of a significant mass split between the charged and heavy neutral scalar bosons, while the pseudoscalar can have a mass similar to the charged boson. Returning to the results from the theoretical constraints of Sec. 4.2, this poses a challenge for the 2HDM, as the new Higgs boson masses must become increasingly degenerate with increasing mass, and only masses below the TeV scale will retain sufficient freedom to manifest the required mass split.

In the 2HDM-I, such points as permit the SFOEWPT are allowed within a 1σ deviation from the best fit point found in Sec. 4.4.4, which are also allowed by the direct search data collated in Sec. 4.5. This is the same result found in the 2HDM-X, which is perhaps unsurprising given the prima facie similarity of the fit constraints.

For the 2HDM-II, one must stray to a 2σ deviation from the best fit point to attain points capable of generating a SFOEWPT, which pushes the Higgs masses to values significantly below those favoured by the global fit. The 2HDM-Y is the most constrained of the four models in the global fit, particularly for the lower σ regions. This poses problems for the SFOEWPT, which exhibits a preference for moderate $\tan\beta$, in conflict with the 1 and 2σ regions permitted in this model, and so the 2HDM-Y cannot accommodate a SFOEWPT within the 2σ region. Beyond this, the allowed regions expand considerably, and thus the SFOEWPT is possible at and above 3σ from the best fit.

4.7 Anomalous Magnetic Moment of the Muon

The anomalous magnetic moment of the muon, a brief introduction to which can be found in Sec. 2.6.3, has been a rich area of study in the context of BSM models, and the 2HDM is no exception in this regard [357, 358], especially in the wake of the Fermilab measurement that confirmed a previous Brookhaven measurement and the headline 4.2σ discrepancy from the SM [77]. It is worth highlighting again here that this discrepancy makes use of the Theory Initiative's White Paper (WP), while a lattice QCD from the Budapest–Marseille–Wuppertal (BMW) collaboration finds only a 1.6σ deviation between their SM prediction and the experimental results, so it is a worthwhile endeavour to consider both theoretical predictions here.

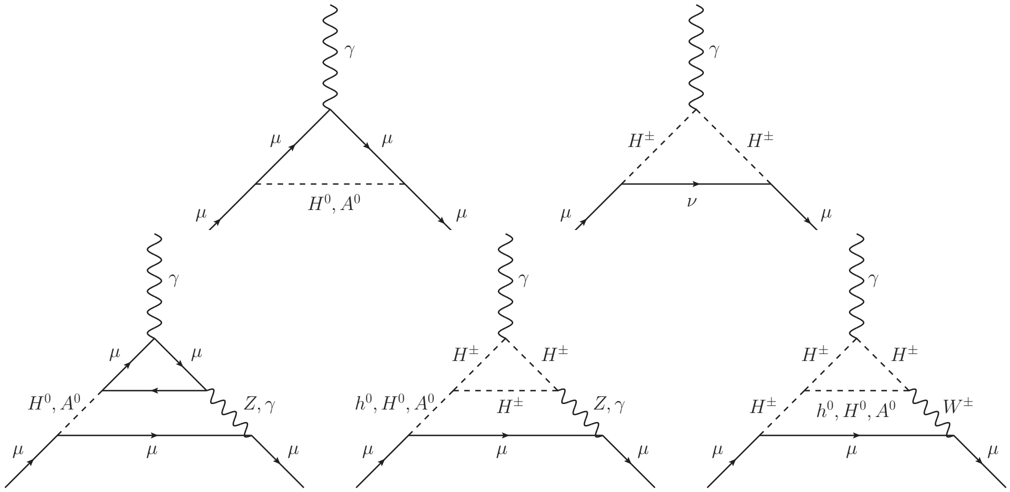

Figure 4.17: Examples of one- and two-loop 2HDM contributions to $(g-2)_\mu$.

In the 2HDM, using FLAVIO's WET-3 basis [195], the contribution to a_μ is defined as

$$a_\mu^{\text{2HDM}} = \frac{G_F m_\mu^2}{\sqrt{2}\,\pi^2} C_7, \tag{4.31}$$

where the contributions at one- and two-loop level are given in Ref. [267]. The two-loop contributions come from the Barr-Zee diagrams [359], which are depicted in Fig. 4.17. All the Higgs bosons of the 2HDM are present in these loops, so all the 2HDM parameters enter into the expressions for the contributions to a_μ, and so the standard alignment and mass degeneracy limits are once again adopted.

To accommodate a_μ in the 2HDM-I, one must venture to regions forbidden by all other constraints, with a strong preference for $m_{H^\pm} \sim 100\,\text{MeV}$ and $\tan\beta \sim 0.5$, at which point the 2HDM-I is capable of replicating almost exactly the experimental result, irrespective of which of the SM predictions is taken. In the physical region, shown in Fig. 4.18, the 2HDM-I is unable to improve over the SM values.

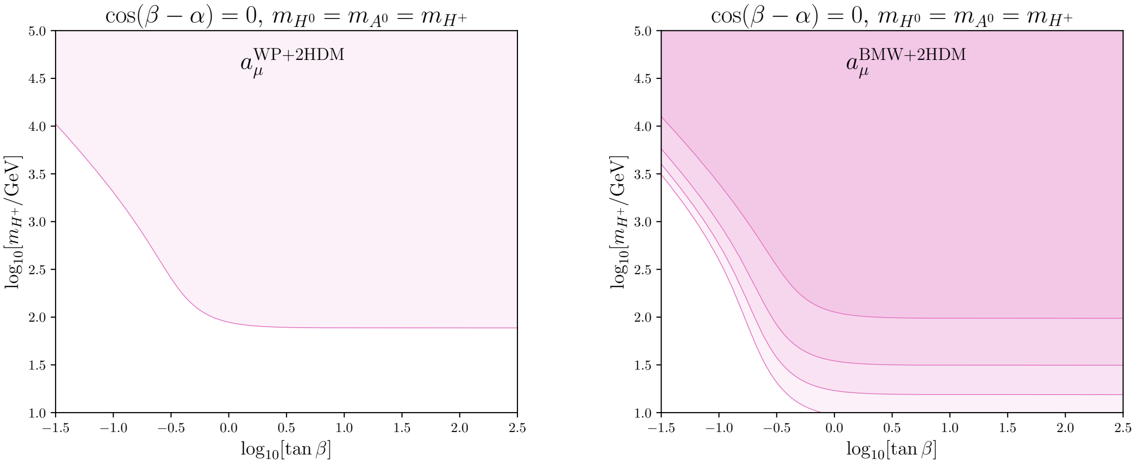

Figure 4.18: Contour plot of allowed 2HDM-I parameter space in the $(\tan\beta - m_{H^\pm})$ plane for a_μ, taken in the alignment and degenerate mass limits. In the left plot, the SM prediction taken from the theory initiative is used; in the right, from the BMW collaboration. Contours are plotted representing allowed parameter space at 1, 2, 3, 4, 5σ confidence from darkest to lightest: in the left plot, only the 5σ contour is exists; in the right, the $2, 3, 4, 5\sigma$ contours.

The results for the 2HDM-II are shown in Fig. 4.19, where it is worth noting that the $\tan\beta$ range shown is substantially larger than for the other plots shown, as a result of being unable to accommodate a_μ within 2σ in the usual parameter space when using the WP SM value. This is beyond the perturbative region and so the anomaly cannot be consistently explained by the

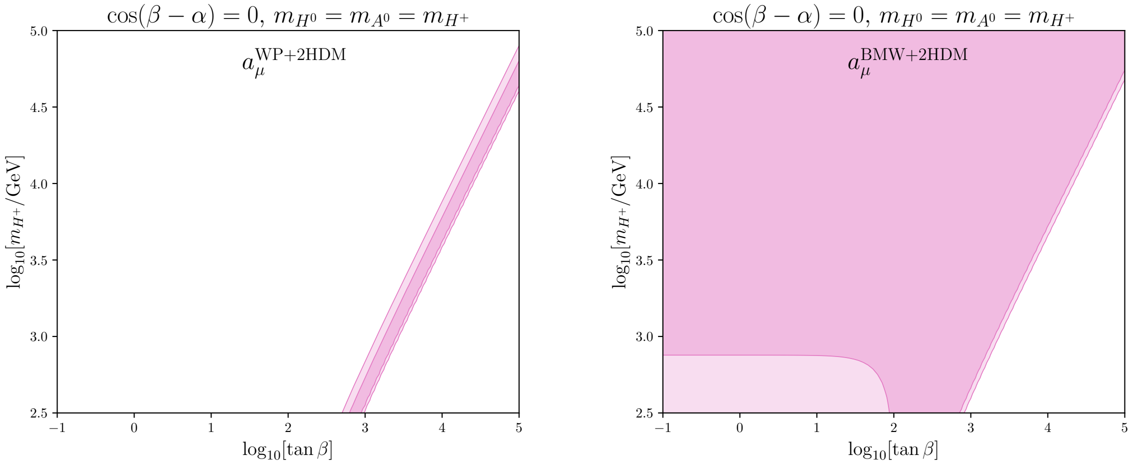

Figure 4.19: Contour plots of the allowed 2HDM-II parameter space in the $(\tan\beta - m_{H^\pm})$ plane for a_μ, using the Standard Model prediction by WP20 [77] (BMW [98]) (left (right) plot), fixing the additional parameters as $\cos(\beta-\alpha)=0$, $m_{H^0}=m_{A^0}=m_{H^\pm}$. The lighter contour indicates the allowed parameter space at 2σ confidence level while the darker contour corresponds to 1σ.

2HDM-II. Alternatively, with the BMW prediction, the 2HDM corrections need not be as large as this SM prediction lies closer to the experimental measurements, and so a larger swathe of the parameter space is allowed.

In order to fully resolve the tension in this observable then, one must consider either values of $\tan\beta$ corresponding to non-perturbative Yukawa couplings or restrict the masses of the new Higgses to < 1 TeV, thereby permitting a mass splitting for the new Higgses; see Sec. 4.2. The case for the 2HDM-X is similar to that of 2HDM-I, with more scope for lower masses from the global fit of Sec. 4.4.4, and therefore significant regions where a_μ can be consistently explained within 2σ of the best fit point. In contrast, the 2HDM-Y more closely reflects the case in the 2HDM-II, whereby it is not possible to resolve the tension within the 2σ allowed region from the other constraints considered.

As an additional note to this section, it is worth pointing out that much more is still ongoing in determining an accurate SM prediction for the anomalous magnetic moment of the muon. Recent improvements to lattice QCD precision levels [98, 360, 361] indicate a closer agreement to the experimental values than the WP prediction, so the required contributions from the 2HDM may be smaller, which favours higher masses of the new Higgs bosons.

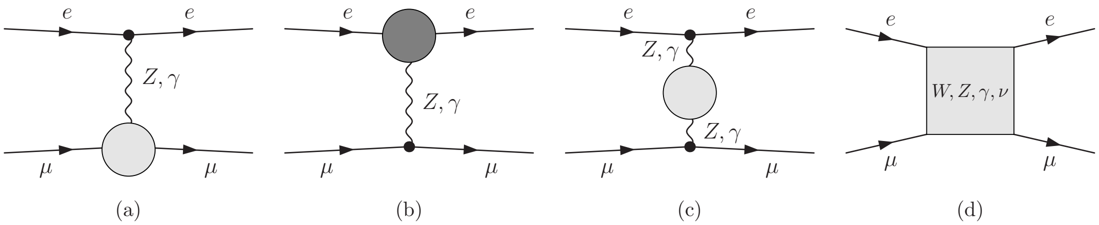

Figure 4.20: Feynman diagram topologies contributing to $e - \mu$ scattering at one loop level. Highlighted are renormalised vertex and propagator corrections for the topologies (a)-(c). They include 2HDM Higgs contributions for the propagator and μ vertex corrections. The different shading of (b) indicates that electron mass contributions to the virtual amplitude have been neglected. The propagator contributions include leading order hadron polarisation effects consistently.

4.8 The 2HDM at MUonE

Following on from the anomalous magnetic moment of the muon and the debate in the literature about the SM prediction, one of the more pertinent sources of uncertainty is the hadronic polarisation contribution to $\Delta a_\mu^{\text{had}}$, wherein lies the significant deviation between some lattice QCD predictions [98, 360, 361] and analyticity driven techniques based on the R ratio [83], which rely on Ref. [362] and Refs. [82, 84–87] respectively. The links of a_μ^{had} to the electroweak fit are also of general interest and have been studied in Refs. [363–366].

To help reduce the uncertainty surrounding this parameter, the MUonE experiment [367, 368] has been proposed, with the stated goal of bringing the statistical uncertainty down to around 0.3%. This will be done through a precision measurement of muon-electron scattering, by use of a 150 GeV muon beam scattered off atomic electrons, which is projected to generate $\sim 3.7 \times 10^{12}$ events from a leading order cross section of around 250 μb. The comparatively low centre of mass energy in this scattering process implies a small t channel momentum exchange compared to the Z boson threshold, thereby enabling the direct measurement of $\Delta a_\mu^{\text{had}}$ [83, 369]. Efforts are also very much underway to improve the theoretical uncertainty of the SM prediction of the scattering [370–375] to meet the experimental precision. There are consequences to this expected precision improvement for BSM models as well [376–379]. In contrast to the large QCD background in the LHC, the MUonE experiment may provide a clearer window into modifications to new electroweak states, but here the focus is on the 2HDM and the role this may play in the MUonE environment. It is therefore worthwhile to explore how the 2HDM may manifest in the scattering process and the resulting measurement of the hadronic vacuum polarisation.

The Born level electron-muon scattering is understood in the framework of the SM, and moving to the one-loop level the amplitude is given by

$$|\mathcal{M}|_1^2 = |\mathcal{M}_{\text{Born}}|^2 + 2\text{Re}\left\{\mathcal{M}_{\text{Born}}\mathcal{M}^*_{\text{virt}}\right\}, \tag{4.32}$$

where the virtual part is depicted in the Feynman diagrams of Fig. 4.20. The electron mass contributions can be safely discarded in the analysis of the virtual amplitude as the 2HDM types examined here are consistent across leptons and $m_e \ll m_\mu$. The consequence of this is that the t-channel Higgs and Goldstone diagrams, along with the scalar contributions in the box diagrams of Fig. 4.20(d), are removed. The on-shell renormalisation scheme is deployed throughout this section. The t-channel photon contributions give a soft singularity at tree level; this is avoided in the experimental design by the requirement of a finite recoil energy. In contrast, the inclusion of virtual massless propogators connecting the on-shell legs yields additional soft eikonal singularities in $|\mathcal{M}|_1^2$, which then cancel against real photon emission via the Kinoshita-Lee-Nauenberg theorem [380, 381]. In Abelian gauge theories, the form of the eikonal approximation is particularly compact and well documented in the literature [382, 383], along with being implemented in FormCalc [159]. For completeness, the real emission part is considered as well, including unresolved soft photon radiation up to 10% of the MUonE centre-of-mass energy, even though this part is not sensitive to the 2HDM modifications.

Turning again to the well established toolchain of FeynArts, FormCalc and LoopTools [159, 160, 163], numerical expressions of the loop diagrams can be calculated, where the cancellation of the ultraviolet divergences is checked both numerically and analytically. The results are additionally validated by checking for independence from the virtual photon mass that is introduced to regularise soft singularities at intermediate steps. The performance in the 2HDM is also checked, by use of a comparison of the decoupling scenario against the SM results and the established cross section of $\sim 240\ \mu$b.

Assuming monochromatic muon beams and electron targets, the muon-electron scattering is determined entirely by the t channel momentum transfer as a $2 \to 2$ scattering process. This momentum transfer determines the scattering angles and the recoil energies of the colliding particles. In this analysis, a χ^2 test is used on the parameter of the scattering angle distribution with 51 independent bins, with the χ^2 value given by

$$\chi^2 = \sum_i \frac{(N_i - N_i^{\text{SM}})^2}{\sigma^2_{i,\text{syst}} + \sigma^2_{i,\text{stat}}}, \tag{4.33}$$

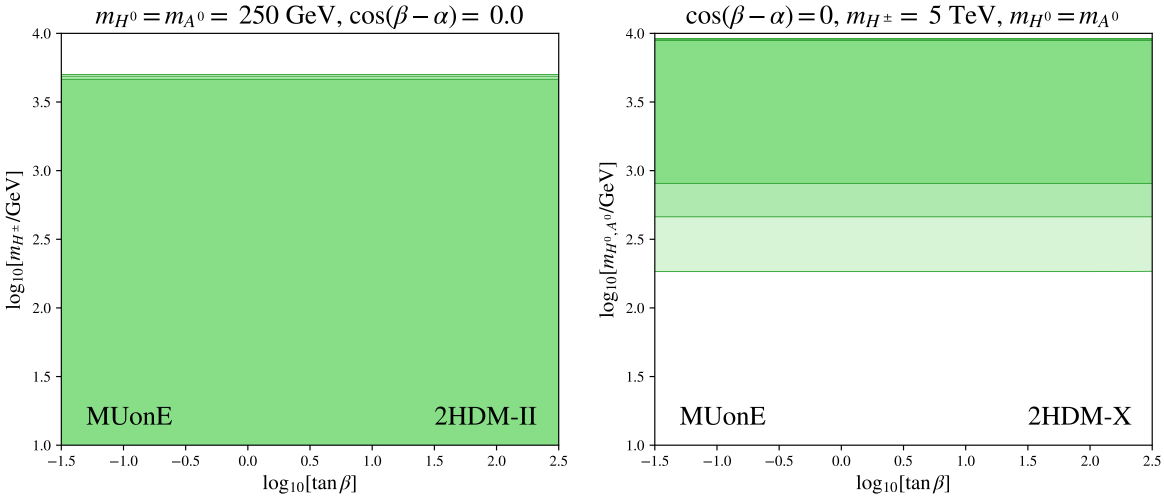

Figure 4.21: Contour plots of the allowed regions at 1, 2, 3σ from the MUonE analysis, where in this case the masses have been studied in differing mass scenarios.

where i runs over the bins, N_i are the 2HDM events in the i^{th} bin, N_i^{SM} denotes the SM expectation (evaluated at next-to-leading order), and $\sigma_{i,\text{stat}}$, $\sigma_{i,\text{syst}}$ denote the statistical and systematic uncertainties respectively. For the latter parameters, the typical benchmark values for the MUonE experiment are used here; $\sigma_{i,\text{stat}} = \sqrt{N_i}$ and $\sigma_{i,\text{syst}} = 10^{-5} N_i$ [368, 376]. The χ^2 value from a given point in the 2HDM parameter space can then be used to determine the sensitivity of the MUonE experiment to the possible existence of such a point, and conclusions drawn as to the regions of parameter space the experiment will be able to probe.

Much as in some of the other sections of this chapter, here the degenerate mass and alignment limits are examined but, in addition, a wide range of mass scenarios are studied, putting the theoretical constraints of Sec. 4.2 aside for a moment. Whilst the Higgs mass and $\tan\beta$ parameter space is scanned, the mass scenarios include independently varying the masses of the new Higgs, or fixing two of the masses to some values and scanning across the other, with $\cos(\beta-\alpha)$ also varied across scenarios.

In short, the results show that the MUonE is largely insensitive to the existence of the 2HDM, irrespective of type, with the maximal χ^2 in the majority of scenarios falling well below the threshold value corresponding to the 68% confidence level. As such, very few regions of the parameter space can be probed with any level of significance at the MUonE experiment. All is not lost from the 2HDM standpoint though, as some useful information can still be attained, although this does require the adoption of some extreme mass scenarios and it is worth reiterating that large mass splits between the new Higgses are ruled out by the theoretical constraints of Sec. 4.2. Two such scenarios are shown in the 2HDM-II and 2HDM-X in Fig. 4.21, where various of the new Higgs masses have been fixed and the remainder varied over the parameter space. In the 2HDM-II scenario shown, there is a 2σ $\tan\beta$ independent upper bound on the mass of the charged Higgs boson at ~ 4 TeV. In the other scenario shown, the 2HDM-X there is a $\tan\beta$ independent lower limit on the mass of the neutral scalars of $m_{H^0} = m_{A^0} \gtrsim 460$ GeV at 2σ, with an upper bound at around 8.5 TeV.

Enforcing a large mass split between the charged and neutral Higgses results in the greatest overall sensitivity, but large mass splits are certainly excluded by the theoretical considerations. There is also some exclusion at and beyond the TeV scale for $m_{H^\pm} = m_{H^0}$ when m_{A^0} is fixed to a value below 1 TeV. At the other end of the scale, the lower Higgs masses, below the order of 1 GeV do yield significant and notable contributions to the MUonE experiment and can be ruled out through this avenue, although it is worth pointing out that such low mass states would have been already observed in the direct collider searches as discussed in Sec. 4.5, so no additional exclusionary power is gained in this regime. In a similar vein, going to non-perturbative regions in $\tan\beta$ yields exclusion regions in the MUonE analysis.

Across the types of 2HDM, the contours found are very similar in the majority of the parameter space examined. This is because the dominant contributions to the scattering process come from the top quark loops, and each type of 2HDM has the same couplings to the top quark; see Tab. 4.2. Only in the extremal $\tan\beta$ regions is there some notable discrepancy between the differing types, where the lepton couplings become significant. As a result, in these regions, Types I and Y yield the same constraints, as do Types II and X, as these models have the same lepton couplings. In all scenarios and models, increasing $\cos(\beta-\alpha)$ does increase the sensitivity, but this effect is relatively minor and insufficient to give any meaningful additional exclusion regions.

As a consequence of these results, it is evident that the MUonE experiment does not give additional sensitivity to the 2HDM in parameter regions that are not already covered by the data examined in other sectors. Whilst this could be taken as disheartening in the context of this chapter, it is a boon to the experiment itself, which aims to accurately measure the leading-order hadronic contribution to the anomalous magnetic moment of the muon. These results indicate that this planned measurement will be free of troublesome contamination from any type of extant 2HDM that is consistent with the theoretical, flavour and collider bounds, in line with what might naively be expected from the small couplings of the Higgs bosons to the electrons.

4.9 Conclusions

Searches for BSM states are a huge part of the modern quest to further understand the nature of the Universe. As of yet, no concrete, definitive signals have been detected at the LHC, though there are a litany of anomalies and indicators that there may be some new states that yet remain hidden in the data. The 2HDM is one possible such set of states, introducing a total of five Higgs bosons, one of which is taken to be the observed SM-like Higgs state and here this model has been studied in depth, leveraging the power of a wide range of observables, in addition to the theoretical constraints that govern the model. This has spanned electroweak precision data, Higgs signal strengths, flavour observables and exotic searches, together comprising a comprehensive interrogation of the model. Again, there are no direct signs of the 2HDM, but this data can be used to set constraints on the parameter space of the model.

The 2HDM-I is able to statistically outperform the SM in the global fit, although the parameter space is found to be less constrained than the 2HDM-II, but bounds on the masses of the new Higgses can still be found; see Sec. 4.4.4. Extrapolating the LHC data to the future expected performance of the HL-LHC underlines the improvement in bounds that can be achieved with additional data, and how the collider search data can act in tandem with the other constraints. While some complementarity between flavour, Higgs physics and direct exotics searches remains, the finite energy coverage of exotics searches typically means a loss of direct LHC sensitivity for large masses approaching the decoupling limit, whilst the HL-LHC data may yet be competitive with the indirect flavour sector results. In all cases, the alignment limit is preferred, reflecting the closeness with which the observed Higgs lines up with the expected phenomenology of the SM Higgs.

The theoretical considerations, which act independently of the type of 2HDM, enforce a degree of degeneracy in the masses of the new Higgses, which becomes stricter as the masses scale higher. Examination of the SFOEWPT, one of the Sakharov criteria required to generate the baryon asymmetry of the Universe, also yields results that are largely type independent, at least in terms of the 2HDM parameters that are able to give the SFOEWPT. The difference in this area comes from the fact that there are different mass constraints, and only the 2HDM-Y cannot generate a SFOEWPT within a 2σ deviation from the best fit point.

Some tensions remain however, most notably in the LFU ratios $R(D^{(*)})$ and the anomalous magnetic moment of the muon, which the 2HDM cannot consistently resolve in the physically relevant parameter space, though there is some debate over the SM predictions for the latter that may result in the 2HDM being able to accommodate this observable. In contrast, the upcoming MUonE experiment lacks the power to probe the 2HDM in the parameter region examined, which is a good sign for the experimental aim of accurately measuring the hadronic vacuum polarisation contribution through the muon-electron scattering process. Consequently, MUonE data can be fully interpreted as a measurement of the hadronic vacuum polarisation contribution in these scenarios without the need to correct for BSM effects.

The recent measurements of the W boson mass [384] indicate a discrepancy of up to 7σ with the SM [213], and this has given rise to a great deal of study of the possible NP contributions, with the 2HDM a prime candidate amongst them [385–395]. In Ref. [7], this avenue was explored, and it was found that all four types of 2HDM studied here are capable of generating the shift required within the physically relevant parameter space. That said, it is worth noting that this experimental result has come under some scrutiny and is not necessarily as widely accepted as the other observables presented here.

Taken as a whole, this chapter provides a detailed and thorough exploration of the 2HDM, across a wide range of sectors. The combined constraints found on the parameter space are therefore the most complete and up to date that I am aware of, and additionally include the possible future constraints at the HL-LHC.

Chapter 5

Constraining Effective Top Quark Interactions using Graph Neural Networks

Whilst the previous chapter explores one specific BSM model in detail, there are no concrete signs of the 2HDM, nor indeed of any of the litany of BSM models lurking in the literature. To study a single chosen model in detail requires a large amount of time and resources, which the previous chapter is evidence of, and yet this may be in vain if nature manifests another model or one not yet thought of. It may make more sense then to take a more generalist approach, with the goal of constraining the potential phenomenology of all BSM models in a consistent framework.

This is where EFTs come into play. Introduced briefly in Sec. 2.7, EFTs provide a model agnostic approach to BSM physics by integrating out the interaction effects of BSM particles, which can safely be taken to have energy scales Λ beyond the electroweak scale. This systematic approach yields a collection of operators $\mathcal{O}_i$, each with a corresponding WC C_i, for a Lagrangian, in the SMEFT, of [109–114]

$$\mathcal{L} = \mathcal{L}_{\mathrm{SM}} + \sum_i \frac{C_i}{\Lambda^2} \mathcal{O}_i \,. \tag{5.1}$$

This handy framework has been studied a great deal in the literature, owing to its generality and applicability to a vast range of phenomena, such as Higgs physics [396–401], electroweak precision observables [221, 402, 403], and the top sector, which are particularly attractive due to the good control of statistical and systematic uncertainties at colliders.

However, the EFT formalism is not quite the silver bullet for BSM analyses. A single channel can have contributions from a large number of effective interactions, which can severely limit the potential sensitivity for an analysis of an individual operator, owing to the complicated and rich phenomenology at play. In addition, systematic uncertainties can limit the constraining power of this approach, possibly pushing the limits on the operators to non-perturbative regions when understood as ultraviolet constraints in concrete matching calculations.

In the face of the current state of affairs at collider experiments, there are two standard approaches to constraining EFTs. The most straightforward and historically well trodden path is to improve the various uncertainties present in the analysis, from both a theoretical and experimental standpoint. With improved data available, and assuming that the ongoing pattern of agreement with the SM continues, the limits on EFTs can be expected to improve. Further, with future collider searches raising the floor for detection of NP states through their increased centre of mass energy, the lower limit on Λ will rise concurrently, though this is not scheduled for great change in the coming years of the LHC programme.

Alternatively, one can aim to improve the constraints available with the current data by more comprehensive information extraction. It is here that machine learning is often deployed in modern high energy physics [404–411]. The traditional approach to collider physics is to make a series of rectangular selection cuts on an array of suitable collider observables, such as transverse momentum and pseudorapidity (see Sec. 2.5), but this may not capture the full delicate intricacy of the particle dance. As such, there may be some constraining power that evades these methods, and machine learning may be able to address this by condensing the multidimensional phase space information available in the data.

The second of these avenues is the focus of this chapter, which will also provide a useful prelude to the machine learning concepts explored in more depth in the following chapter. For the EFT, the top sector, which is particularly insightful for analyses of this kind [412–419] is chosen. Specifically, the relatively clean channel of $pp \to t\bar{t}$ production with semi-leptonic top decays is selected as it has good statistical control, thereby allowing for a robust exploration of the possibilities of the power of machine learning in an EFT context, similar to the work performed in Ref. [408]. To make best use of the expected correlations between the fully showered and hadronised objects, Graph Neural Networks (GNNs) with edge convolution [420–423] are the tool of choice, as they allow for exploitation not only of the structure of the full data but also of the relations between the intermediary and final state particles. This is particularly useful in the arena of particle physics applications, where it is often the case that decay chains are studied [2, 424–432]. Efficient event classification with GNNs, splitting the events into either SM or SMEFT operators could lead to improvements on the bounds of WCs after imposing cuts on the output score of the network.

This chapter is organised as follows. The relevant EFT formalism is outlined in Sec. 5.1, with an explanation of the baseline search used as a template, with the GNN approach detailed in Sec. 5.2, before it is brought to bear on improving the constraints on the WCs in Sec. 5.3. Conclusions are given in Sec. 5.4.

5.1 Effective Interactions for Top Quark Pair Production with Leptonic Decays

The differential cross section from the formalism of Eq. (5.1) can be written as

$$\mathrm{d}\sigma = \mathrm{d}\sigma_{\mathrm{SM}} + \frac{C_i}{\Lambda^2}\mathrm{d}\sigma_i^{(1)} + \frac{C_iC_j}{\Lambda^4}\mathrm{d}\sigma_{ij}^{(2)}. \tag{5.2}$$

The first term is the purely SM contributions, the second the interference of the EFT and SM terms and the third the EFT cross terms. The latter is suppressed by a factor Λ^4 and these terms can be put aside, bearing in mind that Λ can safely taken to be beyond the electroweak scale. Thus the cross section formula is truncated at order Λ^{-2}. This is a theoretically consistent approach, though it should be noted that the Λ^{-4} terms give dramatic momentum transfers and so will generally be easier to constrain when looking at collider data, even with the traditional rectangular cut approach. As such, this investigation into the linear EFT contributions will generalise well to the higher order terms that are naturally present in the cross section expansion.

5.1.1 Analysis Setup and Fit Methodology

The process of interest here is

$$pp \to t\bar{t} \to \ell b\bar{b}jj + \not{E}_T\,, \tag{5.3}$$

with the corresponding Feynman diagram shown in Fig. 5.1. Events are generated using MadGraph5 [338] via FeynRules [433] for Feynman rules calculations and SMEFTSim [434, 435] to include the effective operators of the SMEFT Lagrangian, which are exported to MadGraph5 via

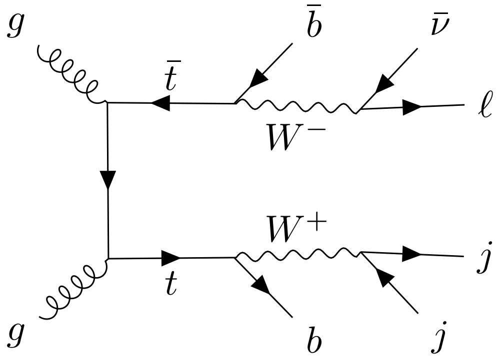

Figure 5.1: Representative Feynman diagram for the process that can receive corrections from dimension-six operators.

the UFO format. Whilst here a choice has been made to focus on the leading order contributions for analysis purposes, it is worth noting that the higher order terms would be critical for agreement between the SM and experimental data, however, it is equally worth pointing out that neglecting such terms will not impact the qualitative results of this exploration of the power of GNNs in an EFT context, and use of the TopFitter software [413, 436–438] validates this approach by finding that the higher order terms are not important here.

The $\sqrt{s} = 13$ TeV analysis by the CMS collaboration in Ref. [439] is used as an instructive example of an investigation of the correlated differential measurements and representative data binning as given in Tab. 5.1. SM data is used as a reference point at the luminosity $\mathcal{L}_{\text{ref}} = 2.3\ \text{fb}^{-1}$ of Ref. [439] and the statistical uncertainties are scaled relative to this luminosity, with $\sqrt{\mathcal{L}_{\text{ref}}/\mathcal{L}}$ used for extrapolation. This construction of an analysis chain depends on showering events with Pythia8 [164] before feeding them into Rivet [440, 441] and subsequently the fit.

To steer clear of any assumptions about correlations and avoid double counting events (and thereby artificially inflating the sensitivity to the EFT contributions), when bin-to-bin correlations are included, a single distribution is used, and a single bin used when they are not. If the reference analysis does not provide a full correlation and covariance matrix, the choice of bin or distribution used is made on a coefficient-by-coefficient basis, selecting the input with maximum deviation from a fixed point on that axis. This comprises a maximal sensitivity and minimal correlation assumption input, which is used for finding the bounds for each coefficient in both the individual and profiled cases. Further details can be found in Refs. [4, 412, 413]. Throughout the rest of this

Distribution	Observable	Binning
$\frac{1}{\sigma}\frac{d\sigma}{d\lvert y_t^h\rvert}$	$\lvert y_t^h\rvert$	$[0.0, 0.2, 0.4, 0.7, 1.0, 1.3, 1.6, 2.5]$
$\frac{1}{\sigma}\frac{d\sigma}{d\lvert y_t^l\rvert}$	$\lvert y_t^l\rvert$	$[0.0, 0.2, 0.4, 0.7, 1.0, 1.3, 1.6, 2.5]$
$\frac{1}{\sigma}\frac{d\sigma}{d\lvert y_{t\bar{t}}\rvert}$	$\lvert y_{t\bar{t}}\rvert$	$[0.0, 0.2, 0.4, 0.6, 0.9, 1.3, 2.3]$
$\frac{1}{\sigma}\frac{d\sigma}{dp_\perp^{t,h}}$	$p_\perp^{t,h}$	$[0, 45, 90, 135, 180, 225, 270, 315, 400, 800]$ GeV
$\frac{1}{\sigma}\frac{d\sigma}{dp_\perp^{t,l}}$	$p_\perp^{t,l}$	$[0, 45, 90, 135, 180, 225, 270, 315, 400, 800]$ GeV
$\frac{1}{\sigma}\frac{d\sigma}{dm_{t\bar{t}}}$	$m_{t\bar{t}}$	$[300, 375, 450, 530, 625, 740, 850, 1100, 2000]$ GeV
$\frac{1}{\sigma}\frac{d\sigma}{d\lvert y_{t\bar{t}}\rvert d\lvert m_{t\bar{t}}\rvert}$	$\lvert y_{t\bar{t}}\rvert$	$[0.0, 0.2, 0.4, 0.6, 0.9, 1.3, 2.3]$
	$m_{t\bar{t}}$	$[300, 375, 450, 625, 850, 2000]$ GeV
$\frac{1}{\sigma}\frac{d\sigma}{dp_\perp^{t,h}d\lvert y_t^h\rvert}$	$p_\perp^{t,h}$	$[0, 45, 90, 135, 180, 225, 270, 315, 400, 800]$ GeV
	$\lvert y_t^h\rvert$	$[0.0, 0.5, 1.0, 1.5, 2.5]$

Table 5.1: Distributions provided in Ref. [439] and included in the fit in this chapter.

chapter, bounds for the operators are considered using the dimensionless "bar" notation;

$$\bar{C}_i = C_i \frac{v^2}{\Lambda^2}\,, \tag{5.4}$$

with the electroweak VEV $v = 246$ GeV.

5.2 Graph Representation of Events

To use GNNs in this context, the events naturally must first be restructured into a graphical structure, consisting of nodes, their features and edges between the nodes. There are a range of ways to go about this process, and here a physically motivated strategy is used, with the graphs created in the image of the decay chain of the process in Eq. (5.3) and in the fashion of Fig. 5.2, using the infra-red safe and detectable final states. To this end, the data samples are processed with several selection criteria; events must have at least two jets that are not b-tagged with transverse momentum $p_T(j) > 20$ GeV and pseudorapidity $|\eta| < 5$. Further, the event is discarded if there are fewer than two b-jets and one lepton ℓ in the central part of the detector ($|\eta(\ell)| < 2.5$), where the b-jets must also satisfy $p_T(b) > 20$ GeV. The events that pass these criteria are then embedded into graphs by defining nodes, their features and edges.

Dealing first with the nodes, in simple terms, these correspond to the elements in the decay chain. In practice, the first step is to identify the missing transverse momentum (MTM) through the usual technique of balancing out the net detected transverse momenta. This is the first defined node. Then, each lepton is used to reconstruct the four-momentum of the W boson as a sum of the lepton's four-momentum and the MTM. If the invariant mass of this candidate W boson is found to fall within the range $[65, 95]$ GeV then it is added as a node W_1, and a further node b_1 is added for the b-jet that has the smallest separation $\Delta R = \sqrt{\Delta\eta^2 + \Delta\phi^2}$ from W_1. Should there be multiple valid MTM solutions, then the one which combines with the lepton to give an invariant mass closest to the W mass is used. Next, the top quark is reconstructed as a node t_1 using the four-momenta of ℓ, b_1 and the MTM. In the same vein, combinations of jets are considered in search of a pair with dijet invariant mass $70\text{ GeV} \leq m(jj) \leq 90\text{ GeV}$, which then receive their own nodes j_1, j_2, along with a node for the second W boson, W_2. If no suitable pair is found for W reconstruction, then the nodes are added only for the leading two jets. Out of those b-jets that remain, the leading one becomes a node b_2, and a second top node t_2 is also added, with its four-momentum reconstructed using b_2, j_1 and j_2. Some events may have yet further jets that contain useful information, so any jets within $\Delta R < 0.8$ of the existing nodes are added as nodes which will be connected only to the nearest existing node.

Each of these nodes is given a feature vector consisting of the transverse momentum, pseudorapidity, azimuthal angle, energy, mass and particle identification number (following the PDG convention [442]); $[p_T, \eta, \phi, E, m, \text{PID}]$.

Turning now to edges, the crucial connections between the nodes that create the adjacency matrix, the nodes of the final states are connected to the reconstructed objects from whence they came, so as to mimic the physical decay structure. The first step here is connecting the MTM and lepton to W_1, and then W_1 and b_1 to t_1. In the case where W_1 is not found, the final states are connected directly to t_1. For the other side of the decay chain things proceed similarly, with the jet nodes j_1 and j_2 connected to W_2, if the latter is successfully reconstructed, and then the W_2 and b_2 nodes are connected to the top node t_2. Again, if there is no W_2 node, the jet nodes are connected directly to the top node. Finally, any remaining nodes from the final state are connected to the nearest (in terms of ΔR separation) node. There is room for error in the assigning of the b quarks to the t quarks, but the minimum ΔR construction is the most practical and is a better measure the more highly boosted the t quark is. The resulting graph bears a resemblance to the underlying physical process as a result of this construction; compare the representative graph structure shown in Fig. 5.2 and the Feynman diagram in Fig. 5.1.

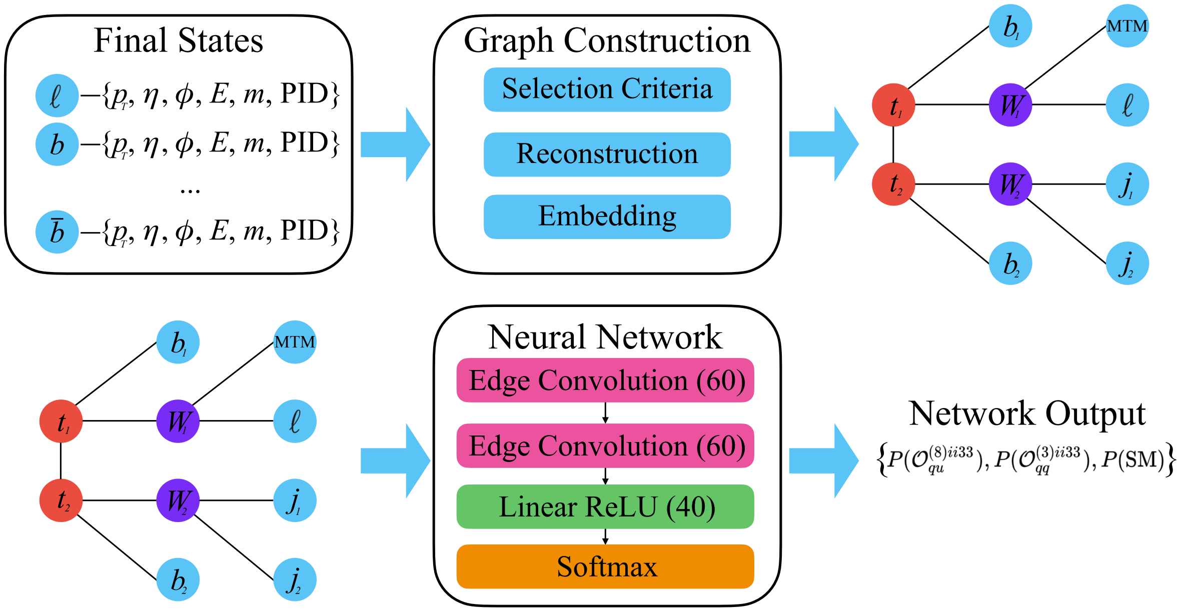

Figure 5.2: The processing flow of the analysis, turning final states into a graph structure, a representative of which is depicted here, though this may vary depending on the reconstruction. The graph is then fed into the neural network, the outputs of which are the probabilities of an event belonging to each class.

5.2.1 Graph Neural Networks with Edge Convolution

Convolution neural networks are a source of active research, with the capability to employ multi-scale localised spatial features. However, a notable limitation of such networks is their preponderance for regular Euclidean data such as images, making them less suited for particle physics applications. This limitation has been overcome through recent developments in GNNs, which generalise their convolutional cousins to operate on data structured as graphs, allowing the non-Euclidean domains of the data to be probed [443]. These developments take the form of Message Passing Neural Networks (MPNNs) [422] for supervised learning applications. This can then be generalised for the edge convolution of the sort used in this chapter.

MPNNs consist of two main components. As one would expect, one is a message passing phase, which is defined as a mathematical operation between two nodes, denoted as i and j, with feature vectors $x_{i,j}^{(l)}$ and an edge connecting the two with a vector $\mathbf{e}_{ij}^{(l)}$ at the l^{th} time step. The vector nature of the edge is a consequence of the directed nature of the graph. Graphs can be directed or undirected; in this chapter bi-directional graphs are used.

In the message passage phase, the message itself, $\mathbf{m}_{ij}^{(l)}$, is computed between two nodes via the mathematical operation $\mathbf{M}$:

$$\mathbf{m}_{ij}^{(l)} = \mathbf{M}^{(l)}(\mathbf{x}_i^{(l)}, \mathbf{x}_j^{(l)}, \mathbf{e}_{ij}^{(l)})\,. \tag{5.5}$$

In this instance, a linear activation function is used for the message function. When all the messages between all the connected nodes in a layer have been calculated, the message passing phase is completed and then each node feature is updated using an aggregation function

$$\mathbf{x}_i^{(l+1)} = \mathbf{A}(\mathbf{x}_i^{(l)}, \{\mathbf{m}_{ij}^{(l)} \,|\, j \in \mathcal{N}(i)\})\,, \tag{5.6}$$

where $\mathcal{N}(i)$ are the neighbouring nodes connected to ith node, and $\mathbf{A}$ is some function that must be permutation invariant. Taking the mean, the maximum or the sum are typical functions for this aggregation. The thus updated features are then used as inputs for the next layer, unless this is the final layer, in which case they are used for the loss function in the network.

In order to classify the graph, once the message passing operation L has been performed, a permutation invariant graph readout operation $\square$ is deployed on the final node features $x_i^{(L)}$, given by

$$\mathbf{X} = \square(\mathbf{x}_i^{(L)} | i \in G) \tag{5.7}$$

for an input graph G. The resulting vector $\mathbf{X}$ is of a fixed length, irrespective of the size and configuration of the graph, and this can be then fed into the neural network consistently and safely. The edge convolution operation used here is defined as

$$\mathbf{x}_i^{(l+1)} = \frac{1}{|\mathcal{N}(i)|} \sum_{j \in \mathcal{N}(i)} \textsc{ReLU}\left(\Theta.(\mathbf{x}_j^{(l)} - \mathbf{x}_i^{(l)}) + \Phi.(\mathbf{x}_i^{(l)})\right)\,, \tag{5.8}$$

where Θ and Φ are linear layers that map the input vectors to vectors of the same dimension. The aggregation function used is the mean, with two layers used with the mean as the graph readout operation.

5.2.2 Network Architecture and Training

To implement the GNN, the common tools of Deep Graph Library [444] and PyTorch [445] are used, with the former useful for the graph construction and operations and the latter for neural network classification. Models are trained on data samples with 70000 events for each operator with a split of 80%, 10% and 10% used for training, validation and testing respectively. The networks thus constructed consist of edge convolution layers followed by hidden linear layers with ReLU activation functions. Application of the softmax function to the final layer yields the probability that an event belongs to each of the classes. For training of the network, the categorical cross-entropy loss function is used with the Adam optimizer [176] with a learning rate of 0.001. This learning rate decays by a factor of 0.1 if the calculated loss fails to fall for three consecutive epochs. The model is trained for 100 epochs with batches of 100 events and an early stopping condition that kicks in when the loss does not fall for ten epochs.

In order to find an optimal configuration of the network, a number of different architectures are explored and trained on the data, from which it is found that the combination of two edge convolution layers of 60 nodes and a single hidden linear layer of 40 nodes performs notably well. The final architecture is shown in Fig. 5.2. As always in machine learning, the spectre of overtraining must be guarded against, and indeed there are signs of overtraining in the loss and accuracy curves when deeper networks are used. That the comparatively shallow network is still able to perform admirably speaks to the fact that the relevant physics can be contained within a small number of physical phenomena, which is in line with the findings of EFT fits performed in the traditional fashion [399].

5.3 Wilson Coefficient Constraints Improved by GNNs

The aim of developing these GNNs is of course for use as tools in constraining EFTs; in particular the WCs in the top sector. There are still a large number of operators at play however, and it is thus prudent to first explore a more minimal selection so as to demonstrate the power of the GNN approach before then diving into the full selection.

5.3.1 A Minimal Example

To begin things then, a three class problem is picked, which is the simplest possible configuration, with the SM contributions and two effective interactions. The network is then built and trained, with the output being the probability of an event belonging to each of these three classes, and events are then catalogued as the class with the largest output. As for the operators chosen for this minimal example, they should reflect a generic and representative phenomenology for EFTs. Interactions that modify SM couplings can fulfil this criteria as they yield modified inclusive rates with momentum related distributions similar to the SM case, as the momentum dependent

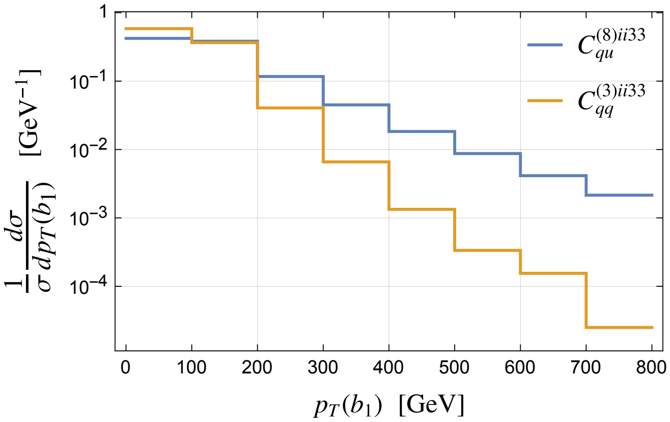

Figure 5.3: The normalised $p_T(b_1)$ distributions at the 13 TeV LHC of the process Eq. (5.3) from the two operators of the three-class example, Eq. (5.9).

interactions normally boost the tails of these distributions. This feeds into notable phenomenona such as a modified top quark width. Two suitable operators are

$$\begin{aligned} \mathcal{O}_{qu}^{(8)ii33} &= (\bar{q}_i \gamma_\mu T^A q_i)(\bar{u}_3 \gamma^\mu T^A u_3)\,, \\ \mathcal{O}_{qq}^{(3)ii33} &= (\bar{q}_i \gamma_\mu \tau^I q_i)(\bar{q}_3 \gamma^\mu \tau^I q_3)\,. \end{aligned} \tag{5.9}$$

The p_T distributions of the leading b-jet from these operators are shown in Fig. 5.3, from which it can be seen that the phenomenology is particularly distinguishable, consolidating the reasoning behind the choice of these two operators. The harder the event, the more the final states will be located centrally in the detector, with related modifications to the angular and rapidity situtations, hence the expectation that these differing distributions will allow the network to effectively discriminate between the two operators, as is crucial for a sensitive EFT analysis. This choice of operators also facilitates the discussion of the limitations of the GNN approach.

The network outputs are shown en masse on the left of Fig. 5.4, with each point representing a single event and the network assigned probability of originating from one of the SMEFT operators. This is indicative of good network performance, as the events from $\mathcal{O}_{qu}^{8(ii33)}$ are primarily clustered in the upper left region that corresponds to the network assigning these events high probabilities of being from $\mathcal{O}_{qu}^{8(ii33)}$, with those events from $\mathcal{O}_{qq}^{3(ii33)}$ mainly in the lower right region, as one would hope. The SM events lie in a region where the probabilities for $\mathcal{O}_{qu}^{8(ii33)}$ and $\mathcal{O}_{qq}^{3(ii33)}$ are both low, and thus the chance of being a SM event is high. This is indicative of the fact that

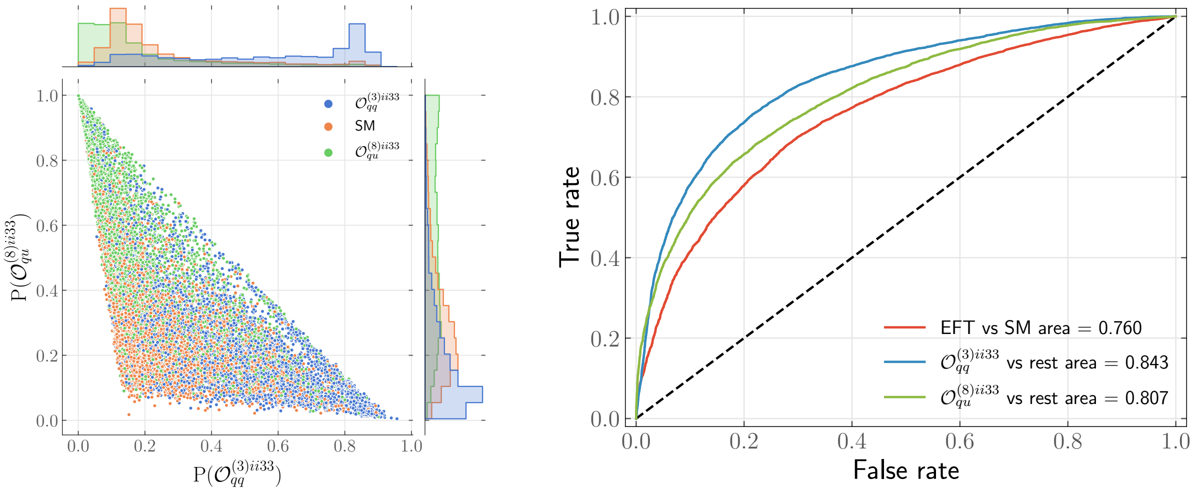

Figure 5.4: The probabilities calculated for each event to be a result of each SMEFT insertion are shown. On the right, the Receiver Operator Characteristic (ROC) curves are shown. These are calculated in a one-vs-rest scheme for each operator.

the network can be used effectively to select classes based on cuts on the output probabilities. The individual 2D histograms for each class are additionally shown in Fig. 5.5. The right hand of Fig. 5.4 shows the receiver operating characteristic (ROC) curves, calculated in a one vs rest scheme. In addition, the ROC curve for EFT events against the SM is shown.

To show the efficacy of the GNN approach for this minimal example, an analysis framework that yields constraints on the WCs must be developed, and in this the ever handy χ^2 fit comes into play. In particular, the observable used to construct the χ^2 is the transverse momentum of the leading b-jet, $p_T(b_1)$, with the χ^2 calculated as in Ref. [413]. In the hope of gaining as much statistical control as possible, the results are extrapolated to the expected performance of the HL-LHC, $\mathcal{L} = 3\text{ab}^{-1}$, but it is important to note that the qualitative pattern of results does not depend on the luminosity. This analysis provides a baseline against which the relative improvement of the GNN approach can be judged, and is shown in black in Fig. 5.6.

Finally, it is time to assess the power of the GNN approach. To do so, the datasets are subjected to cuts on the network assigned probability of belonging to a given class, such that only events with a probability greater than some chosen threshold value are considered in the χ^2 fit. The good performance of the network allows for the selection of a threshold probability, thereby substantially reducing the SM background and also the signal contamination from the other

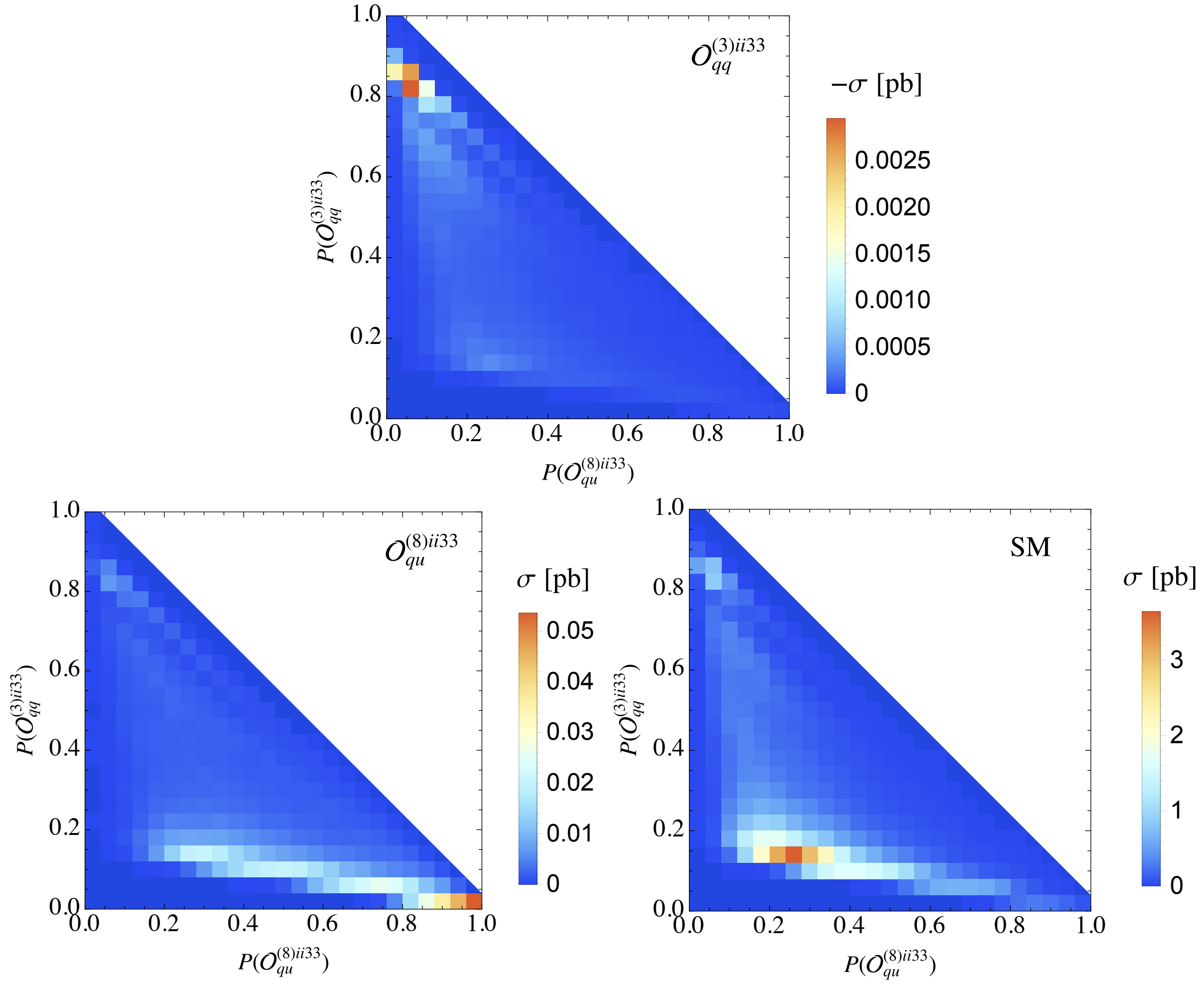

Figure 5.5: Example two-dimensional histograms for the network output from each contribution, with each $C_i/\Lambda^2 = 1$ TeV^{-2}, normalised to the cross section rate.

operator, which results in a boosted signal effect and thus a tighter constraint on the WC for the operator for which the cut is performed. Optimising the value of the probability to cut on requires a degree of tuning, as the desire for maximal performance must be balanced with the danger of losing statistical control by completely depleting bins in the SM $p_T(b_1)$ distribution, which would lead to unrealistic bounds. The constraints from this approach are shown as the blue and red contours in Fig. 5.6.

Taking this path does indeed yield improved constraints on the coefficient for which the probability

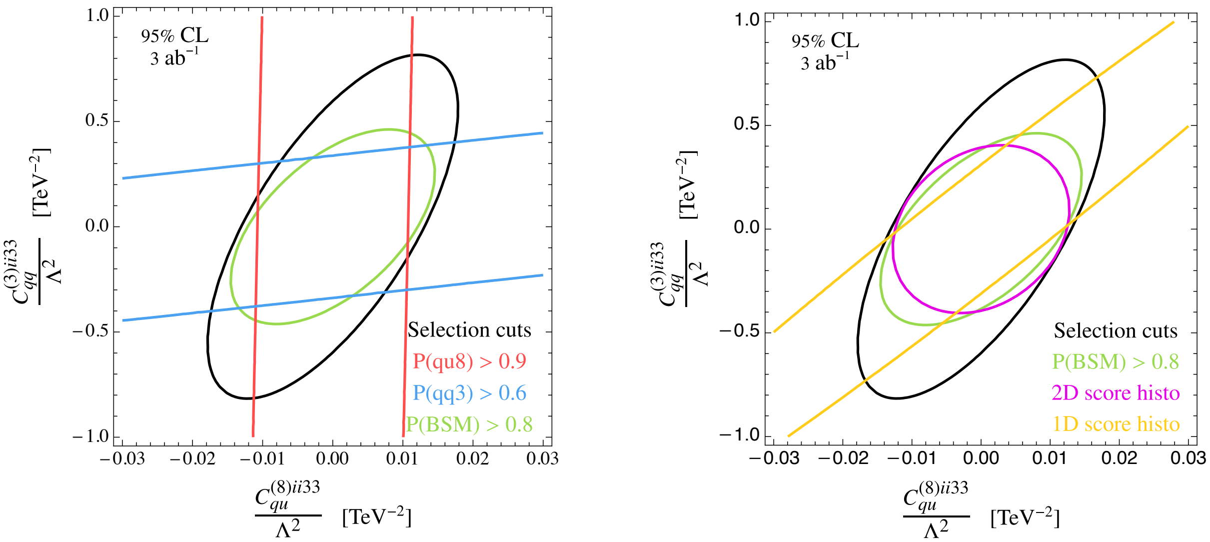

Figure 5.6: WC constraint contours at the 95% C.L. from χ^2 fitting; in black from the data of the baseline selection of Sec. 5.1 which also passes the network requirements. The left plot shows the contours from cuts on the NN scores at the optimal value of these score cuts, with the analysis performed using $p_T(b_1)$ distributions. The right plot shows the BSM score cut as in the left plot, along with the contour from the 2D score histogram of Fig. 5.5 (with no score cuts) analysis as well as an analysis using the 1D BSM score histogram. For details see text.

cut is performed, however, the other coefficient is all but unconstrained, a far worse performance than that of the full dataset. This is a promising start, but clearly not a convincing solution. Seeking such a solution, the probability P(BSM) can be used, which is simply the combined probability of the network output probabilities:

$$\mathrm{P(BSM)} = \mathrm{P}(\mathcal{O}_{qu}^{(8)ii33}) + \mathrm{P}(\mathcal{O}_{qq}^{(3)ii33}). \tag{5.10}$$

The resulting bound from this new quantity does indeed result in a combined bound that is superior to the original analysis, and is shown in green in Fig. 5.6.

Constraints could also be found by direct use of the output of the GNN; using the 2D histograms like those Fig. 5.5, in place of the $p_T(b_1)$ distributions of Fig. 5.3. In this fashion, a d dimensional classification can be reduced to a $d-1$ dimensional probability histogram, thereby condensing the phenomenologically available information for operator classification. The resulting contour from this method, using a total of 15 bins (the maximum possible before reaching statistical depletion), is shown in purple on the right plot of Fig. 5.6, and demonstrates an improvement on the bounds found compared to the original $p_T(b_1)$ distribution analysis, without the requirement of performing cuts on the data. However, this method can quickly become limited once the number of operators is increased, as using the full $d-1$ dimensional histogram rapidly increases the statistical uncertainty. From the qualitative likeness of the two approaches, it would appear that, for multi-dimensional EFT analyses, particularly at luminosities below 3 ab^{-1}, an adequate approach is the minimisation of

$$\mathrm{P(SM)} = 1 - \mathrm{P(BSM)}. \tag{5.11}$$

To take things further, it would be possible to use the P(BSM) histogram to construct a χ^2 and thus constraints, but the sensitivity found from this approach and shown in Fig. 5.6 in orange is limited compared to the other approaches. This is because of the information loss that occurs when projecting the two dimensional output down to a one dimensional histogram, and so this approach is not explored further.

5.3.2 Fit Constraints with GNN Selections

And finally it comes time to unleash the full potential of the GNN approach by expanding the above approach to the thirteen dimensional SMEFT parameter space. The resultant ROC curves for the network built and trained for the full classification are shown in Fig. 5.7 and have been calculated with the generalised procedure discussed above. The hyperparameters have again been

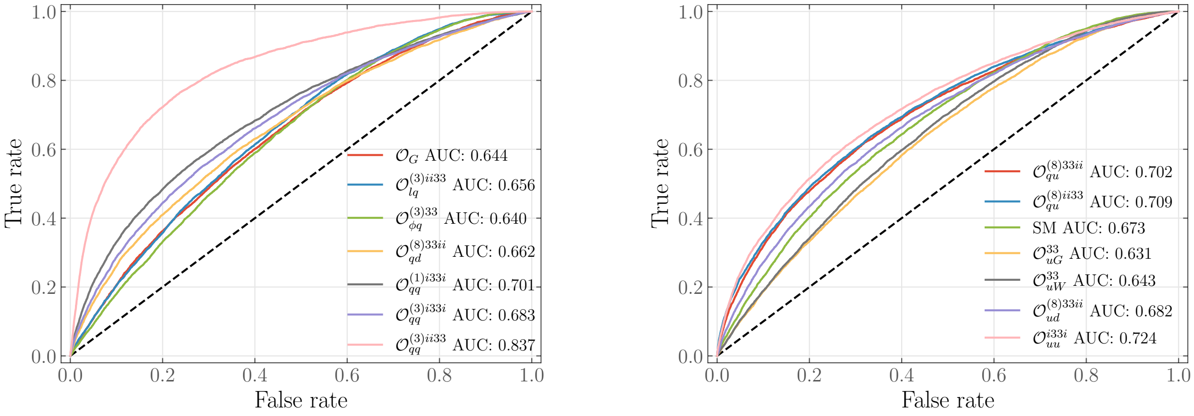

Figure 5.7: ROC curves for the scenario where multi-class classification is performed on thirteen SMEFT operators and the SM.

	$2.3\ \text{fb}^{-1}$		$3\ \text{ab}^{-1}$	
	Individual	Profiled	Individual	Profiled
$\bar{C}_G$	$(-0.0543, 0.0535)$	$(-0.1785, 0.1776)$	$(-0.0015, 0.0015)$	$(-0.0047, 0.0047)$
$\bar{C}_{\varphi q}^{(3)33}$	$(-0.0317, 0.0326)$	$(-0.0806, 0.0758)$	$(-0.0009, 0.0009)$	$(-0.0022, 0.0022)$
$\bar{C}_{uG}^{33}$	$(-0.0253, 0.0247)$	$(-0.0622, 0.0655)$	$(-0.0007, 0.0007)$	$(-0.0017, 0.0017)$
$\bar{C}_{uW}^{33}$	$(-0.0234, 0.0228)$	$(-0.0544, 0.0580)$	$(-0.0006, 0.0006)$	$(-0.0015, 0.0016)$
$\bar{C}_{qd}^{(8)33ii}$	$(-0.1543, 0.1558)$	$(-0.3789, 0.3698)$	$(-0.0043, 0.0043)$	$(-0.0104, 0.0104)$
$\bar{C}_{qq}^{(1)i33i}$	$(-0.0202, 0.0204)$	$(-0.0495, 0.0484)$	$(-0.0006, 0.0006)$	$(-0.0014, 0.0014)$
$\bar{C}_{qq}^{(3)i33i}$	$(-0.0101, 0.0102)$	$(-0.0247, 0.0241)$	$(-0.0003, 0.0003)$	$(-0.0007, 0.0007)$
$\bar{C}_{qq}^{(3)ii33}$	$(-3.2964, 3.3259)$	–	$(-0.0917, 0.0917)$	$(-0.3045, 0.3046)$
$\bar{C}_{qu}^{(8)33ii}$	$(-0.0867, 0.0875)$	$(-0.2127, 0.2079)$	$(-0.0024, 0.0024)$	$(-0.0058, 0.0058)$
$\bar{C}_{qu}^{(8)ii33}$	$(-0.0577, 0.0583)$	$(-0.1416, 0.1383)$	$(-0.0016, 0.0016)$	$(-0.0039, 0.0039)$
$\bar{C}_{ud}^{(8)33ii}$	$(-0.1598, 0.1613)$	$(-0.3923, 0.3824)$	$(-0.0044, 0.0044)$	$(-0.0107, 0.0107)$
$\bar{C}_{uu}^{i33i}$	$(-0.0225, 0.0228)$	$(-0.0553, 0.0540)$	$(-0.0006, 0.0006)$	$(-0.0015, 0.0015)$
$\bar{C}_{lq}^{(3)ii33}$	–	–	$(-0.3289, 0.3288)$	$(-1.8493, 1.8930)$

Table 5.2: Baseline 2σ bounds for different luminosities from running TopFitter.

optimised for this scenario and the previous architecture still performs well without suffering from the blights of overly long training times and overtraining. Again the resultant network is capable of admirable performance when distinguishing operators, albeit lower than for the three class problem, though this is to be expected given the increased complexity demanded of it.

Beginning with the baseline sensitivity of Tab. 5.2 (see also Sec. 5.1), the impact on the operator constraints from the imposition of the machine learning inspired cuts are shown in Fig. 5.7. In Tab. 5.2, the individual bounds are those found when considering only a single operator, with the contributions from the remaining effective interactions discarded. Such an austere approach naturally fails to capture the impact of the rich phenomenology at play however; hence the second column of constraints in which the other WCs have been profiled over by fixing them to the value that minimises the total χ^2 value. When the analysis is sensitive to additional operators, there will be a significant decrease in sensitivity, which can be expected as the network selection removes background contributions but keeps NP effects. In some cases, the profiled bound's

	$2.3\ \text{fb}^{-1}$		$3\ \text{ab}^{-1}$	
	Individual	Profiled	Individual	Profiled
$\bar{C}_G$	0.07%	14.12%	0.07%	11.09%
$\bar{C}_{\varphi q}^{(3)33}$	33.74%	34.19%	33.73%	33.48%
$\bar{C}_{uG}^{33}$	28.29%	32.18%	28.28%	30.74%
$\bar{C}_{uW}^{33}$	34.86%	35.35%	34.85%	35.53%
$\bar{C}_{qd}^{(8)33ii}$	4.71%	4.68%	4.71%	4.76%
$\bar{C}_{qq}^{(1)i33i}$	3.50%	3.45%	3.50%	4.73%
$\bar{C}_{qq}^{(3)i33i}$	4.35%	4.28%	4.35%	5.00%
$\bar{C}_{qq}^{(3)ii33}$	63.83%	–	63.83%	71.91%
$\bar{C}_{qu}^{(8)33ii}$	3.45%	3.51%	3.45%	3.48%
$\bar{C}_{qu}^{(8)ii33}$	3.74%	3.72%	3.74%	3.77%
$\bar{C}_{ud}^{(8)33ii}$	4.62%	4.46%	4.62%	4.79%
$\bar{C}_{uu}^{i33i}$	3.38%	3.35%	3.38%	1.95%
$\bar{C}_{lq}^{(3)ii33}$	–	–	10.57%	35.52%

Table 5.3: Maximum improvements in 2σ bounds via a cut on the network assigned score.

improvement exceeds that of the individual, which is a result of the EFT score cut picking out a region in which the impact on the bounds of a particular operator is comparatively diminished by the presence of additional operators.

Significant improvements can be achieved when there is significant momentum enhancement, as is the case with $\bar{C}_{uG}^{33}$, and the GNN also performs well when the non-resonant top decay contributions such as $\bar{C}_{uW}^{33}$ come under the microscope. On the whole, improvements between 5% and 60% can be attained, with the details given in Tab. 5.3, varying between the operator considered, although this always requires heavy cuts on the GNN output, though always avoiding the loss of statistical control. Representative operator improvements as a function of the network assigned scores score are given in Fig. 5.8. Alas, improvement across the board is not possible, with those operators that are already well controlled by the pre-existing inclusive rate and the baseline selection cuts, such as $\bar{C}_G$, seeing relatively small improvements. Such operators can however be constrained in their own tailored ways through multi-jet production [446, 447].

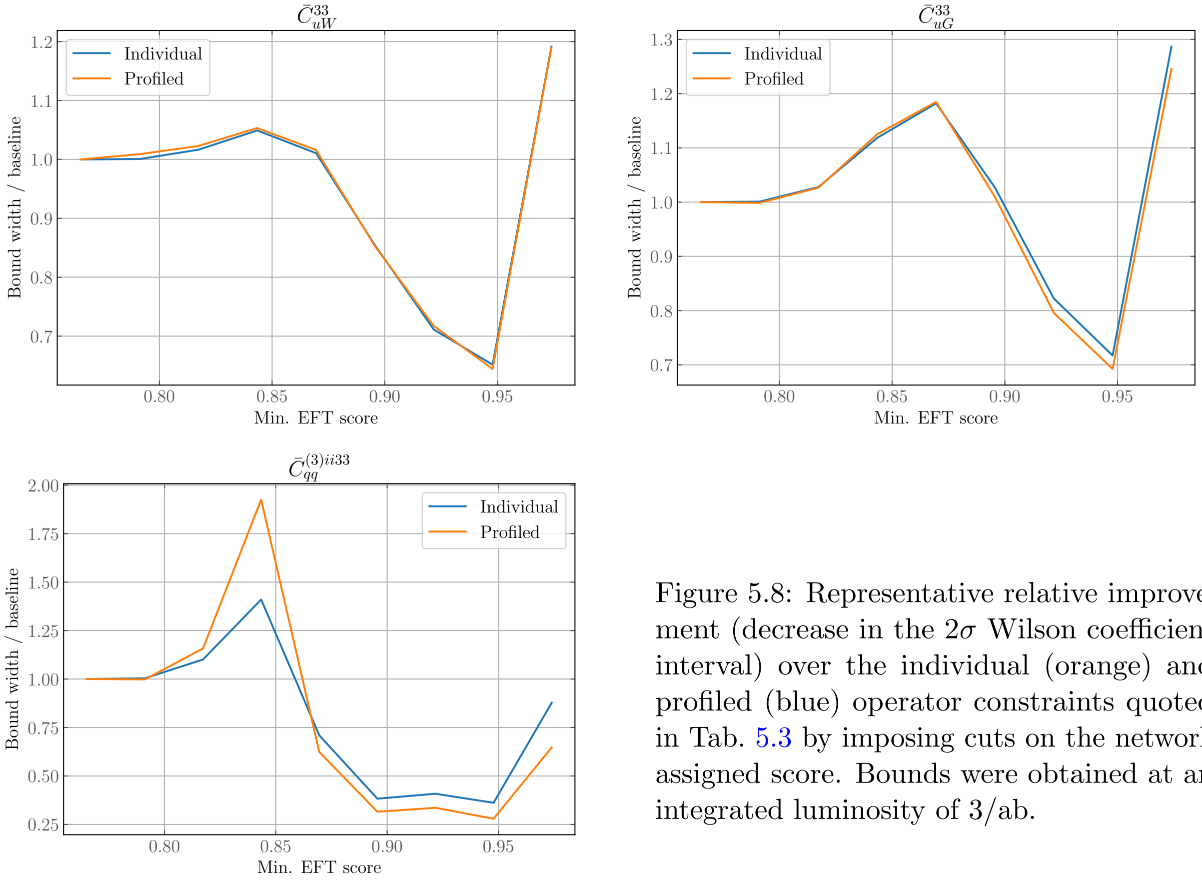

Figure 5.8: Representative relative improvement (decrease in the 2σ Wilson coefficient interval) over the individual (orange) and profiled (blue) operator constraints quoted in Tab. 5.3 by imposing cuts on the network assigned score. Bounds were obtained at an integrated luminosity of 3/ab.

5.4 Conclusions

The vast efforts directed at detecting NP have not yet thrown up any smoking gun signatures. One worthy approach is the in depth study of specific BSM models, as has been undertaken in the previous chapters. In the interest of taking a more general approach, the EFT formalism can be used, with the aim of constraining the phenomenology of NP through the observation of modifications of expected SM correlations in LHC data. Particularly deserving of consideration in the context of this thesis and its focus on Higgs physics is the SMEFT, and the drive to set the most sensitive limits possible on the relevant WCs. Traditional approaches make use of a selection of differential distributions and rectangular cuts on chosen observables, but employing machine learning techniques can give superior bounds by exploiting otherwise hidden relations and correlations in the data.

This chapter has made use of GNNs, which are well motivated in this context as they can be used to mimic the decay chain structure in the graph design. The network assigns probabilities to events so as to classify them. This analysis is based on the semileptonic $t\bar{t}$ final states, as this is phenomenologically fertile ground for new interactions, and is additionally an arena for a critically large Wilson coefficient parameter space for multi-label classification. By taking this tack, the bounds on the WCs can be significantly improved as compared to the traditional methods, showing how machine learning can be most useful for multi-labelled collider data in the context of improving the sensitivity of EFT related measurements at colliders. The improvement is found across the board, in both the individual and profiled bounds on the WCs, and the results also indicate profiled bounds can be improved by tensioning operators against each other, highlighting relative operator probabilities as another avenue for future investigations. In this vein, more model specific EFT constraints can be included in the machine learning framework by optimising the GNN output scores through different weightings of the individual class probabilities, in principle further enhancing the sensitivity available.

This chapter forms an exploratory study aimed at illustrating the possible power of the machine learning approach, and it is worth noting that these results are based on a Monte Carlo analysis, and naturally the actual experimental data is buffeted by an assortment of uncertainties. Here these uncertainties are neglected, though they could in principle be dealt with by Generative Adversarial Neural Networks [448, 449], with other approaches given in Ref. [450] and Ref. [451] for ameliorating the theoretical and experimental uncertainties respectively. Whilst the quadratic EFT terms of Eq. (5.2) were negelected for valid reasons here, they would generally be important and so should be considered in analyses that build upon this one. The quest for increased generality in the detection of NP states through GNN usage continues apace in the next chapter.

Chapter 6

Anomaly Detection with Graph Neural Networks

As is hopefully abundantly clear at this point, the search for NP has not yet borne any fruit. Whilst the tensions between experimental results and the SM grow, and exceedingly strong evidence exists that there must be some as yet undiscovered physics at play, the concrete signals continue to elude detection at the LHC and other collider environments. One outcome of this impasse has been the proliferation of BSM models, from the more straightforward to the more inventive and, at times, esoteric. Despite this lively theoretical milieu, no single model can claim to stand above all others. Of course, it is still well worth examining each model on its merits to pin down precisely what parameter space remains permissible in the face of the plethora of data, hence the studies of particular models presented in Chapters 3 and 4.

Pursuit of this path is perhaps problematic however, owing to the ever expanding collection of both data and models to pin down, possibly leading to an unending quagmire of phenomenological studies. Prompted by this, model independent frameworks, most notably EFTs, have been developed, and these too have been the subject of many detailed analyses seeking to constrain WCs from a selection of data. There are all sorts of avenues to venture down in this quest, and one possible approach, leveraging the power of machine learning, was examined in Chapter 5. There are also some issues here however, such as the assumption that NP acts at some high energy scale, leaving only slight footprints in current collider data and then proceeding to place constraints on the models, whilst concrete models focus only on a pertinent subset of operators [452–454].

Whilst the EFT framework does provide a good step towards generality and model independent searches, it is still a framework cast very much in the current understanding of physics, and predicated upon some assumptions that may not be valid, such as the energy scale gap to NP. Furthermore, it would be most impudent to believe that the Universe is kind enough to conform to these frameworks and our expectations of what NP may look like, and so it is only prudent to continue reaching for generality in the search for NP signals.

Something strange is afoot – this much can be said for sure. The current crop of colliders has not observed any unexpected particles and yet the SM is almost certainly an incomplete model of nature. The range of BSM models and vast data production make individual searches laborious and nigh Sisyphean, while the EFT framework falters in certain circumstances, for instance light NP. To proceed, perhaps the best way is to shed the preconceptions of how NP may present and instead seek out the anomalous events directly.

There is no need to throw the baby out with the bathwater though, and collider data remains the best avenue for NP detection. Seeking out these anomalies in this otherwise well understood data is one valid method [455–463]. One of the apparent drawbacks of the LHC is the large QCD background, and it may be that this has allowed anomalous signals to remain masked, but on the flip side, this means that QCD jets are very well studied, with a great deal of effort put into understanding their behaviour [42]. The unfolding of the typical QCD events from high to low energy is well understood as a result, hence the success of Monte Carlo programmes when applied to the modelling of the QCD showers in collider data (see e.g. Ref. [464]). It stands to reason then, that by classifying jets, possibly using motivated first-principle approaches [465, 466], and discarding what can be regarded as a standard QCD jet, the remaining events may be the BSM signatures that are so sought after. This is the process of anomaly detection in LHC data.

Buoyed by the success of the foray into machine learning in the previous chapter, this chapter will again deploy this method, though in a somewhat different approach to the EFT examination. Recently, a range of cutting edge techniques for anomaly detection with deep learning have been dreamt up [410, 425, 455, 457–463, 467–469]. In this particular case, the tool of choice is an autoencoder, which is designed to recreate the most prevelant traits of the training data through dimensional reduction of the input features. Should a BSM event be fed into such a network, trained to accurately identify QCD events, the network can be expected to perform poorly, and so the BSM signatures can be identified by this poor performance.

Whilst convolutional autoencoders can be used in this type of jet classification [431, 468, 470–474], their reliance on “jet-images” [475, 476] as the input space is a significant limitation, as these images are typically very sparse, making performing convolutions on them computationally expensive. In addition, the nature of convolutional neural networks confines their efficacy to Euclidean data. To combat these issues, the GNN is deployed again. This type of neural network has been shown to perform well for QCD phenomenology in Ref. [424], is also capable of exploiting the Lund-plane representation of splittings [477, 478], and has shown promise as a real-time trigger at the LHC [479].

GNN jet classification can be supervised [424, 426, 480] or unsupervised [425], and the performance in the context of anomaly detection with autoencoders was carried out in the LHC Olympics community challenge [481]. However, the existing GNN based autoencoders, such as those in Refs. [482–486], focus on the classification of nodes or predicting the links between them, rather than classifying the full graph, which is the goal here as this additionally facilitates the exploitation of the full kinematic information of the jet through the multidimensional edge information inherent in the graph structure. This also aids in overcoming a common limitation in GNN autoencoders, whereby they struggle to reflect all of the network features in the decoding process, but by using inner product layers, the decoder can simultaneously reconstruct multidimensional edge and node features. The latent space representation structure can also be used for NP detection [487].

The details of the events simulated and then fed into the network are given in Sec. 6.1, with an overview of the GNN formalism and the details of the structure used here given in Sec. 6.2, before the results of this procedure are shown and discussed in Sec. 6.3.

6.1 Event Simulation

This analysis will focus on the standard 13 TeV LHC collider environment, simulating a collection of events using MadGraph5 [338] to generate the events at leading order, which are then showered and hadronised with Pythia8 [164]. The resulting final hadronic states are then subjected to jet clustering through the anti-k_t algorithm [37], with the jet radius set to $R = 1.5$ in the FastJet [170] analysis, with the requirements of jet rapidity $|y| < 2.5$ and a minimum transverse momentum $p_T > 1$ TeV. No detector simulation is applied, and the leading jet from each event is then used as an input to the GNN via the graph construction method that will be outlined in Sec. 6.2.

The QCD background sample used to train the autoencoder is a multi-jet background sample of

200k $pp \to jj$ events, with the leading jet of each event picked. Choosing the leading QCD jet is sufficient when considering only a LO QCD expansion, but a more general and less exploratory analysis than this should ensure greater accuracy by including higher orders. Three different potential signal samples are used as the anomalies for the autoencoder to detect, each of which is a 100k event sample, with the processes chosen for their jet structure, being two, three and four pronged structures respectively and are:

1. boosted hadronically-decaying W bosons,
2. boosted hadronically-decaying top quarks,
3. a boosted scalar ϕ decaying as $\phi \to W^+W^- \to 4j$.

The interactions of the new scalar ϕ are given by the simplified Lagrangian

$$\mathcal{L} \supset -\frac{c_1}{v}\phi W^{\mu\nu}W_{\mu\nu} - c_2(u\bar{u} + d\bar{d})\phi, \tag{6.1}$$

for dimensionless constants c_1 and c_2 and the Higgs VEV v. The mass of this scalar is set to be 700 GeV, but the results found are fairly independent of this mass choice.

In place of the individual particles in the final and intermediate states used for the construction of the graph in the previous chapter, here microjets are used, which are known to be under solid control experimentally [488]. These microjets are found by reclustering the fat jet constituents with a finer radius $R = 0.1$ and minimum $p_T = 5$ GeV, again using the infra-red and collinear safe anti-k_T algorithm, with fat jets of at least three microjets considered in the analysis.

These microjets are used as the nodes for the network, with each fat jet corresponding to a single graph. Each node has an associated feature vector $[\log p_T,\ \Delta\eta\ , \Delta\phi,\ \Delta R, \bar{m}]$, where the differences are taken between the microjet and the jet axis, and $\bar{m}$ is the microjet mass divided by 100 GeV so as to achieve a similar range as the angular observables, with the same reasoning being behind the taking of the log of p_T.

Edges are created between all nodes, and each edge also has a feature vector. To capture the physics between the nodes, two slightly different distance metrics, along with an invariant mass, are used, with the former constructed using the metric

$$d_{ij} = \min(p_{Ti}^{2p}, p_{Tj}^{2p})\frac{R_{ij}^2}{R^2},$$

where $p = 0$ for Cambridge-Aachen (CA) jets, $p = 1$ for k_t jets and R is radius parameter for the fat jet. The CA metric gives information about the geometric distance between microjets, and the k_t metric is motivated by the nature of QCD splittings [36, 489]. The resultant edge feature vector is thus $\mathbf{e}_{ij} = (d_{ij}^{\text{CA}}, \log d_{ij}^{k_t}, \log m_{ij})$.

To allow for reconstruction of the edge features in the decoder, an adjacency matrix is defined for each of the features, such that, for a vector index a,

$$A^a_{ij} = A^a_{ji} = \begin{cases} e^a_{ij} & \text{if } i \neq j \\ 1 & \text{otherwise} \end{cases} .$$

As such, for a jet of N microjets, and thus N nodes, there will be a total of 3 $N \times N$ matrices. It is in this representation that the network outputs the edge features, and so the edge loss is a function of these matrices. Distributions of ΔR_{ij} and m_{ij} for the three leading microjets of each jet are shown in Figs. 6.1 and 6.2. The graphs are constructed and analysed using the Deep Graph Library [444] with the PyTorch [445] backend.

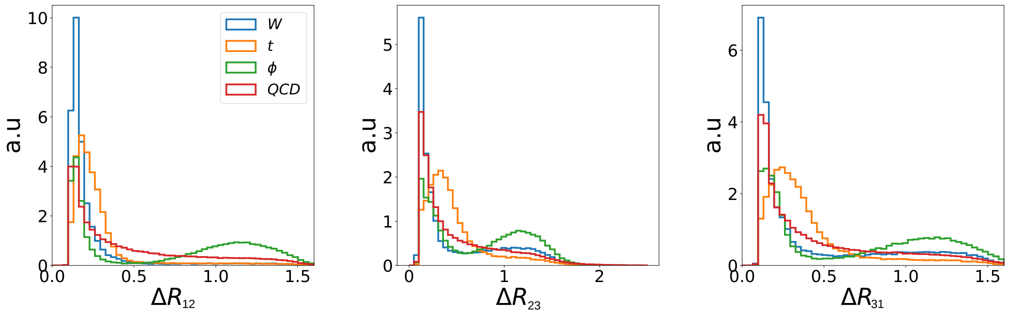

Figure 6.1: Normalised angular separation distribution between three leading microjets in the fat jet for the physics scenarios discussed in this work.

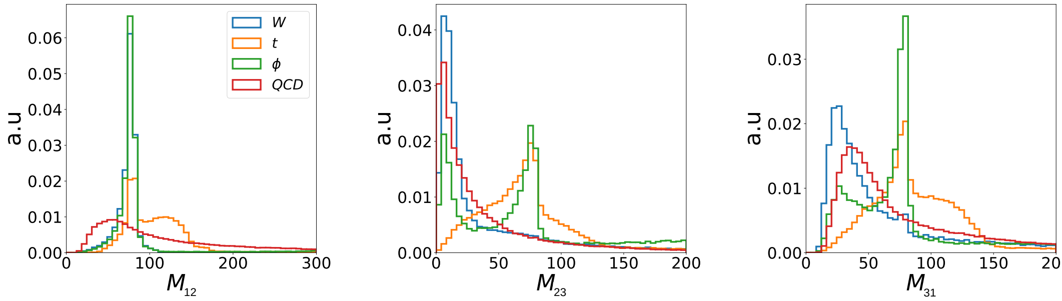

Figure 6.2: Similar to Fig. 6.1, but showing the normalised invariant mass distribution between three leading microjets in the fat jet.

6.2 Graph Neural Networks

The general formalism for GNNs has already been set out in Sec. 5.2.1, in that they can effectively extract features from data structured as graphs and generalise convolutional neural nets to non-Euclidean data. To avoid being overly repetitive only a brief sketch of the paradigm is given here, before the autoencoder is introduced in Sec. 6.2.1. In particular, the same approach to MPNNs is used here as in Sec. 5.2.1, with Eq. (5.5) and Eq. (5.6) giving the message computation and aggregation function used for node updating. One salient difference is that here a multilayer-perceptron (MLP) shared between all the edges is used for the message passing function, ($\mathbf{M}$ in Eq. (5.5)), to better facilitate the network learning the entire graph structure.

The primary point of departure from the previous chapter's approach comes in the final stage of the message passing. Previously, and generally in supervised learning, a graph readout operation is used on the final set of node features to give vectors of a set length that are then used in the loss calculations (see Eq. (5.7)). For the autoencoder approach however, the graph structure should be maintained through to the final output. Whilst graph based autoencoders are usually used for classification of nodes or edges, which leads to them focussing on learning the local structures in large graphs, the graphs used here are comparatively small. As such, the network must be capable of learning both the overarching global structures and the local features. To this end, edge reconstruction is used in the decoder, allowing the network to reconstruct, and thereby learn, the entire graph structure. Note that undirected edges are used in this application of the edge convolution technique to reflect the physical situation, in contrast to the well motivated directed edges of the previous chapter. The network architecture is shown in Fig. 6.3, with boxes delimiting the encoder, decoder and the constituent edge reconstruction network.

Finally, it is worth addressing the question of infra-red and collinear (IRC) safety. In the clustering of the jets and microjets here, the anit-k_t algorithm has been used, and it is well established that this is an IRC safe procedure, and of course this is crucial to guarantee consistency between experiment and theory to all orders in perturbation theory. By including an energy weighted message passing network [411] and developing an IRC safe graph construction method, IRC safety can be firmly entrenched in the structure of GNN based autoencoders, and it was to this end that the work in Ref. [6] was undertaken, though the details fall outside the scope of this thesis.

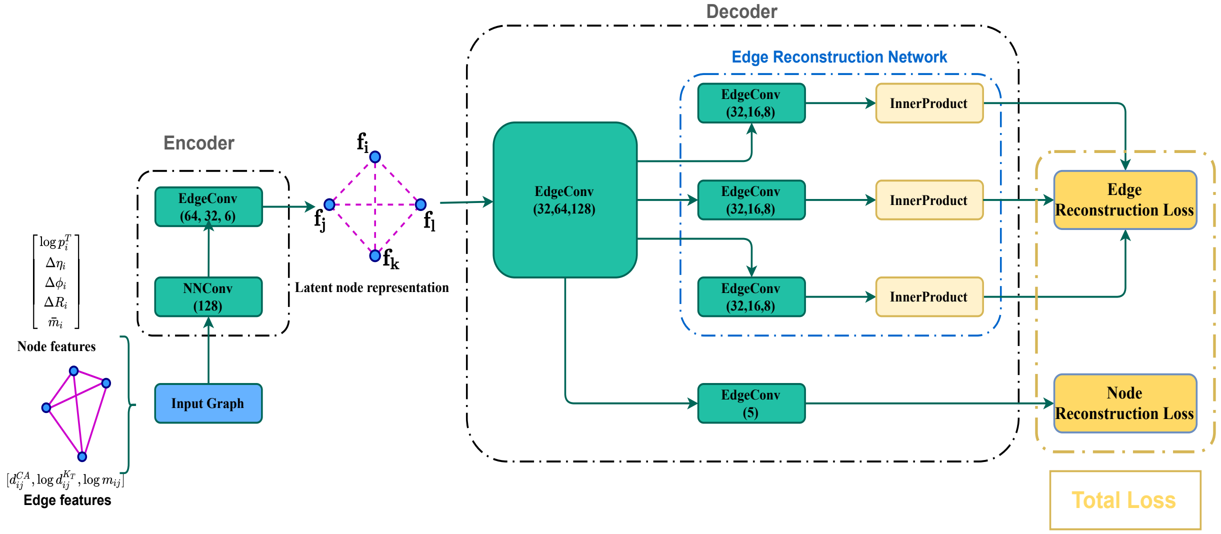

Figure 6.3: A schematic representation of a graph-autoencoder network. The network contains the encoder and the decoder. An edge reconstruction network is used in the decoder to reconstruct the multidimensional edge information.

6.2.1 Autoencoder

Turning now to the autoencoder itself, this is a neural network capable of mapping an input space to a bottleneck, or latent, dimension, and then back to the same space as the input. Here, the graph convolutions of Ref. [422] are used to include both the node and edge feature vectors, ensuring that the network learns the physical information within these. Building on the success of the previous chapter and other demonstrations of superb performance [424, 426], edge convolution [423] is again deployed. As an overview, the encoder updates the latent features $\mathbf{f}_i$ of each node, while the decoder uses this latent node representation to reconstruct the node and edge features. The decoder contains a collective edge convolution block, the output of which is fed into a single edge convolution layer for node reconstruction and three edge identical convolution blocks for edge reconstruction. The edge reconstruction is performed independently for each of the edge features, using an inner product layer [482] to do so in the form of three adjacency matrices.

Delving into the details, the initial layer of the encoder takes the raw feature vectors as inputs and uses a MLP, denoted as the edge function F_e, to perform a weighted graph convolution, mapping the edge features to a $m \times n$ dimension, where m is the dimension of the node feature vector, here five, and n is the dimension of the updated node features. The message passing function performs a broadcasted element-wise multiplication of the form

$$ {}^{ab}m_{ij}^{(1)} = {}^{ab}F_e(\mathbf{e}_{ij}) \times \ {}^{ab}\tilde{h}_j^{(0)} \,, \tag{6.2}$$

where a and b are the matrix indices, and ${}^{ab}\tilde{h}_j^{(0)}$ is formed by repeating $\mathbf{h}_j^{(0)}$, the input node features, n times. The next step in this layer is the aggregation, where the mean of ${}^{ab}m_{ij}^{(1)}$ is taken over all the neighbouring nodes j, before performing a sum over the matrix index a to yield updated n dimensional node features $\mathbf{h}_i^{(1)}$ as

$$ {}^{b}h_i^{(1)} = \sum_a \mathrm{mean}_{j\in\mathcal{N}(i)} \left(\left\{ {}^{ab}m_{ij}^{(1)} \right\} \right) \,. \tag{6.3}$$

The workhorse of the network is the edge convolution operation [423], which has two linear layers, Θ_w and Φ_w, with the same input and output dimensions, set by the dimensions of original and updated node features respectively. The message passing function is defined as (c.f. Eq. (5.8) with a slight notation change)

$$ \mathbf{m}_{ij}^{(l)} = \Theta_w(\mathbf{h}_j^{(l)} - \mathbf{h}_i^{(l)}) + \Phi_w(\mathbf{h}_i^{(l)}) \,. \tag{6.4}$$

The aggregation used here is the maximum in each component a of the incoming message vectors, yielding the updated node features $\mathbf{h}_i^{(l+1)}$:

$$ {}^{a}h_i^{(l+1)} = \max_{j\in\mathcal{N}(i)} \{ {}^{a}m_{ij}^{(l)} \} \,. \tag{6.5}$$

The inner product layer reconstructs the edge features from the node features of the last edge convolution layer, with the inner product establishing a relation to the pair of node indices corresponding to each edge. As a consequence of the undirected nature of the edges, this layer gives a symmetric $N \times N$ matrix for a graph of N nodes with components

$$ \hat{A}_{ij} = \mathbf{h}_i \ . \ \mathbf{h}_j \,. \tag{6.6}$$

A root-mean-squared error is used for both the node and edge reconstruction losses, given by

$$L_{node} = \sqrt{\sum_{i,a} \frac{(\hat{x}_i^a - x_i^a)^2}{N \times 5}} \tag{6.7}$$

for the former, where a is the node-feature index, i is the node index, and $\hat{x}_i^a$ and x_i^a are the reconstructed and input node features respectively. As for the edge reconstruction loss, this is taken as the sum over the calculated losses for the three edge features:

$$L_{edge} = \sum_a \sqrt{\sum_{ij} \frac{(\hat{A}_{ij}^a - A_{ij}^a)^2}{N \times N}} \quad , \tag{6.8}$$

where a is the edge-feature index, i and j are node indices, and $\hat{A}_{ij}^a$ and A_{ij}^a are the reconstructed and input adjacency matrices respectively. Finally, the total loss is found as a weighted sum of the individual losses;

$$L_{auto} = \lambda_{node}\, L_{node} + \lambda_{edge}\, L_{edge}, \tag{6.9}$$

where the weights are set as $\lambda_{node} = 0.2$ and $\lambda_{edge} = 1$, such that the combination of the five node features is weighted equally to each edge feature, as the latter carries more of the pertinent physical information. This construction of loss is permutation invariant on the nodes.

6.2.2 Network Architecture and Training

Whilst it is true that a thorough implementation of a neural network requires a carefully determined set of optimised hyperparameters, as this chapter is a proof of principle analysis an extensive scan is not carried out here. That said, given how critical the latent dimension is for autoencoders, a scan over the latent dimension is performed, and detailed in the next section. The first layer of the encoder uses an MLP of hidden dimensions 256, 128, 64, and 32 for the edge function that maps the three dimensional edge features to a 5 × 128 dimensional output. Each of these hidden layers has a ReLU activation function, with a sigmoid function for the final layer. The capped range of the latter is useful in preventing the weighted sum in the aggregation from being dominated by the outputs of the edge function. To avoid overfitting, each of the hidden layers has a dropout layer with a fraction of 0.2. Once the aggregation is completed, the 128 dimensional output is fed into a sequence of edge convolution layers, with output dimensions of 64, 32, 6, and so the final output is a set of nodes encoded in a six dimensional latent space. The value of six is selected off the back of a scan over different latent dimensions.

The first element of the decoder switches the dimensions of the encoder; 32, 64 and 128. The 128 dimensional vector is then passed separately to the node and edge reconstruction elements, with each of the edge reconstruction elements containing three edge convolution layers of output dimensions 32, 16, and 8. The inner products on the resulting 8 dimensional vector space are calculated to give the reconstructed adjacency matrices. Finally, the losses for the edge and node reconstruction are calculated and combined to give the total loss.

The network is trained with the Adam optimiser [176], initialised with a learning rate of 0.001, on mini batches of 64 samples. This learning rate is decayed by a factor of 0.5 when the loss has not fallen for five epochs, with a following five epoch cool down phase, and training terminated when the learning rate falls below 10^{-8}. A total of 85000 QCD jets are used to train the network, with a separate validation sample of 28000 jets, and the epoch with the minimum validation loss used in further analyses.

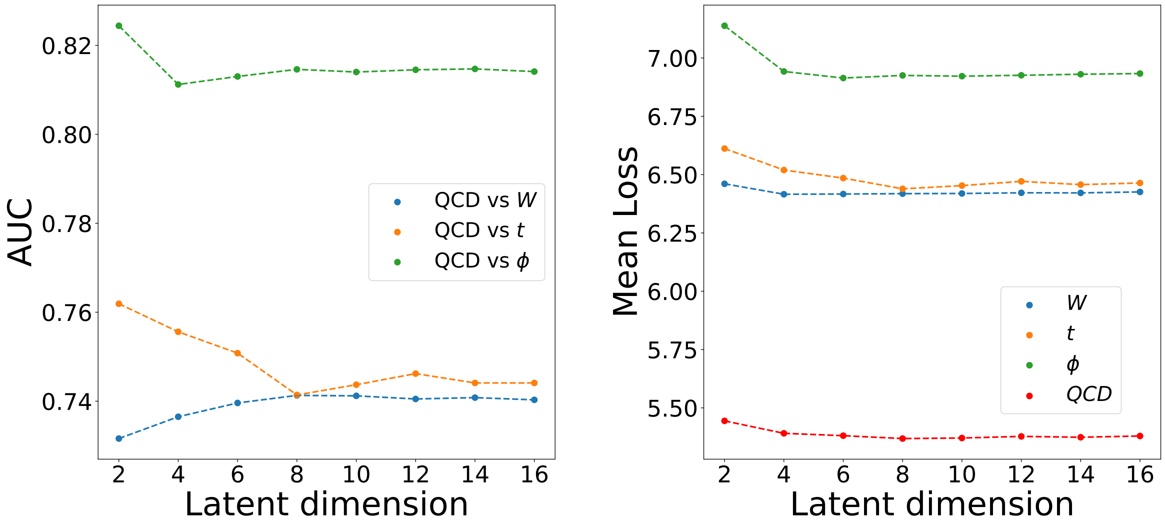

(a)

(b)

Figure 6.4: The AUC and mean loss for the three signal classes as a function of latent dimension from two to sixteen for the given architecture

6.3 Results and Discussion

The test dataset comprises a further 28000 QCD jets, as yet unseen by the network, and the same number of jets for each of the three different signal classes. The first task is to fix the number of latent dimensions, by performing a scan between two to sixteen in even steps with all other hyperparameters fixed. The area under the curve (AUC) between the signal acceptance and background rejection for each latent dimension is shown in Fig. 6.4(a), while the mean loss for each class for each latent dimension is shown in Fig. 6.4(b). Whilst the mean loss is consistent and stable for QCD jets beyond the dimension four mark, there remains some notable variation between the different signal scenarios, which can be ascribed to the unsupervised setup used here, as this means the network knows nothing about the signal classes.

This does allow us to gain an insight into the network behaviour for the differing signal classes in the context of differing latent dimensions. The fact that the AUC increases with the latent dimension for the two pronged W jets signifies that the network treats them similarly to the QCD jets when the latent dimension bottleneck is small. However, the low dimensionality prevents the typical QCD jet features from being accurately modelled, and so the discrimination in this region is unreliable. Increasing the latent dimensions allows the network to more accurately learn the QCD features, yielding robust anomaly detection for top quarks and W bosons. As for the ϕ jets, they have a distinctly different structure to the background QCD jets, so the network can rapidly achieve a stable AUC. On the whole, stable performance is reached for all three classes at a latent dimension of around six, with the mean loss flattening out at this point, and so this is chosen as the number of latent dimensions. It would in theory be possible to attain superior accuracy with different latent dimensions for specific signal classes, but as anomaly detection is the goal, and anomalies are by definition of unknown composition, it would make no sense to tune the network to each individual class.

The normalised distribution of the loss is shown in Fig. 6.5(a) for all classes. As one would expect for a network trained on QCD jets only, the loss is lowest for this class. This is the desired performance of the autoencoder, as it means that vetoing jets with low loss should leave a signal dataset rich in anomalies. The ROC curve and the corresponding AUC values are shown in Fig. 6.5(b), from which it can be seen that the network performs better for the more complex prong structures. Comparisons with other autoencoders [481] and correlations of the loss with common jet observables are available in the appendices of Ref. [2].

Following similar work done in a range of physical scenarios in Refs. [490–492], the capacity for

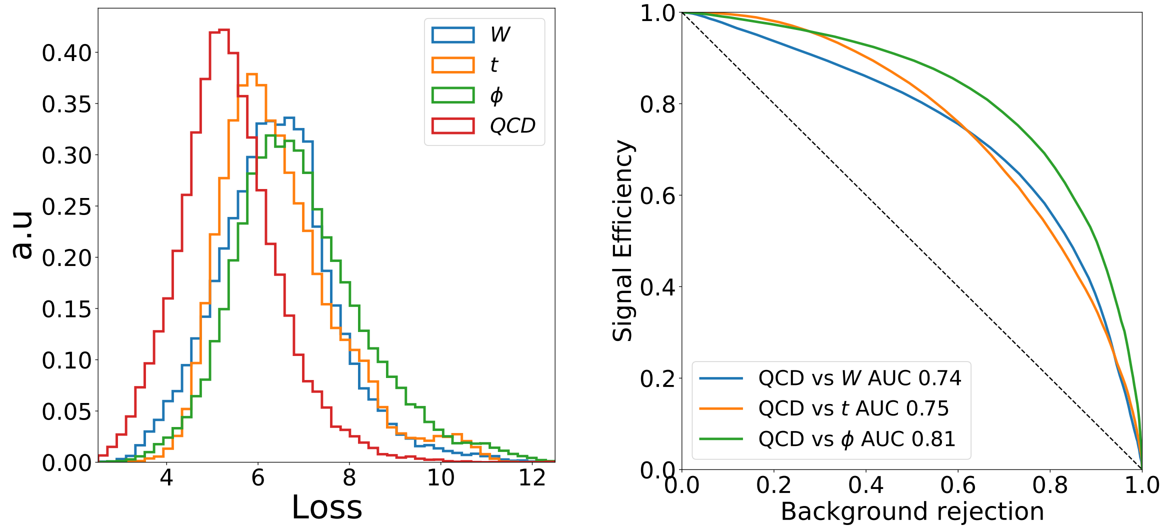

(a)

(b)

Figure 6.5: The loss of the graph-autoencoder (a) and ROC curves (b) for a network trained only on QCD jets.

the autoencoder to effectively compress the QCD jets into the latent space representations is explored, as the autoencoder should learn the graph structure through the edge reconstruction network. This is done using a graph readout operation that takes the mean in each dimension of the latent node features, yielding a latent graph representation of fixed dimensions. For a vector index a, node index i and a set of graph nodes G, this is given by

$$\tilde{f}^a = \frac{1}{N} \sum_{i \in G} f_i^a \,.$$

The resulting normalised distributions for each of the classes in each of the latent dimensions and the corresponding AUC when discriminating against the QCD background are shown in Fig. 6.6 and Fig. 6.7. From these plots, it can be seen that $\tilde{f}^2$ gives the optimal performance for the top and ϕ jet cases, with $\tilde{f}^5$ performing best for the W jets. For the BSM scalar and the W jets, the maximal AUCs of 0.84 and 0.78 respectively represent improvements over the values found from the more standard loss function, which are given in Fig. 6.5(b). However, the latent distributions lack regularisation terms in their loss function, which leaves them susceptible to training uncertainties, which is to say that the distributions can present very differently for different training instances, even if the loss function distributions are very similar. It is possible to overcome this issue for the training class [493–495], but the very nature of unsupervised training means it is not possible to control the signal distributions in this way.

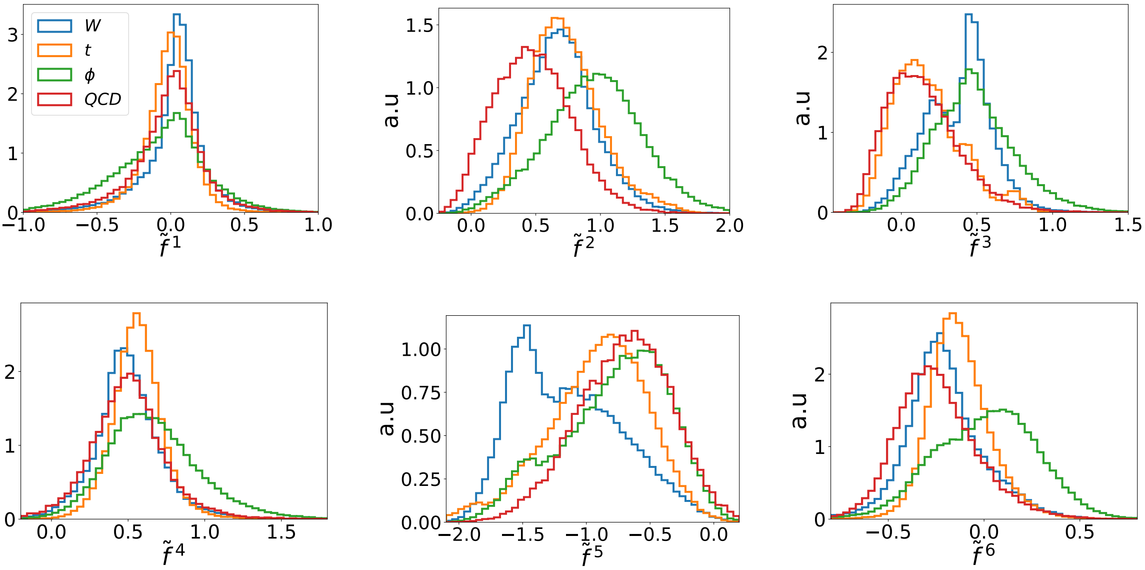

Figure 6.6: The distribution of six dimensional latent space after the training is performed only on QCD jets.

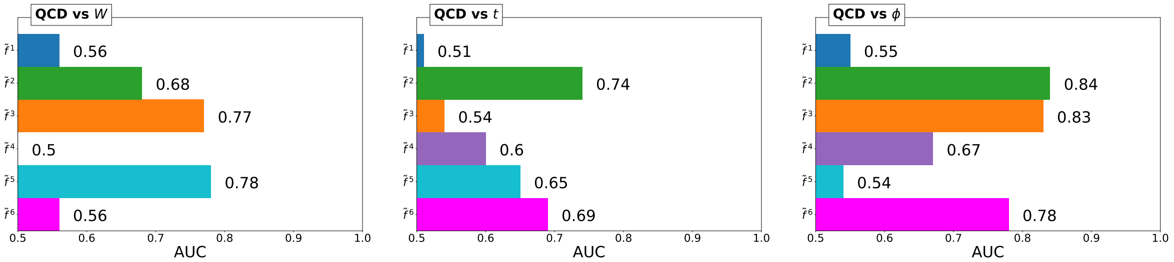

Figure 6.7: The AUC for all three signal classes corresponding to each latent dimension in the network.

6.4 Conclusions

This chapter has focussed on the development of a GNN autoencoder capable of unsupervised anomaly detection in the rich QCD background present at the LHC, as part of the quest to identify any and all possible signatures of BSM physics amongst the maelstrom of collider data. In particular, the graph decoder designed here uses a novel edge reconstruction network, which allows it to reconstruct multidimensional edge information, bestowing upon the autoencoder the ability to classify whole graphs, which is a step beyond previously designed graph based autoencoders. By making use of both multidimensional edge and node features as inputs, latent space representations of QCD jets' graph structured data can be learnt and anomalous signals picked out by the autoencoder's relative failure in the reconstruction of such jets, resulting in higher total loss values than for the QCD jets.

This anomaly finding technique works well in the three scenarios considered here, and the further possibility of directly using the latent space variables for anomaly detection has also been explored, and can indeed prove a powerful tool through the ability to access compressed information in the QCD data. The latent dimension approach also has the appealing characteristic of requiring far fewer layers than the loss based approach, leading to a shallower network and the associated benefits in terms of training time. As such, further study of the latent dimension representation of QCD jets as an avenue for NP detection by anomaly identification is warranted, and may represent a step towards concrete detection of BSM physics. That said, here the QCD theory and the systematic uncertainties have not been addressed, and tackling these should be the immediate focus of future work.

This anomaly detection method provides a further step towards generality in the search for NP at the LHC, as it is truly independent of the nature of the NP. This opens up a wealth of possibilities in the event detection sphere and frees experiments from the constraints of model dependent searches. Hopefully, in the years to come, anomalies will not only be found in the data, but in time they will be explained and integrated into our understanding of the Universe. Of course, history has shown us that there is always some new anomaly just around the corner, and discoveries can often raise more questions than answers. Part of the power of concentrating on the detection of a generic anomaly is the evergreen nature of anomalies – something new and mysterious may always be hiding in the data, no matter the level of understanding we think we have.

Chapter 7

Conclusion

And so we arrive, here at the end of all things, or at least the end of this thesis. The prevailing model of particle physics, the SM, is a towering success and a testament to human ingenuity, but it simply is not complete. Indeed, things have become perhaps a little stale in the past decade since the confirmation of the existence of the Higgs boson at the LHC in 2012. On the one hand, many, many measurements seem determined to conform to the SM predictions, and yet there are some hints, some anomalies, a few tentative signs of the hand of NP amongst the vast reams of collider data and so the search must continue. Lest this enterprise of great pith and moment turn awry, particle physics phenomenology at the LHC and beyond must be studied.

This challenge has been approached from a few angles over the course of my studies in the past few years, evolving into this concrete record. After establishing the fundamentals of the SM and its issues in Chapter 2, a relatively simple model of NP in the Higgs sector was introduced in Chapter 3. This two singlet model was examined in the context of its Higgs bosons decaying in a cascade pattern and the resulting interference effects in the top sector, finding that these interference effects are largely absent for the asymmetric cascade decay. This means that, when the branching ratios are favourable, the detection possibilities are not diminished by signal-background interference. The sensitivity can be further enhanced by deploying machine learning techniques.

A large portion of the thesis is Chapter 4, which comprises a thorough and detailed examination of another BSM model in the Higgs sector; the 2HDM, and its four naturally flavour conserving types. Bringing together the plethora of measurements across all sorts of sectors, including conditions of a cosmological bent, it is possible to place the tightest constraints yet on the parameter space of this model. In doing so, the allowed regions for the 2HDM are squeezed harder and the energy thresholds pushed higher than in any previous studies, driving the model toward the alignment limit and allowed particle masses close to the TeV level.

Sadly, no concrete detection of BSM physics has yet occurred. It is prudent then to turn to other, more general approaches to constraining NP, hence the development and deployment of the EFT framework. Applying the nascent field of machine learning, and GNNs in particular, to EFT studies was done in Chapter 5, demonstrating the boost in constraining power that can be achieved through this method.

Further cranking the machine learning handle, a GNN based autoencoder was designed in Chapter 6 with the goal of picking out anomalous signals in the LHC data. This approach was ultimately successful and points the way for increased generality in BSM searches, both using the autoencoder and the latent space variables it provides.

As Banquo beseeched the three witches, if you can look into the seeds of time, and say which grain will grow and which will not, speak then. The path to progress is uncertain, and nobody can say where the final blow to the SM will fall. In anticipation of this next breakthrough, this thesis has explored numerous avenues for beyond standard model physics and how it may present at the LHC and future colliders.

Bibliography

[1] O. Atkinson, C. Englert and P. Stylianou, *On interference effects in top-philic decay chains*, *Phys. Lett. B* **821** (2021) 136618, [`2012.07424`].

[2] O. Atkinson, A. Bhardwaj, C. Englert, V. S. Ngairangbam and M. Spannowsky, *Anomaly detection with convolutional Graph Neural Networks*, *JHEP* **08** (2021) 080, [`2105.07988`].

[3] O. Atkinson, M. Black, A. Lenz, A. Rusov and J. Wynne, *Cornering the Two Higgs Doublet Model Type II*, *JHEP* **04** (2022) 172, [`2107.05650`].

[4] O. Atkinson, A. Bhardwaj, S. Brown, C. Englert, D. J. Miller and P. Stylianou, *Improved constraints on effective top quark interactions using edge convolution networks*, *JHEP* **04** (2022) 137, [`2111.01838`].

[5] O. Atkinson, M. Black, C. Englert, A. Lenz, A. Rusov and J. Wynne, *The flavourful present and future of 2HDMs at the collider energy frontier*, *JHEP* **11** (2022) 139, [`2202.08807`].

[6] O. Atkinson, A. Bhardwaj, C. Englert, P. Konar, V. S. Ngairangbam and M. Spannowsky, *IRC-Safe Graph Autoencoder for Unsupervised Anomaly Detection*, *Front. Artif. Intell.* **5** (2022) 943135, [`2204.12231`].

[7] O. Atkinson, M. Black, C. Englert, A. Lenz and A. Rusov, *MUonE, muon g-2 and electroweak precision constraints within 2HDMs*, *Phys. Rev. D* **106** (2022) 115031, [`2207.02789`].

[8] Anisha, O. Atkinson, A. Bhardwaj, C. Englert and P. Stylianou, *Quartic Gauge-Higgs couplings: constraints and future directions*, *JHEP* **10** (2022) 172, [`2208.09334`].

[9] Anisha, O. Atkinson, A. Bhardwaj, C. Englert, W. Naskar and P. Stylianou, *BSM reach of four-top production at the LHC*, *Phys. Rev. D* **108** (2023) 035001, [`2302.08281`].

[10] M. D. Schwartz, *Quantum Field Theory and the Standard Model*. Cambridge University Press, 3, 2014.

[11] C.-N. Yang and R. L. Mills, *Conservation of Isotopic Spin and Isotopic Gauge Invariance*, *Phys. Rev.* **96** (1954) 191–195.

[12] G. 't Hooft, *Renormalizable Lagrangians for Massive Yang-Mills Fields*, *Nucl. Phys. B* **35** (1971) 167–188.

[13] G. 't Hooft and M. J. G. Veltman, *Regularization and Renormalization of Gauge Fields*, *Nucl. Phys. B* **44** (1972) 189–213.

[14] M. Gell-Mann, *A Schematic Model of Baryons and Mesons*, *Phys. Lett.* **8** (1964) 214–215.

[15] W. A. Bardeen, H. Fritzsch and M. Gell-Mann, *Light cone current algebra, π^0 decay, and e^+e^- annihilation*, in *Topical Meeting on the Outlook for Broken Conformal Symmetry in Elementary Particle Physics*, 7, 1972. `hep-ph/0211388`.

[16] H. Fritzsch, M. Gell-Mann and H. Leutwyler, *Advantages of the Color Octet Gluon Picture*, *Phys. Lett. B* **47** (1973) 365–368.

[17] C. S. Wu, E. Ambler, R. W. Hayward, D. D. Hoppes and R. P. Hudson, *Experimental Test of Parity Conservation in β Decay*, *Phys. Rev.* **105** (1957) 1413–1414.

[18] S. L. Glashow, *Partial Symmetries of Weak Interactions*, *Nucl. Phys.* **22** (1961) 579–588.

[19] S. Weinberg, *A Model of Leptons*, *Phys. Rev. Lett.* **19** (1967) 1264–1266.

[20] A. Salam, *Weak and Electromagnetic Interactions*, *Conf. Proc. C* **680519** (1968) 367–377.

[21] P. W. Higgs, *Broken Symmetries and the Masses of Gauge Bosons*, *Phys. Rev. Lett.* **13** (1964) 508–509.

[22] F. Englert and R. Brout, *Broken Symmetry and the Mass of Gauge Vector Mesons*, *Phys. Rev. Lett.* **13** (1964) 321–323.

[23] G. S. Guralnik, C. R. Hagen and T. W. B. Kibble, *Global Conservation Laws and Massless Particles*, *Phys. Rev. Lett.* **13** (1964) 585–587.

[24] T. W. B. Kibble, *Symmetry breaking in nonAbelian gauge theories*, *Phys. Rev.* **155** (1967) 1554–1561.

[25] T. Nakano and K. Nishijima, *Charge Independence for V-particles*, *Prog. Theor. Phys.* **10** (1953) 581–582.

[26] M. Gell-Mann, *The interpretation of the new particles as displaced charge multiplets*, *Nuovo Cim.* **4** (1956) 848–866.

[27] ATLAS collaboration, G. Aad et al., *Observation of a new particle in the search for the Standard Model Higgs boson with the ATLAS detector at the LHC*, *Phys. Lett. B* **716** (2012) 1–29, [`1207.7214`].

[28] CMS collaboration, S. Chatrchyan et al., *Observation of a New Boson at a Mass of 125 GeV with the CMS Experiment at the LHC*, *Phys. Lett. B* **716** (2012) 30–61, [`1207.7235`].

[29] H. Yukawa, *On the Interaction of Elementary Particles I*, *Proc. Phys. Math. Soc. Jap.* **17** (1935) 48–57.

[30] N. Cabibbo, *Unitary Symmetry and Leptonic Decays*, *Phys. Rev. Lett.* **10** (1963) 531–533.

[31] M. Kobayashi and T. Maskawa, *CP Violation in the Renormalizable Theory of Weak Interaction*, *Prog. Theor. Phys.* **49** (1973) 652–657.

[32] L. Wolfenstein, *Parametrization of the Kobayashi-Maskawa Matrix*, *Phys. Rev. Lett.* **51** (1983) 1945.

[33] J. F. Gunion, H. E. Haber, G. L. Kane and S. Dawson, *The Higgs Hunter's Guide*, vol. 80. 2000.

[34] LHC Higgs Cross Section Working Group collaboration, D. de Florian et al., *Handbook of LHC Higgs Cross Sections: 4. Deciphering the Nature of the Higgs Sector*, `1610.07922`.

[35] LHC Higgs Cross Section Working Group collaboration, J. R. Andersen et al., *Handbook of LHC Higgs Cross Sections: 3. Higgs Properties*, `1307.1347`.

[36] S. D. Ellis and D. E. Soper, *Successive combination jet algorithm for hadron collisions*, *Phys. Rev. D* **48** (1993) 3160–3166, [`hep-ph/9305266`].

[37] M. Cacciari, G. P. Salam and G. Soyez, *The anti-k_t jet clustering algorithm*, *JHEP* **04** (2008) 063, [`0802.1189`].

[38] M. Wobisch and T. Wengler, *Hadronization corrections to jet cross-sections in deep inelastic scattering*, in *Workshop on Monte Carlo Generators for HERA Physics (Plenary Starting Meeting)*, pp. 270–279, 4, 1998. `hep-ph/9907280`.

[39] J. M. Butterworth, A. R. Davison, M. Rubin and G. P. Salam, *Jet substructure as a new Higgs search channel at the LHC*, *Phys. Rev. Lett.* **100** (2008) 242001, [`0802.2470`].

[40] G. P. Salam, *Towards Jetography*, *Eur. Phys. J. C* **67** (2010) 637–686, [`0906.1833`].

[41] A. J. Larkoski, I. Moult and B. Nachman, *Jet Substructure at the Large Hadron Collider: A Review of Recent Advances in Theory and Machine Learning*, *Phys. Rept.* **841** (2020) 1–63, [`1709.04464`].

[42] S. Marzani, G. Soyez and M. Spannowsky, *Looking inside jets: an introduction to jet substructure and boosted-object phenomenology*, vol. 958. Springer, 2019, 10.1007/978-3-030-15709-8.

[43] LSND collaboration, C. Athanassopoulos et al., *Evidence for $\nu_\mu \rightarrow \nu_e$ neutrino oscillations from LSND*, *Phys. Rev. Lett.* **81** (1998) 1774–1777, [`nucl-ex/9709006`].

[44] SUPER-KAMIOKANDE collaboration, Y. Fukuda et al., *Evidence for oscillation of atmospheric neutrinos*, *Phys. Rev. Lett.* **81** (1998) 1562–1567, [`hep-ex/9807003`].

[45] LSND collaboration, A. Aguilar et al., *Evidence for neutrino oscillations from the observation of $\bar{\nu}_e$ appearance in a $\bar{\nu}_\mu$ beam*, *Phys. Rev. D* **64** (2001) 112007, [`hep-ex/0104049`].

[46] KAMLAND collaboration, T. Araki et al., *Measurement of neutrino oscillation with KamLAND: Evidence of spectral distortion*, *Phys. Rev. Lett.* **94** (2005) 081801, [`hep-ex/0406035`].

[47] SUPER-KAMIOKANDE collaboration, Y. Ashie et al., *Evidence for an oscillatory signature in atmospheric neutrino oscillation*, *Phys. Rev. Lett.* **93** (2004) 101801, [`hep-ex/0404034`].

[48] K2K collaboration, M. H. Ahn et al., *Measurement of Neutrino Oscillation by the K2K Experiment*, *Phys. Rev. D* **74** (2006) 072003, [`hep-ex/0606032`].

[49] SUPER-KAMIOKANDE collaboration, K. Abe et al., *Solar neutrino results in Super-Kamiokande-III*, *Phys. Rev. D* **83** (2011) 052010, [`1010.0118`].

[50] T2K collaboration, K. Abe et al., *Observation of Electron Neutrino Appearance in a Muon Neutrino Beam*, *Phys. Rev. Lett.* **112** (2014) 061802, [`1311.4750`].

[51] T2K collaboration, K. Abe et al., *Measurements of neutrino oscillation in appearance and disappearance channels by the T2K experiment with 6.6×10^{20} protons on target*, *Phys. Rev. D* **91** (2015) 072010, [`1502.01550`].

[52] M. C. Gonzalez-Garcia and M. Maltoni, *Phenomenology with Massive Neutrinos*, *Phys. Rept.* **460** (2008) 1–129, [`0704.1800`].

[53] A. D. Sakharov, *Violation of CP Invariance, C asymmetry, and baryon asymmetry of the universe*, *Pisma Zh. Eksp. Teor. Fiz.* **5** (1967) 32–35.

[54] D. E. Morrissey and M. J. Ramsey-Musolf, *Electroweak baryogenesis*, *New J. Phys.* **14** (2012) 125003, [`1206.2942`].

[55] F. R. Klinkhamer and N. S. Manton, *A Saddle Point Solution in the Weinberg-Salam Theory*, *Phys. Rev. D* **30** (1984) 2212.

[56] C. Jarlskog, *Commutator of the Quark Mass Matrices in the Standard Electroweak Model and a Measure of Maximal CP Nonconservation*, *Phys. Rev. Lett.* **55** (1985) 1039.

[57] K. Kajantie, M. Laine, K. Rummukainen and M. E. Shaposhnikov, *Is there a hot electroweak phase transition at $m_H \gtrsim m_W$?*, *Phys. Rev. Lett.* **77** (1996) 2887–2890, [`hep-ph/9605288`].

[58] PLANCK collaboration, P. A. R. Ade et al., *Planck 2013 results. I. Overview of products and scientific results*, *Astron. Astrophys.* **571** (2014) A1, [`1303.5062`].

[59] V. C. Rubin and W. K. Ford, Jr., *Rotation of the Andromeda Nebula from a Spectroscopic Survey of Emission Regions*, *Astrophys. J.* **159** (1970) 379–403.

[60] V. C. Rubin, N. Thonnard and W. K. Ford, Jr., *Rotational properties of 21 SC galaxies with a large range of luminosities and radii, from NGC 4605 /R = 4kpc/ to UGC 2885 /R = 122 kpc/*, *Astrophys. J.* **238** (1980) 471.

[61] V. Trimble, *Existence and Nature of Dark Matter in the Universe*, *Ann. Rev. Astron. Astrophys.* **25** (1987) 425–472.

[62] A. Refregier, *Weak gravitational lensing by large scale structure*, *Ann. Rev. Astron. Astrophys.* **41** (2003) 645–668, [`astro-ph/0307212`].

[63] J. A. Tyson, G. P. Kochanski and I. P. Dell'Antonio, *Detailed mass map of CL0024+1654 from strong lensing*, *Astrophys. J. Lett.* **498** (1998) L107, [`astro-ph/9801193`].

[64] A. D. Lewis, D. A. Buote and J. T. Stocke, *Chandra observations of Abell 2029: The Dark matter profile at* < 0.01 *R(VIR) in an unusually relaxed cluster*, *Astrophys. J.* **586** (2003) 135–142, [`astro-ph/0209205`].

[65] D. Clowe, M. Bradac, A. H. Gonzalez, M. Markevitch, S. W. Randall, C. Jones et al., *A direct empirical proof of the existence of dark matter*, *Astrophys. J. Lett.* **648** (2006) L109–L113, [`astro-ph/0608407`].

[66] S. W. Allen, A. C. Fabian, R. W. Schmidt and H. Ebeling, *Cosmological constraints from the local x-ray luminosity function of the most x-ray luminous galaxy clusters*, *Mon. Not. Roy. Astron. Soc.* **342** (2003) 287, [`astro-ph/0208394`].

[67] P. Salucci, *The distribution of dark matter in galaxies*, *Astron. Astrophys. Rev.* **27** (2019) 2, [`1811.08843`].

[68] J. D. Simon, *The Faintest Dwarf Galaxies*, *Ann. Rev. Astron. Astrophys.* **57** (2019) 375–415, [`1901.05465`].

[69] S. W. Allen, A. E. Evrard and A. B. Mantz, *Cosmological Parameters from Observations of Galaxy Clusters*, *Ann. Rev. Astron. Astrophys.* **49** (2011) 409–470, [`1103.4829`].

[70] G. Bertone, D. Hooper and J. Silk, *Particle dark matter: Evidence, candidates and constraints*, *Phys. Rept.* **405** (2005) 279–390, [`hep-ph/0404175`].

[71] J. L. Feng, *Dark Matter Candidates from Particle Physics and Methods of Detection*, *Ann. Rev. Astron. Astrophys.* **48** (2010) 495–545, [`1003.0904`].

[72] SUPERNOVA SEARCH TEAM collaboration, A. G. Riess et al., *Observational evidence from supernovae for an accelerating universe and a cosmological constant*, *Astron. J.* **116** (1998) 1009–1038, [`astro-ph/9805201`].

[73] SUPERNOVA COSMOLOGY PROJECT collaboration, S. Perlmutter et al., *Measurements of* Ω *and* Λ *from 42 high redshift supernovae*, *Astrophys. J.* **517** (1999) 565–586, [`astro-ph/9812133`].

[74] P. A. M. Dirac, *The quantum theory of the electron*, *Proc. Roy. Soc. Lond. A* **117** (1928) 610–624.

[75] Muon g-2 collaboration, B. Abi et al., *Measurement of the Positive Muon Anomalous Magnetic Moment to 0.46 ppm*, *Phys. Rev. Lett.* **126** (2021) 141801, [`2104.03281`].

[76] Muon g-2 collaboration, G. W. Bennett et al., *Final Report of the Muon E821 Anomalous Magnetic Moment Measurement at BNL*, *Phys. Rev. D* **73** (2006) 072003, [`hep-ex/0602035`].

[77] T. Aoyama et al., *The anomalous magnetic moment of the muon in the Standard Model*, *Phys. Rept.* **887** (2020) 1–166, [`2006.04822`].

[78] T. Aoyama, M. Hayakawa, T. Kinoshita and M. Nio, *Complete Tenth-Order QED Contribution to the Muon g-2*, *Phys. Rev. Lett.* **109** (2012) 111808, [`1205.5370`].

[79] T. Aoyama, T. Kinoshita and M. Nio, *Theory of the Anomalous Magnetic Moment of the Electron*, *Atoms* **7** (2019) 28.

[80] A. Czarnecki, W. J. Marciano and A. Vainshtein, *Refinements in electroweak contributions to the muon anomalous magnetic moment*, *Phys. Rev. D* **67** (2003) 073006, [`hep-ph/0212229`].

[81] C. Gnendiger, D. Stöckinger and H. Stöckinger-Kim, *The electroweak contributions to* $(g-2)_\mu$ *after the Higgs boson mass measurement*, *Phys. Rev. D* **88** (2013) 053005, [`1306.5546`].

[82] M. Davier, A. Hoecker, B. Malaescu and Z. Zhang, *Reevaluation of the hadronic vacuum polarisation contributions to the Standard Model predictions of the muon* $g-2$ *and* $\alpha(m_Z^2)$ *using newest hadronic cross-section data*, *Eur. Phys. J. C* **77** (2017) 827, [`1706.09436`].

[83] A. Keshavarzi, D. Nomura and T. Teubner, *Muon* $g-2$ *and* $\alpha(M_Z^2)$*: a new data-based analysis*, *Phys. Rev. D* **97** (2018) 114025, [`1802.02995`].

[84] G. Colangelo, M. Hoferichter and P. Stoffer, *Two-pion contribution to hadronic vacuum polarization*, *JHEP* **02** (2019) 006, [`1810.00007`].

[85] M. Hoferichter, B.-L. Hoid and B. Kubis, *Three-pion contribution to hadronic vacuum polarization*, *JHEP* **08** (2019) 137, [`1907.01556`].

[86] M. Davier, A. Hoecker, B. Malaescu and Z. Zhang, *A new evaluation of the hadronic vacuum polarisation contributions to the muon anomalous magnetic moment and to* $\boldsymbol{\alpha}(\mathbf{m}_{\mathbf{Z}}^{\mathbf{2}})$, *Eur. Phys. J. C* **80** (2020) 241, [`1908.00921`].

[87] A. Keshavarzi, D. Nomura and T. Teubner, $g-2$ *of charged leptons,* $\alpha(M_Z^2)$ *, and the hyperfine splitting of muonium*, *Phys. Rev. D* **101** (2020) 014029, [`1911.00367`].

[88] A. Kurz, T. Liu, P. Marquard and M. Steinhauser, *Hadronic contribution to the muon anomalous magnetic moment to next-to-next-to-leading order*, *Phys. Lett. B* **734** (2014) 144–147, [`1403.6400`].

[89] K. Melnikov and A. Vainshtein, *Hadronic light-by-light scattering contribution to the muon anomalous magnetic moment revisited*, *Phys. Rev. D* **70** (2004) 113006, [`hep-ph/0312226`].

[90] P. Masjuan and P. Sanchez-Puertas, *Pseudoscalar-pole contribution to the* $(g_\mu - 2)$*: a rational approach*, *Phys. Rev. D* **95** (2017) 054026, [`1701.05829`].

[91] G. Colangelo, M. Hoferichter, M. Procura and P. Stoffer, *Dispersion relation for hadronic light-by-light scattering: two-pion contributions*, *JHEP* **04** (2017) 161, [`1702.07347`].

[92] M. Hoferichter, B.-L. Hoid, B. Kubis, S. Leupold and S. P. Schneider, *Dispersion relation for hadronic light-by-light scattering: pion pole*, *JHEP* **10** (2018) 141, [`1808.04823`].

[93] A. Gérardin, H. B. Meyer and A. Nyffeler, *Lattice calculation of the pion transition form factor with* $N_f = 2+1$ *Wilson quarks*, *Phys. Rev. D* **100** (2019) 034520, [`1903.09471`].

[94] J. Bijnens, N. Hermansson-Truedsson and A. Rodríguez-Sánchez, *Short-distance constraints for the HLbL contribution to the muon anomalous magnetic moment*, *Phys. Lett. B* **798** (2019) 134994, [`1908.03331`].

[95] G. Colangelo, F. Hagelstein, M. Hoferichter, L. Laub and P. Stoffer, *Longitudinal short-distance constraints for the hadronic light-by-light contribution to* $(g-2)_\mu$ *with large-*N_c *Regge models*, *JHEP* **03** (2020) 101, [`1910.13432`].

[96] T. Blum, N. Christ, M. Hayakawa, T. Izubuchi, L. Jin, C. Jung et al., *Hadronic Light-by-Light Scattering Contribution to the Muon Anomalous Magnetic Moment from Lattice QCD*, *Phys. Rev. Lett.* **124** (2020) 132002, [`1911.08123`].

[97] G. Colangelo, M. Hoferichter, A. Nyffeler, M. Passera and P. Stoffer, *Remarks on*

higher-order hadronic corrections to the muon $g-2$, *Phys. Lett. B* **735** (2014) 90–91, [1403.7512].

[98] S. Borsanyi et al., *Leading hadronic contribution to the muon magnetic moment from lattice QCD*, *Nature* **593** (2021) 51–55, [2002.12347].

[99] Fermilab Lattice, LATTICE-HPQCD, MILC collaboration, B. Chakraborty et al., *Strong-Isospin-Breaking Correction to the Muon Anomalous Magnetic Moment from Lattice QCD at the Physical Point*, *Phys. Rev. Lett.* **120** (2018) 152001, [1710.11212].

[100] Budapest-Marseille-Wuppertal collaboration, S. Borsanyi et al., *Hadronic vacuum polarization contribution to the anomalous magnetic moments of leptons from first principles*, *Phys. Rev. Lett.* **121** (2018) 022002, [1711.04980].

[101] RBC, UKQCD collaboration, T. Blum, P. A. Boyle, V. Gülpers, T. Izubuchi, L. Jin, C. Jung et al., *Calculation of the hadronic vacuum polarization contribution to the muon anomalous magnetic moment*, *Phys. Rev. Lett.* **121** (2018) 022003, [1801.07224].

[102] D. Giusti, V. Lubicz, G. Martinelli, F. Sanfilippo and S. Simula, *Electromagnetic and strong isospin-breaking corrections to the muon $g-2$ from Lattice QCD+QED*, *Phys. Rev. D* **99** (2019) 114502, [1901.10462].

[103] PACS collaboration, E. Shintani and Y. Kuramashi, *Hadronic vacuum polarization contribution to the muon $g-2$ with 2+1 flavor lattice QCD on a larger than $(10\ fm)^4$ lattice at the physical point*, *Phys. Rev. D* **100** (2019) 034517, [1902.00885].

[104] Fermilab Lattice, LATTICE-HPQCD, MILC collaboration, C. T. H. Davies et al., *Hadronic-vacuum-polarization contribution to the muon's anomalous magnetic moment from four-flavor lattice QCD*, *Phys. Rev. D* **101** (2020) 034512, [1902.04223].

[105] A. Gérardin, M. Cè, G. von Hippel, B. Hörz, H. B. Meyer, D. Mohler et al., *The leading hadronic contribution to $(g-2)_\mu$ from lattice QCD with $N_\mathrm{f} = 2+1$ flavours of $O(a)$ improved Wilson quarks*, *Phys. Rev. D* **100** (2019) 014510, [1904.03120].

[106] C. Aubin, T. Blum, C. Tu, M. Golterman, C. Jung and S. Peris, *Light quark vacuum polarization at the physical point and contribution to the muon $g-2$*, *Phys. Rev. D* **101** (2020) 014503, [1905.09307].

[107] D. Giusti and S. Simula, *Lepton anomalous magnetic moments in Lattice QCD+QED*, *PoS* **LATTICE2019** (2019) 104, [`1910.03874`].

[108] S. Weinberg, *Phenomenological Lagrangians*, *Physica A* **96** (1979) 327–340.

[109] W. Buchmuller and D. Wyler, *Effective Lagrangian Analysis of New Interactions and Flavor Conservation*, *Nucl. Phys. B* **268** (1986) 621–653.

[110] C. J. C. Burges and H. J. Schnitzer, *Virtual Effects of Excited Quarks as Probes of a Possible New Hadronic Mass Scale*, *Nucl. Phys. B* **228** (1983) 464–500.

[111] C. N. Leung, S. T. Love and S. Rao, *Low-Energy Manifestations of a New Interaction Scale: Operator Analysis*, *Z. Phys. C* **31** (1986) 433.

[112] K. Hagiwara, R. D. Peccei, D. Zeppenfeld and K. Hikasa, *Probing the Weak Boson Sector in $e^+e^- \to W^+W^-$*, *Nucl. Phys. B* **282** (1987) 253–307.

[113] B. Grzadkowski, M. Iskrzynski, M. Misiak and J. Rosiek, *Dimension-Six Terms in the Standard Model Lagrangian*, *JHEP* **10** (2010) 085, [`1008.4884`].

[114] A. Dedes, W. Materkowska, M. Paraskevas, J. Rosiek and K. Suxho, *Feynman rules for the Standard Model Effective Field Theory in R_ξ -gauges*, *JHEP* **06** (2017) 143, [`1704.03888`].

[115] S. Weinberg, *Baryon and Lepton Nonconserving Processes*, *Phys. Rev. Lett.* **43** (1979) 1566–1570.

[116] I. Brivio and M. Trott, *The Standard Model as an Effective Field Theory*, *Phys. Rept.* **793** (2019) 1–98, [`1706.08945`].

[117] K. J. F. Gaemers and F. Hoogeveen, *Higgs Production and Decay Into Heavy Flavors With the Gluon Fusion Mechanism*, *Phys. Lett. B* **146** (1984) 347–349.

[118] D. Dicus, A. Stange and S. Willenbrock, *Higgs decay to top quarks at hadron colliders*, *Phys. Lett. B* **333** (1994) 126–131, [`hep-ph/9404359`].

[119] W. Bernreuther, A. Brandenburg and M. Flesch, *Effects of Higgs sector CP violation in top quark pair production at the LHC*, `hep-ph/9812387`.

[120] S. Jung, J. Song and Y. W. Yoon, *Dip or nothingness of a Higgs resonance from the interference with a complex phase*, *Phys. Rev. D* **92** (2015) 055009, [`1505.00291`].

[121] R. Frederix and F. Maltoni, *Top pair invariant mass distribution: A Window on new physics*, *JHEP* **01** (2009) 047, [`0712.2355`].

[122] V. Barger, T. Han and D. G. E. Walker, *Top Quark Pairs at High Invariant Mass: A Model-Independent Discriminator of New Physics at the LHC*, *Phys. Rev. Lett.* **100** (2008) 031801, [`hep-ph/0612016`].

[123] N. Craig, F. D'Eramo, P. Draper, S. Thomas and H. Zhang, *The Hunt for the Rest of the Higgs Bosons*, *JHEP* **06** (2015) 137, [`1504.04630`].

[124] W. Bernreuther, P. Galler, C. Mellein, Z. G. Si and P. Uwer, *Production of heavy Higgs bosons and decay into top quarks at the LHC*, *Phys. Rev. D* **93** (2016) 034032, [`1511.05584`].

[125] M. Carena and Z. Liu, *Challenges and opportunities for heavy scalar searches in the $t\bar{t}$ channel at the LHC*, *JHEP* **11** (2016) 159, [`1608.07282`].

[126] B. Hespel, F. Maltoni and E. Vryonidou, *Signal background interference effects in heavy scalar production and decay to a top-anti-top pair*, *JHEP* **10** (2016) 016, [`1606.04149`].

[127] D. Buarque Franzosi, F. Fabbri and S. Schumann, *Constraining scalar resonances with top-quark pair production at the LHC*, *JHEP* **03** (2018) 022, [`1711.00102`].

[128] D. Buarque Franzosi, E. Vryonidou and C. Zhang, *Scalar production and decay to top quarks including interference effects at NLO in QCD in an EFT approach*, *JHEP* **10** (2017) 096, [`1707.06760`].

[129] A. Djouadi, J. Ellis, A. Popov and J. Quevillon, *Interference effects in $t\bar{t}$ production at the LHC as a window on new physics*, *JHEP* **03** (2019) 119, [`1901.03417`].

[130] P. Basler, S. Dawson, C. Englert and M. Mühlleitner, *Di-Higgs boson peaks and top valleys: Interference effects in Higgs sector extensions*, *Phys. Rev. D* **101** (2020) 015019, [`1909.09987`].

[131] M. H. Seymour, *The Higgs boson line shape and perturbative unitarity*, *Phys. Lett. B* **354** (1995) 409–414, [`hep-ph/9505211`].

[132] J. Papavassiliou and A. Pilaftsis, *Effective charge of the Higgs boson*, *Phys. Rev. Lett.* **80** (1998) 2785–2788, [`hep-ph/9710380`].

[133] J. Papavassiliou and A. Pilaftsis, *Gauge invariant resummation formalism for two point correlation functions*, *Phys. Rev. D* **54** (1996) 5315–5335, [hep-ph/9605385].

[134] P. Gambino and P. A. Grassi, *The Nielsen identities of the SM and the definition of mass*, *Phys. Rev. D* **62** (2000) 076002, [hep-ph/9907254].

[135] P. A. Grassi, B. A. Kniehl and A. Sirlin, *Width and partial widths of unstable particles in the light of the Nielsen identities*, *Phys. Rev. D* **65** (2002) 085001, [hep-ph/0109228].

[136] S. Goria, G. Passarino and D. Rosco, *The Higgs Boson Lineshape*, *Nucl. Phys. B* **864** (2012) 530–579, [1112.5517].

[137] T. Robens, T. Stefaniak and J. Wittbrodt, *Two-real-scalar-singlet extension of the SM: LHC phenomenology and benchmark scenarios*, *Eur. Phys. J. C* **80** (2020) 151, [1908.08554].

[138] C. Englert, M. Fairbairn, M. Spannowsky, P. Stylianou and S. Varma, *Sensing Higgs boson cascade decays through memory*, *Phys. Rev. D* **102** (2020) 095027, [2008.08611].

[139] ATLAS collaboration, M. Aaboud et al., *Search for Heavy Higgs Bosons A/H Decaying to a Top Quark Pair in pp Collisions at $\sqrt{s} = 8$ TeV with the ATLAS Detector*, *Phys. Rev. Lett.* **119** (2017) 191803, [1707.06025].

[140] CMS collaboration, A. M. Sirunyan et al., *Search for heavy Higgs bosons decaying to a top quark pair in proton-proton collisions at $\sqrt{s} = 13$ TeV*, *JHEP* **04** (2020) 171, [1908.01115].

[141] I. P. Ivanov, *Building and testing models with extended Higgs sectors*, *Prog. Part. Nucl. Phys.* **95** (2017) 160–208, [1702.03776].

[142] R. N. Lerner and J. McDonald, *Gauge singlet scalar as inflaton and thermal relic dark matter*, *Phys. Rev. D* **80** (2009) 123507, [0909.0520].

[143] M. Gonderinger, H. Lim and M. J. Ramsey-Musolf, *Complex Scalar Singlet Dark Matter: Vacuum Stability and Phenomenology*, *Phys. Rev. D* **86** (2012) 043511, [1202.1316].

[144] G. Belanger, K. Kannike, A. Pukhov and M. Raidal, *Z_3 Scalar Singlet Dark Matter*, *JCAP* **01** (2013) 022, [1211.1014].

[145] D. Curtin, P. Meade and C.-T. Yu, *Testing Electroweak Baryogenesis with Future Colliders*, *JHEP* **11** (2014) 127, [1409.0005].

[146] A. V. Kotwal, M. J. Ramsey-Musolf, J. M. No and P. Winslow, *Singlet-catalyzed electroweak phase transitions in the 100 TeV frontier*, *Phys. Rev. D* **94** (2016) 035022, [`1605.06123`].

[147] C.-W. Chiang, M. J. Ramsey-Musolf and E. Senaha, *Standard Model with a Complex Scalar Singlet: Cosmological Implications and Theoretical Considerations*, *Phys. Rev. D* **97** (2018) 015005, [`1707.09960`].

[148] B. Grzadkowski and D. Huang, *Spontaneous CP-Violating Electroweak Baryogenesis and Dark Matter from a Complex Singlet Scalar*, *JHEP* **08** (2018) 135, [`1807.06987`].

[149] W. Cheng and L. Bian, *From inflation to cosmological electroweak phase transition with a complex scalar singlet*, *Phys. Rev. D* **98** (2018) 023524, [`1801.00662`].

[150] P. M. Ferreira, *The vacuum structure of the Higgs complex singlet-doublet model*, *Phys. Rev. D* **94** (2016) 096011, [`1607.06101`].

[151] K. Kannike, *Vacuum Stability Conditions From Copositivity Criteria*, *Eur. Phys. J. C* **72** (2012) 2093, [`1205.3781`].

[152] K. Kannike, *Vacuum Stability of a General Scalar Potential of a Few Fields*, *Eur. Phys. J. C* **76** (2016) 324, [`1603.02680`].

[153] M. E. Peskin and T. Takeuchi, *Estimation of oblique electroweak corrections*, *Phys. Rev. D* **46** (1992) 381–409.

[154] M. E. Peskin and T. Takeuchi, *A New constraint on a strongly interacting Higgs sector*, *Phys. Rev. Lett.* **65** (1990) 964–967.

[155] GFITTER GROUP collaboration, M. Baak, J. Cúth, J. Haller, A. Hoecker, R. Kogler, K. Mönig et al., *The global electroweak fit at NNLO and prospects for the LHC and ILC*, *Eur. Phys. J. C* **74** (2014) 3046, [`1407.3792`].

[156] M. Spira, *HIGLU: A program for the calculation of the total Higgs production cross-section at hadron colliders via gluon fusion including QCD corrections*, `hep-ph/9510347`.

[157] K. Arnold et al., *VBFNLO: A Parton level Monte Carlo for processes with electroweak bosons*, *Comput. Phys. Commun.* **180** (2009) 1661–1670, [`0811.4559`].

[158] J. Baglio et al., *VBFNLO: A Parton Level Monte Carlo for Processes with Electroweak Bosons – Manual for Version 2.7.0*, `1107.4038`.

[159] T. Hahn and M. Perez-Victoria, *Automatized one loop calculations in four-dimensions and D-dimensions*, *Comput. Phys. Commun.* **118** (1999) 153–165, [`hep-ph/9807565`].

[160] T. Hahn, *Loop calculations with FeynArts, FormCalc, and LoopTools*, *Acta Phys. Polon. B* **30** (1999) 3469–3475, [`hep-ph/9910227`].

[161] T. Hahn, *Generating Feynman diagrams and amplitudes with FeynArts 3*, *Comput. Phys. Commun.* **140** (2001) 418–431, [`hep-ph/0012260`].

[162] T. Hahn, *Automatic loop calculations with FeynArts, FormCalc, and LoopTools*, *Nucl. Phys. B Proc. Suppl.* **89** (2000) 231–236, [`hep-ph/0005029`].

[163] T. Hahn and C. Schappacher, *The Implementation of the minimal supersymmetric standard model in FeynArts and FormCalc*, *Comput. Phys. Commun.* **143** (2002) 54–68, [`hep-ph/0105349`].

[164] T. Sjöstrand, S. Ask, J. R. Christiansen, R. Corke, N. Desai, P. Ilten et al., *An introduction to PYTHIA 8.2*, *Comput. Phys. Commun.* **191** (2015) 159–177, [`1410.3012`].

[165] M. Dobbs and J. B. Hansen, *The HepMC C++ Monte Carlo event record for High Energy Physics*, *Comput. Phys. Commun.* **134** (2001) 41–46.

[166] E. Conte, B. Fuks and G. Serret, *MadAnalysis 5, A User-Friendly Framework for Collider Phenomenology*, *Comput. Phys. Commun.* **184** (2013) 222–256, [`1206.1599`].

[167] E. Conte, B. Dumont, B. Fuks and C. Wymant, *Designing and recasting LHC analyses with MadAnalysis 5*, *Eur. Phys. J. C* **74** (2014) 3103, [`1405.3982`].

[168] B. Dumont, B. Fuks, S. Kraml, S. Bein, G. Chalons, E. Conte et al., *Toward a public analysis database for LHC new physics searches using MADANALYSIS 5*, *Eur. Phys. J. C* **75** (2015) 56, [`1407.3278`].

[169] E. Conte and B. Fuks, *Confronting new physics theories to LHC data with MADANALYSIS 5*, *Int. J. Mod. Phys. A* **33** (2018) 1830027, [`1808.00480`].

[170] M. Cacciari, G. P. Salam and G. Soyez, *FastJet User Manual*, *Eur. Phys. J. C* **72** (2012) 1896, [`1111.6097`].

[171] M. Cacciari and G. P. Salam, *Dispelling the N^3 myth for the k_t jet-finder*, *Phys. Lett. B* **641** (2006) 57–61, [`hep-ph/0512210`].

[172] ATLAS collaboration, *Measurement of the b-tag Efficiency in a Sample of Jets Containing Muons with 5 fb^{-1} of Data from the ATLAS Detector*, ATLAS-CONF-2012-043, (2012).

[173] A. Bredenstein, A. Denner, S. Dittmaier and S. Pozzorini, *NLO QCD corrections to $pp \to t\bar{t}b\bar{b} + X$ at the LHC*, *Phys. Rev. Lett.* **103** (2009) 012002, [`0905.0110`].

[174] ATLAS, CMS collaboration, *Addendum to the report on the physics at the HL-LHC, and perspectives for the HE-LHC: Collection of notes from ATLAS and CMS*, *CERN Yellow Rep. Monogr.* **7** (2019) Addendum, [`1902.10229`].

[175] F. Chollet et al., *Keras*, `https://keras.io` (2015).

[176] D P. Kingma and J Ba, *Adam: A Method for Stochastic Optimization*, *CoRR*, [`1412.6980`].

[177] J. S. Bridle, in *Neurocomputing*, edited by F. F. Soulié and J. Hérault (Springer Berlin Heidelberg, Berlin, Heidelberg, 1990), pp. 227–236, ISBN 978-3-642-76153-9.

[178] M. Trodden, *Electroweak baryogenesis: A Brief review*, in *33rd Rencontres de Moriond: Electroweak Interactions and Unified Theories*, pp. 471–480, 1998. `hep-ph/9805252`.

[179] G. C. Dorsch, S. J. Huber, K. Mimasu and J. M. No, *Echoes of the Electroweak Phase Transition: Discovering a second Higgs doublet through $A_0 \to ZH_0$*, *Phys. Rev. Lett.* **113** (2014) 211802, [`1405.5537`].

[180] G. C. Dorsch, S. J. Huber, K. Mimasu and J. M. No, *Hierarchical versus degenerate 2HDM: The LHC run 1 legacy at the onset of run 2*, *Phys. Rev. D* **93** (2016) 115033, [`1601.04545`].

[181] P. Basler, M. Krause, M. Muhlleitner, J. Wittbrodt and A. Wlotzka, *Strong First Order Electroweak Phase Transition in the CP-Conserving 2HDM Revisited*, *JHEP* **02** (2017) 121, [`1612.04086`].

[182] P. Basler, S. Dawson, C. Englert and M. Mühlleitner, *Showcasing HH production: Benchmarks for the LHC and HL-LHC*, *Phys. Rev. D* **99** (2019) 055048, [`1812.03542`].

[183] D. Gonçalves, A. Kaladharan and Y. Wu, *Electroweak phase transition in the 2HDM: Collider and gravitational wave complementarity*, *Phys. Rev. D* **105** (2022) 095041, [`2108.05356`].

[184] W. Su, A. G. Williams and M. Zhang, *Strong first order electroweak phase transition in 2HDM confronting future Z & Higgs factories*, *JHEP* **04** (2021) 219, [`2011.04540`].

[185] L. Wang, *Inflation, electroweak phase transition, and Higgs searches at the LHC in the two-Higgs-doublet model*, *JHEP* **07** (2022) 055, [2105.02143].

[186] G. C. Dorsch, S. J. Huber, K. Mimasu and J. M. No, *The Higgs Vacuum Uplifted: Revisiting the Electroweak Phase Transition with a Second Higgs Doublet*, *JHEP* **12** (2017) 086, [1705.09186].

[187] P. Basler, L. Biermann, M. Mühlleitner and J. Müller, *Electroweak baryogenesis in the CP-violating two-Higgs doublet model*, *Eur. Phys. J. C* **83** (2023) 57, [2108.03580].

[188] Anisha, L. Biermann, C. Englert and M. Mühlleitner, *Two Higgs doublets, effective interactions and a strong first-order electroweak phase transition*, *JHEP* **08** (2022) 091, [2204.06966].

[189] J. F. Gunion, R. Vega and J. Wudka, *Naturalness problems for $\rho = 1$ and other large one loop effects for a standard model Higgs sector containing triplet fields*, *Phys. Rev. D* **43** (1991) 2322–2336.

[190] CMS collaboration, A. M. Sirunyan et al., *Combination of searches for Higgs boson pair production in proton-proton collisions at $\sqrt{s} = 13$ TeV*, *Phys. Rev. Lett.* **122** (2019) 121803, [1811.09689].

[191] ATLAS collaboration, *A combination of measurements of Higgs boson production and decay using up to 139 fb^{-1} of proton–proton collision data at $\sqrt{s} = 13$ TeV collected with the ATLAS experiment*, ATLAS-CONF-2021-053, (2021).

[192] O. Deschamps, S. Descotes-Genon, S. Monteil, V. Niess, S. T'Jampens and V. Tisserand, *The Two Higgs Doublet of Type II facing flavour physics data*, *Phys. Rev. D* **82** (2010) 073012, [0907.5135].

[193] D. Chowdhury and O. Eberhardt, *Update of Global Two-Higgs-Doublet Model Fits*, *JHEP* **05** (2018) 161, [1711.02095].

[194] D. M. Straub, *flavio: a Python package for flavour and precision phenomenology in the Standard Model and beyond*, 1810.08132.

[195] J. Aebischer et al., *WCxf: an exchange format for Wilson coefficients beyond the Standard Model*, *Comput. Phys. Commun.* **232** (2018) 71–83, [1712.05298].

[196] G. C. Branco, P. M. Ferreira, L. Lavoura, M. N. Rebelo, M. Sher and J. P. Silva, *Theory*

and phenomenology of two-Higgs-doublet models, *Phys. Rept.* **516** (2012) 1–102, [1106.0034].

[197] S. L. Glashow and S. Weinberg, *Natural Conservation Laws for Neutral Currents*, *Phys. Rev. D* **15** (1977) 1958–1965.

[198] P. Arnan, D. Bečirević, F. Mescia and O. Sumensari, *Two Higgs doublet models and $b \to s$ exclusive decays*, *Eur. Phys. J. C* **77** (2017) 796, [1703.03426].

[199] X.-F. Han and H.-X. Wang, *Revisiting wrong sign Yukawa coupling of type II two-Higgs-doublet model in light of recent LHC data*, *Chin. Phys. C* **44** (2020) 073101, [2003.06170].

[200] F. Kling, J. M. No and S. Su, *Anatomy of Exotic Higgs Decays in 2HDM*, *JHEP* **09** (2016) 093, [1604.01406].

[201] A. Crivellin, D. Müller and C. Wiegand, *$b \to s\ell^+\ell^-$ transitions in two-Higgs-doublet models*, *JHEP* **06** (2019) 119, [1903.10440].

[202] T. Han, S. Li, S. Su, W. Su and Y. Wu, *Comparative Studies of 2HDMs under the Higgs Boson Precision Measurements*, *JHEP* **01** (2021) 045, [2008.05492].

[203] B. Grinstein, C. W. Murphy and P. Uttayarat, *One-loop corrections to the perturbative unitarity bounds in the CP-conserving two-Higgs doublet model with a softly broken $\mathbb{Z}_2$ symmetry*, *JHEP* **06** (2016) 070, [1512.04567].

[204] V. Cacchio, D. Chowdhury, O. Eberhardt and C. W. Murphy, *Next-to-leading order unitarity fits in Two-Higgs-Doublet models with soft $\mathbb{Z}_2$ breaking*, *JHEP* **11** (2016) 026, [1609.01290].

[205] N. G. Deshpande and E. Ma, *Pattern of Symmetry Breaking with Two Higgs Doublets*, *Phys. Rev. D* **18** (1978) 2574.

[206] A. Barroso, P. M. Ferreira, I. P. Ivanov and R. Santos, *Metastability bounds on the two Higgs doublet model*, *JHEP* **06** (2013) 045, [1303.5098].

[207] I. F. Ginzburg and I. P. Ivanov, *Tree-level unitarity constraints in the most general 2HDM*, *Phys. Rev. D* **72** (2005) 115010, [hep-ph/0508020].

[208] A. Arhrib, *Unitarity constraints on scalar parameters of the standard and two Higgs*

doublets model, in *Workshop on Noncommutative Geometry, Superstrings and Particle Physics*, 12, 2000. `hep-ph/0012353`.

[209] J. Horejsi and M. Kladiva, *Tree-unitarity bounds for THDM Higgs masses revisited*, *Eur. Phys. J. C* **46** (2006) 81–91, [`hep-ph/0510154`].

[210] W. Grimus, L. Lavoura, O. M. Ogreid and P. Osland, *The Oblique parameters in multi-Higgs-doublet models*, *Nucl. Phys. B* **801** (2008) 81–96, [`0802.4353`].

[211] B. Grinstein and M.B Wise, *Operator analysis for precision electroweak physics*, *Phys. Lett. B* **265** (1991) 326–334.

[212] K. Hagiwara, S. Ishihara, R. Szalapski and D. Zeppenfeld, *Low-energy effects of new interactions in the electroweak boson sector*, *Phys. Rev. D* **48** (1993), 2182–2203

[213] Particle Data Group collaboration, P. A. Zyla et al., *Review of Particle Physics*, *PTEP* **2020** (2020) 083C01.

[214] CMS collaboration, A. M. Sirunyan et al., *Combined measurements of Higgs boson couplings in proton–proton collisions at $\sqrt{s} = 13$ TeV*, *Eur. Phys. J. C* **79** (2019) 421, [`1809.10733`].

[215] CMS collaboration, A. M. Sirunyan et al., *A search for the standard model Higgs boson decaying to charm quarks*, *JHEP* **03** (2020) 131, [`1912.01662`].

[216] ATLAS collaboration, G. Aad et al., *Combined measurements of Higgs boson production and decay using up to 80 fb^{-1} of proton-proton collision data at $\sqrt{s} = 13$ TeV collected with the ATLAS experiment*, *Phys. Rev. D* **101** (2020) 012002, [`1909.02845`].

[217] ATLAS collaboration, G. Aad et al., *A search for the $Z\gamma$ decay mode of the Higgs boson in pp collisions at $\sqrt{s} = 13$ TeV with the ATLAS detector*, *Phys. Lett. B* **809** (2020) 135754, [`2005.05382`].

[218] ATLAS collaboration, G. Aad et al., *A search for the dimuon decay of the Standard Model Higgs boson with the ATLAS detector*, *Phys. Lett. B* **812** (2021) 135980, [`2007.07830`].

[219] CMS collaboration, *Combined Higgs boson production and decay measurements with up to 137 fb^{-1} of proton-proton collision data at $\sqrt{s} = 13$ TeV*, CMS-PAS-HIG-19-005, (2021) .

[220] S. Dawson, S. Homiller and S. D. Lane, *Putting standard model EFT fits to work*, *Phys. Rev. D* **102** (2020) 055012, [`2007.01296`].

[221] J. Ellis, C. W. Murphy, V. Sanz and T. You, *Updated Global SMEFT Fit to Higgs, Diboson and Electroweak Data*, *JHEP* **06** (2018) 146, [`1803.03252`].

[222] D. Das, A. Kundu and I. Saha, *Higgs data does not rule out a sequential fourth generation with an extended scalar sector*, *Phys. Rev. D* **97** (2018) 011701, [`1707.03000`].

[223] E. Kuflik, Y. Nir and T. Volansky, *Implications of Higgs searches on the four generation standard model*, *Phys. Rev. Lett.* **110** (2013) 091801, [`1204.1975`].

[224] O. Eberhardt, G. Herbert, H. Lacker, A. Lenz, A. Menzel, U. Nierste et al., *Impact of a Higgs boson at a mass of 126 GeV on the standard model with three and four fermion generations*, *Phys. Rev. Lett.* **109** (2012) 241802, [`1209.1101`].

[225] A. Djouadi and A. Lenz, *Sealing the fate of a fourth generation of fermions*, *Phys. Lett. B* **715** (2012) 310–314, [`1204.1252`].

[226] M. Bertrand, S. Kraml, T. Q. Loc, D. T. Nhung and L. D. Ninh, *Constraining new physics from Higgs measurements with Lilith-2*, *PoS* **TOOLS2020** (2021) 040, [`2012.11408`].

[227] T. Modak, J. C. Romão, S. Sadhukhan, J. a. P. Silva and R. Srivastava, *Constraining wrong-sign hbb couplings with* $h \to \Upsilon\gamma$, *Phys. Rev. D* **94** (2016) 075017, [`1607.07876`].

[228] M. Raju, J. P. Saha, D. Das and A. Kundu, *Double Higgs boson production as an exclusive probe for a sequential fourth generation with wrong-sign Yukawa couplings*, *Phys. Rev. D* **101** (2020) 055036, [`2001.05280`].

[229] CMS collaboration, A. M. Sirunyan et al., *Measurements of Higgs boson production cross sections and couplings in the diphoton decay channel at* $\sqrt{\mathrm{s}} = 13$ *TeV*, *JHEP* **07** (2021) 027, [`2103.06956`].

[230] ATLAS collaboration, *Measurements of gluon fusion and vector-boson-fusion production of the Higgs boson in* $H \to WW^* \to e\nu\mu\nu$ *decays using pp collisions at* $\sqrt{s} = 13$ *TeV with the ATLAS detector*, ATLAS-CONF-2021-014, (2021).

[231] CMS collaboration, A. M. Sirunyan et al., *Evidence for Higgs boson decay to a pair of muons*, *JHEP* **01** (2021) 148, [`2009.04363`].

[232] ATLAS collaboration, G. Aad et al., *Measurements of Higgs bosons decaying to bottom quarks from vector boson fusion production with the ATLAS experiment at* $\sqrt{s} = 13$ *TeV*, *Eur. Phys. J. C* **81** (2021) 537, [`2011.08280`].

[233] ATLAS collaboration, G. Aad et al., *Measurements of WH and ZH production in the $H \to b\bar{b}$ decay channel in pp collisions at 13 TeV with the ATLAS detector*, *Eur. Phys. J. C* **81** (2021) 178, [2007.02873].

[234] HFLAV collaboration, Y. S. Amhis et al., *Averages of b-hadron, c-hadron, and τ-lepton properties as of 2018*, *Eur. Phys. J. C* **81** (2021) 226, [1909.12524].

[235] LHCb collaboration, R. Aaij et al., *Measurement of $|V_{cb}|$ with $B_s^0 \to D_s^{(*)-}\mu^+\nu_\mu$ decays*, *Phys. Rev. D* **101** (2020) 072004, [2001.03225].

[236] LHCb collaboration, R. Aaij et al., *Precise measurement of the f_s/f_d ratio of fragmentation fractions and of B_s^0 decay branching fractions*, *Phys. Rev. D* **104** (2021) 032005, [2103.06810].

[237] E. McLean, C. T. H. Davies, J. Koponen and A. T. Lytle, *$B_s \to D_s\ell\nu$ Form Factors for the full q^2 range from Lattice QCD with non-perturbatively normalized currents*, *Phys. Rev. D* **101** (2020) 074513, [1906.00701].

[238] W. Altmannshofer and P. Stangl, *New physics in rare B decays after Moriond 2021*, *Eur. Phys. J. C* **81** (2021) 952, [2103.13370].

[239] LHCb collaboration, R. Aaij et al., *Differential branching fractions and isospin asymmetries of $B \to K^{(*)}\mu^+\mu^-$ decays*, *JHEP* **06** (2014) 133, [1403.8044].

[240] LHCb collaboration, R. Aaij et al., *Angular Analysis of the $B^+ \to K^{*+}\mu^+\mu^-$ Decay*, *Phys. Rev. Lett.* **126** (2021) 161802, [2012.13241].

[241] LHCb collaboration, R. Aaij et al., *Measurement of CP-Averaged Observables in the $B^0 \to K^{*0}\mu^+\mu^-$ Decay*, *Phys. Rev. Lett.* **125** (2020) 011802, [2003.04831].

[242] ATLAS collaboration, M. Aaboud et al., *Angular analysis of $B_d^0 \to K^*\mu^+\mu^-$ decays in pp collisions at $\sqrt{s} = 8$ TeV with the ATLAS detector*, *JHEP* **10** (2018) 047, [1805.04000].

[243] CMS collaboration, V. Khachatryan et al., *Angular analysis of the decay $B^0 \to K^{*0}\mu^+\mu^-$ from pp collisions at $\sqrt{s} = 8$ TeV*, *Phys. Lett. B* **753** (2016) 424–448, [1507.08126].

[244] CMS collaboration, A. M. Sirunyan et al., *Measurement of angular parameters from the decay $\mathrm{B}^0 \to \mathrm{K}^{*0}\mu^+\mu^-$ in proton-proton collisions at $\sqrt{s} = 8$ TeV*, *Phys. Lett. B* **781** (2018) 517–541, [1710.02846].

[245] BELLE collaboration, S. Choudhury et al., *Test of lepton flavor universality and search for lepton flavor violation in $B \to K\ell\ell$ decays*, *JHEP* **03** (2021) 105, [1908.01848].

[246] BELLE collaboration, A. Abdesselam et al., *Test of Lepton-Flavor Universality in $B \to K^*\ell^+\ell^-$ Decays at Belle*, *Phys. Rev. Lett.* **126** (2021) 161801, [1904.02440].

[247] LHCB collaboration, R. Aaij et al., *Angular analysis and differential branching fraction of the decay $B_s^0 \to \phi\mu^+\mu^-$*, *JHEP* **09** (2015) 179, [1506.08777].

[248] BABAR collaboration, J. P. Lees et al., *Measurement of the $B \to X_s l^+ l^-$ branching fraction and search for direct CP violation from a sum of exclusive final states*, *Phys. Rev. Lett.* **112** (2014) 211802, [1312.5364].

[249] BELLE collaboration, S. Wehle et al., *Lepton-Flavor-Dependent Angular Analysis of $B \to K^*\ell^+\ell^-$*, *Phys. Rev. Lett.* **118** (2017) 111801, [1612.05014].

[250] LHCB collaboration, R. Aaij et al., *Angular analysis of the $B^0 \to K^{*0}e^+e^-$ decay in the low-q^2 region*, *JHEP* **04** (2015) 064, [1501.03038].

[251] CMS collaboration, A. M. Sirunyan et al., *Angular analysis of the decay $B^+ \to K^+\mu^+\mu^-$ in proton-proton collisions at $\sqrt{s} = 8$ TeV*, *Phys. Rev. D* **98** (2018) 112011, [1806.00636].

[252] LHCB collaboration, R. Aaij et al., *Differential branching fraction and angular analysis of $\Lambda_b^0 \to \Lambda\mu^+\mu^-$ decays*, *JHEP* **06** (2015) 115, [1503.07138].

[253] LHCB collaboration, R. Aaij et al., *Angular moments of the decay $\Lambda_b^0 \to \Lambda\mu^+\mu^-$ at low hadronic recoil*, *JHEP* **09** (2018) 146, [1808.00264].

[254] LHCB collaboration, R. Aaij et al., *Test of lepton universality in beauty-quark decays*, *Nature Phys.* **18** (2022) 277–282, [2103.11769].

[255] LHCB collaboration, R. Aaij et al., *Test of lepton universality using $B^+ \to K^+\ell^+\ell^-$ decays*, *Phys. Rev. Lett.* **113** (2014) 151601, [1406.6482].

[256] LHCB collaboration, R. Aaij et al., *Test of lepton universality with $B^0 \to K^{*0}\ell^+\ell^-$ decays*, *JHEP* **08** (2017) 055, [1705.05802].

[257] BABAR collaboration, J. P. Lees et al., *Measurement of Branching Fractions and Rate Asymmetries in the Rare Decays $B \to K^{(*)}l^+l^-$*, *Phys. Rev. D* **86** (2012) 032012, [1204.3933].

[258] F. U. Bernlochner, Z. Ligeti, M. Papucci and D. J. Robinson, *Combined analysis of semileptonic B decays to D and D^*: $R(D^{(*)})$, $|V_{cb}|$, and new physics*, Phys. Rev. D **95** (2017) 115008, [`1703.05330`].

[259] I. Caprini, L. Lellouch and M. Neubert, *Dispersive bounds on the shape of $\bar{B} \to D(*)\ell\bar{\nu}$ form-factors*, Nucl. Phys. B **530** (1998) 153–181, [`hep-ph/9712417`].

[260] Y. Sakaki, M. Tanaka, A. Tayduganov and R. Watanabe, *Testing leptoquark models in $\bar{B} \to D^{(*)}\tau\bar{\nu}$*, Phys. Rev. D **88** (2013) 094012, [`1309.0301`].

[261] A. Bharucha, D. M. Straub and R. Zwicky, *$B \to V\ell^+\ell^-$ in the Standard Model from light-cone sum rules*, JHEP **08** (2016) 098, [`1503.05534`].

[262] N. Gubernari, A. Kokulu and D. van Dyk, *$B \to P$ and $B \to V$ Form Factors from B-Meson Light-Cone Sum Rules beyond Leading Twist*, JHEP **01** (2019) 150, [`1811.00983`].

[263] W. Detmold and S. Meinel, *$\Lambda_b \to \Lambda\ell^+\ell^-$ form factors, differential branching fraction, and angular observables from lattice QCD with relativistic b quarks*, Phys. Rev. D **93** (2016) 074501, [`1602.01399`].

[264] V. Bernard, M. Oertel, E. Passemar and J. Stern, *K(mu3)**L decay: A Stringent test of right-handed quark currents*, Phys. Lett. B **638** (2006) 480–486, [`hep-ph/0603202`].

[265] V. Bernard, M. Oertel, E. Passemar and J. Stern, *Dispersive representation and shape of the K(l3) form factors: Robustness*, Phys. Rev. D **80** (2009) 034034, [`0903.1654`].

[266] FlaviaNet Working Group on Kaon Decays collaboration, M. Antonelli et al., *An Evaluation of $|V_{us}|$ and precise tests of the Standard Model from world data on leptonic and semileptonic kaon decays*, Eur. Phys. J. C **69** (2010) 399–424, [`1005.2323`].

[267] V. Ilisie, *New Barr-Zee contributions to $(\mathbf{g-2})_\mu$ in two-Higgs-doublet models*, JHEP **04** (2015) 077, [`1502.04199`].

[268] F. Borzumati and C. Greub, *2HDMs predictions for $\bar{B} \to X_s\gamma$ in NLO QCD*, Phys. Rev. D **58** (1998) 074004, [`hep-ph/9802391`].

[269] F. Borzumati and C. Greub, *Two Higgs doublet model predictions for $\bar{B} \to X_s\gamma$ in NLO QCD: Addendum*, Phys. Rev. D **59** (1999) 057501, [`hep-ph/9809438`].

[270] A. Crivellin, G. D'Ambrosio and J. Heeck, *Explaining* $h \to \mu^\pm\tau^\mp$, $B \to K^*\mu^+\mu^-$ *and* $B \to K\mu^+\mu^-/B \to Ke^+e^-$ *in a two-Higgs-doublet model with gauged* $L_\mu - L_\tau$, *Phys. Rev. Lett.* **114** (2015) 151801, [`1501.00993`].

[271] W. Altmannshofer, P. Stangl and D. M. Straub, *Interpreting Hints for Lepton Flavor Universality Violation*, *Phys. Rev. D* **96** (2017) 055008, [`1704.05435`].

[272] LHCb collaboration, R. Aaij et al., *Precise determination of the* B^0_s–$\overline{B}{}^0_s$ *oscillation frequency*, *Nature Phys.* **18** (2022) 1–5, [`2104.04421`].

[273] L. Di Luzio, M. Kirk, A. Lenz and T. Rauh, ΔM_s *theory precision confronts flavour anomalies*, *JHEP* **12** (2019) 009, [`1909.11087`].

[274] D. King, A. Lenz and T. Rauh, B_s *mixing observables and —*V_{td}/V_{ts}*— from sum rules*, *JHEP* **05** (2019) 034, [`1904.00940`].

[275] M. Kirk, A. Lenz and T. Rauh, *Dimension-six matrix elements for meson mixing and lifetimes from sum rules*, *JHEP* **12** (2017) 068, [`1711.02100`].

[276] A. G. Grozin, R. Klein, T. Mannel and A. A. Pivovarov, $B^0 - \bar{B}^0$ *mixing at next-to-leading order*, *Phys. Rev. D* **94** (2016) 034024, [`1606.06054`].

[277] R. J. Dowdall, C. T. H. Davies, R. R. Horgan, G. P. Lepage, C. J. Monahan, J. Shigemitsu et al., *Neutral B-meson mixing from full lattice QCD at the physical point*, *Phys. Rev. D* **100** (2019) 094508, [`1907.01025`].

[278] RBC/UKQCD collaboration, P. A. Boyle, L. Del Debbio, N. Garron, A. Juttner, A. Soni, J. T. Tsang et al., *SU(3)-breaking ratios for* $D_{(s)}$ *and* $B_{(s)}$ *mesons*, `1812.08791`.

[279] Fermilab Lattice, MILC collaboration, A. Bazavov et al., $B^0_{(s)}$*-mixing matrix elements from lattice QCD for the Standard Model and beyond*, *Phys. Rev. D* **93** (2016) 113016, [`1602.03560`].

[280] A. J. Buras, M. Jamin and P. H. Weisz, *Leading and Next-to-leading QCD Corrections to* ϵ *Parameter and* $B^0 - \bar{B}^0$ *Mixing in the Presence of a Heavy Top Quark*, *Nucl. Phys. B* **347** (1990) 491–536.

[281] C. Q. Geng and J. N. Ng, *Charged Higgs Effect in B)d)0 -* $\bar{B}$*(d)0 Mixing,* $K \to \pi$ *Neutrino Anti-neutrino Decay and Rare Decays of B Mesons*, *Phys. Rev. D* **38** (1988) 2857.

[282] J. Urban, F. Krauss, U. Jentschura and G. Soff, *Next-to-leading order QCD corrections for the B0 anti-B0 mixing with an extended Higgs sector*, *Nucl. Phys. B* **523** (1998) 40–58, [hep-ph/9710245].

[283] M. Misiak, A. Rehman and M. Steinhauser, *Towards $\overline{B} \to X_s\gamma$ at the NNLO in QCD without interpolation in m_c*, *JHEP* **06** (2020) 175, [2002.01548].

[284] M. Misiak and M. Steinhauser, *NNLO QCD corrections to the $\bar{B} \to X_s\gamma$ matrix elements using interpolation in m(c)*, *Nucl. Phys. B* **764** (2007) 62–82, [hep-ph/0609241].

[285] M. Misiak et al., *Updated NNLO QCD predictions for the weak radiative B-meson decays*, *Phys. Rev. Lett.* **114** (2015) 221801, [1503.01789].

[286] CLEO collaboration, S. Chen et al., *Branching fraction and photon energy spectrum for $b \to s\gamma$*, *Phys. Rev. Lett.* **87** (2001) 251807, [hep-ex/0108032].

[287] BaBar collaboration, J. P. Lees et al., *Precision Measurement of the $B \to X_s\gamma$ Photon Energy Spectrum, Branching Fraction, and Direct CP Asymmetry $A_{CP}(B \to X_{s+d}\gamma)$*, *Phys. Rev. Lett.* **109** (2012) 191801, [1207.2690].

[288] Belle collaboration, A. Abdesselam et al., *Measurement of the inclusive $B \to X_{s+d}\gamma$ branching fraction, photon energy spectrum and HQE parameters*, in *38th International Conference on High Energy Physics*, 8, 2016. 1608.02344.

[289] LHCb collaboration, R. Aaij et al., *Measurement of the $B^0_s \to \mu^+\mu^-$ branching fraction and effective lifetime and search for $B^0 \to \mu^+\mu^-$ decays*, *Phys. Rev. Lett.* **118** (2017) 191801, [1703.05747].

[290] ATLAS collaboration, M. Aaboud et al., *Study of the rare decays of B^0_s and B^0 mesons into muon pairs using data collected during 2015 and 2016 with the ATLAS detector*, *JHEP* **04** (2019) 098, [1812.03017].

[291] CMS collaboration, A. M. Sirunyan et al., *Measurement of properties of $B^0_\mathrm{s} \to \mu^+\mu^-$ decays and search for $B^0 \to \mu^+\mu^-$ with the CMS experiment*, *JHEP* **04** (2020) 188, [1910.12127].

[292] LHCb, ATLAS, CMS collaboration, *Combination of the ATLAS, CMS and LHCb results on the $B^0_{(s)} \to \mu^+\mu^-$ decays*, LHCb-CONF-2020-002, CERN-LHCb-CONF-2020-002, (2020).

[293] LHCb collaboration, R. Aaij et al., *Measurement of the $B^0_s \to \mu^+\mu^-$ decay properties and*

search for the $B^0 \to \mu^+\mu^-$ and $B^0_s \to \mu^+\mu^-\gamma$ decays, *Phys. Rev. D* **105** (2022) 012010, [`2108.09283`].

[294] LHCb collaboration, R. Aaij et al., *Analysis of Neutral B-Meson Decays into Two Muons*, *Phys. Rev. Lett.* **128** (2022) 041801, [`2108.09284`].

[295] G. Buchalla and A. J. Buras, *QCD corrections to rare K and B decays for arbitrary top quark mass*, *Nucl. Phys. B* **400** (1993) 225–239.

[296] C. Bobeth, M. Gorbahn, T. Hermann, M. Misiak, E. Stamou and M. Steinhauser, *$B_{s,d} \to l^+l^-$ in the Standard Model with Reduced Theoretical Uncertainty*, *Phys. Rev. Lett.* **112** (2014) 101801, [`1311.0903`].

[297] M. Beneke, C. Bobeth and R. Szafron, *Power-enhanced leading-logarithmic QED corrections to $B_q \to \mu^+\mu^-$*, *JHEP* **10** (2019) 232, [`1908.07011`].

[298] ETM collaboration, A. Bussone et al., *Mass of the b quark and B -meson decay constants from N_f=2+1+1 twisted-mass lattice QCD*, *Phys. Rev. D* **93** (2016) 114505, [`1603.04306`].

[299] A. Bazavov et al., *B- and D-meson leptonic decay constants from four-flavor lattice QCD*, *Phys. Rev. D* **98** (2018) 074512, [`1712.09262`].

[300] C. Hughes, C. T. H. Davies and C. J. Monahan, *New methods for B meson decay constants and form factors from lattice NRQCD*, *Phys. Rev. D* **97** (2018) 054509, [`1711.09981`].

[301] H. E. Logan and U. Nierste, *$B_{s,d} \to \ell^+\ell^-$ in a two Higgs doublet model*, *Nucl. Phys. B* **586** (2000) 39–55, [`hep-ph/0004139`].

[302] C. Bobeth, G. Hiller and G. Piranishvili, *Angular distributions of $\bar{B} \to \bar{K}\ell^+\ell^-$ decays*, *JHEP* **12** (2007) 040, [`0709.4174`].

[303] M. Bordone, G. Isidori and A. Pattori, *On the Standard Model predictions for R_K and R_{K^*}*, *Eur. Phys. J. C* **76** (2016) 440, [`1605.07633`].

[304] T. Hurth, F. Mahmoudi and S. Neshatpour, *Model independent analysis of the angular observables in $B^0 \to K^{*0}\mu^+\mu^-$ and $B^+ \to K^{*+}\mu^+\mu^-$*, *Phys. Rev. D* **103** (2021) 095020, [`2012.12207`].

[305] L.-S. Geng, B. Grinstein, S. Jäger, J. Martin Camalich, X.-L. Ren and R.-X. Shi, *Towards the discovery of new physics with lepton-universality ratios of $b \to s\ell\ell$ decays*, *Phys. Rev. D* **96** (2017) 093006, [`1704.05446`].

[306] M. Ciuchini, A. M. Coutinho, M. Fedele, E. Franco, A. Paul, L. Silvestrini et al., *New Physics in $b \to s\ell^+\ell^-$ confronts new data on Lepton Universality*, *Eur. Phys. J. C* **79** (2019) 719, [1903.09632].

[307] A. Datta, J. Kumar and D. London, *The B anomalies and new physics in $b \to se^+e^-$*, *Phys. Lett. B* **797** (2019) 134858, [1903.10086].

[308] K. Kowalska, D. Kumar and E. M. Sessolo, *Implications for new physics in $b \to s\mu\mu$ transitions after recent measurements by Belle and LHCb*, *Eur. Phys. J. C* **79** (2019) 840, [1903.10932].

[309] T. Hurth, F. Mahmoudi and S. Neshatpour, *Implications of the new LHCb angular analysis of $B \to K^*\mu^+\mu^-$: Hadronic effects or new physics?*, *Phys. Rev. D* **102** (2020) 055001, [2006.04213].

[310] M. Ciuchini, M. Fedele, E. Franco, A. Paul, L. Silvestrini and M. Valli, *Lessons from the $B^{0,+} \to K^{*0,+}\mu^+\mu^-$ angular analyses*, *Phys. Rev. D* **103** (2021) 015030, [2011.01212].

[311] G. Hiller and F. Kruger, *More model-independent analysis of $b \to s$ processes*, *Phys. Rev. D* **69** (2004), 074020, [hep-ph/0310219].

[312] M. Algueró, B. Capdevila, A. Crivellin, S. Descotes-Genon, P. Masjuan, J. Matias et al., *Emerging patterns of New Physics with and without Lepton Flavour Universal contributions*, *Eur. Phys. J. C* **79** (2019) 714, [1903.09578].

[313] A. K. Alok, A. Dighe, S. Gangal and D. Kumar, *Continuing search for new physics in $b \to s\mu\mu$ decays: two operators at a time*, *JHEP* **06** (2019) 089, [1903.09617].

[314] J. Aebischer, W. Altmannshofer, D. Guadagnoli, M. Reboud, P. Stangl and D. M. Straub, *B-decay discrepancies after Moriond 2019*, *Eur. Phys. J. C* **80** (2020) 252, [1903.10434].

[315] A. Carvunis, F. Dettori, S. Gangal, D. Guadagnoli and C. Normand, *On the effective lifetime of $B_s \to \mu\mu\gamma$*, *JHEP* **12** (2021) 078, [2102.13390].

[316] LHCb collaboration, R. Aaij et al., *Measurement of lepton universality parameters in $B^+ \to K^+\ell^+\ell^-$ and $B^0 \to K^{*0}\ell^+\ell^-$ decays*, *Phys. Rev. D* **108** (2023) 032002, [2212.09153].

[317] A. Khodjamirian, T. Mannel, A. A. Pivovarov and Y. M. Wang, *Charm-loop effect in $B \to K^{(*)}\ell^+\ell^-$ and $B \to K^*\gamma$*, *JHEP* **09** (2010) 089, [1006.4945].

[318] A. Khodjamirian, T. Mannel and Y. M. Wang, *$B \to K\ell^+\ell^-$ decay at large hadronic recoil*, *JHEP* **02** (2013) 010, [`1211.0234`].

[319] A. Khodjamirian and A. V. Rusov, *$B_s \to K\ell\nu_\ell$ and $B_{(s)} \to \pi(K)\ell^+\ell^-$ decays at large recoil and CKM matrix elements*, *JHEP* **08** (2017) 112, [`1703.04765`].

[320] T. Hurth, F. Mahmoudi, D. M. Santos and S. Neshatpour, *More Indications for Lepton Nonuniversality in $b \to s\ell^+\ell^-$*, *Phys. Lett. B* **824** (2022) 136838, [`2104.10058`].

[321] M. Algueró, B. Capdevila, S. Descotes-Genon, J. Matias and M. Novoa-Brunet, *$b \to s\ell^+\ell^-$ global fits after R_{K_S} and $R_{K^{*+}}$*, *Eur. Phys. J. C* **82** (2022) 326, [`2104.08921`].

[322] C. Cornella, D. A. Faroughy, J. Fuentes-Martin, G. Isidori and M. Neubert, *Reading the footprints of the B-meson flavor anomalies*, *JHEP* **08** (2021) 050, [`2103.16558`].

[323] L.-S. Geng, B. Grinstein, S. Jäger, S.-Y. Li, J. Martin Camalich and R.-X. Shi, *Implications of new evidence for lepton-universality violation in $b \to s\ell^+\ell^-$ decays*, *Phys. Rev. D* **104** (2021) 035029, [`2103.12738`].

[324] F. Munir Bhutta, Z.-R. Huang, C.-D. Lü, M. A. Paracha and W. Wang, *New physics in $b \to s\ell\ell$ anomalies and its implications for the complementary neutral current decays*, *Nucl. Phys. B* **979** (2022) 115763, [`2009.03588`].

[325] A. Biswas, S. Nandi, S. K. Patra and I. Ray, *New physics in $b \to s\ell\ell$ decays with complex Wilson coefficients*, *Nucl. Phys. B* **969** (2021) 115479, [`2004.14687`].

[326] P. Bechtle, O. Brein, S. Heinemeyer, G. Weiglein and K. E. Williams, *HiggsBounds: Confronting Arbitrary Higgs Sectors with Exclusion Bounds from LEP and the Tevatron*, *Comput. Phys. Commun.* **181** (2010) 138–167, [`0811.4169`].

[327] P. Bechtle, O. Brein, S. Heinemeyer, G. Weiglein and K. E. Williams, *HiggsBounds 2.0.0: Confronting Neutral and Charged Higgs Sector Predictions with Exclusion Bounds from LEP and the Tevatron*, *Comput. Phys. Commun.* **182** (2011) 2605–2631, [`1102.1898`].

[328] P. Bechtle, O. Brein, S. Heinemeyer, O. Stal, T. Stefaniak, G. Weiglein et al., *Recent Developments in HiggsBounds and a Preview of HiggsSignals*, *PoS* **CHARGED2012** (2012) 024, [`1301.2345`].

[329] P. Bechtle, O. Brein, S. Heinemeyer, O. Stål, T. Stefaniak, G. Weiglein et al.,

HiggsBounds – 4*: Improved Tests of Extended Higgs Sectors against Exclusion Bounds from LEP, the Tevatron and the LHC*, *Eur. Phys. J. C* **74** (2014) 2693, [`1311.0055`].

[330] P. Bechtle, S. Heinemeyer, O. Stal, T. Stefaniak and G. Weiglein, *Applying Exclusion Likelihoods from LHC Searches to Extended Higgs Sectors*, *Eur. Phys. J. C* **75** (2015) 421, [`1507.06706`].

[331] P. Bechtle, D. Dercks, S. Heinemeyer, T. Klingl, T. Stefaniak, G. Weiglein et al., *HiggsBounds-5: Testing Higgs Sectors in the LHC 13 TeV Era*, *Eur. Phys. J. C* **80** (2020) 1211, [`2006.06007`].

[332] H. Bahl, V. M. Lozano, T. Stefaniak and J. Wittbrodt, *Testing exotic scalars with HiggsBounds*, *Eur. Phys. J. C* **82** (2022) 584, [`2109.10366`].

[333] M. Krause, M. Mühlleitner and M. Spira, *2HDECAY —A program for the calculation of electroweak one-loop corrections to Higgs decays in the Two-Higgs-Doublet Model including state-of-the-art QCD corrections*, *Comput. Phys. Commun.* **246** (2020) 106852, [`1810.00768`].

[334] A. Djouadi, J. Kalinowski and M. Spira, *HDECAY: A Program for Higgs boson decays in the standard model and its supersymmetric extension*, *Comput. Phys. Commun.* **108** (1998) 56–74, [`hep-ph/9704448`].

[335] HDECAY collaboration, A. Djouadi, J. Kalinowski, M. Muehlleitner and M. Spira, *HDECAY: Twenty$_{++}$ years after*, *Comput. Phys. Commun.* **238** (2019) 214–231, [`1801.09506`].

[336] M. Krause, M. Muhlleitner, R. Santos and H. Ziesche, *Higgs-to-Higgs boson decays in a 2HDM at next-to-leading order*, *Phys. Rev. D* **95** (2017) 075019, [`1609.04185`].

[337] A. Denner, S. Dittmaier and J.-N. Lang, *Renormalization of mixing angles*, *JHEP* **11** (2018) 104, [`1808.03466`].

[338] J. Alwall, R. Frederix, S. Frixione, V. Hirschi, F. Maltoni, O. Mattelaer et al., *The automated computation of tree-level and next-to-leading order differential cross sections, and their matching to parton shower simulations*, *JHEP* **07** (2014) 079, [`1405.0301`].

[339] A. Belvedere, C. Englert, R. Kogler and M. Spannowsky, *Dispelling the $\sqrt{L}$ myth for the High-Luminosity LHC*, `2402.07985`.

[340] ALEPH, DELPHI, L3, OPAL, LEP collaboration, G. Abbiendi et al., *Search for Charged Higgs bosons: Combined Results Using LEP Data*, *Eur. Phys. J. C* **73** (2013) 2463, [1301.6065].

[341] CMS collaboration, A. M. Sirunyan et al., *Search for physics beyond the standard model in multilepton final states in proton-proton collisions at $\sqrt{s} = 13$ TeV*, *JHEP* **03** (2020) 051, [1911.04968].

[342] CMS collaboration, A. M. Sirunyan et al., *Search for charged Higgs bosons in the $H^{\pm} \to \tau^{\pm}\nu_{\tau}$ decay channel in proton-proton collisions at $\sqrt{s} = 13$ TeV*, *JHEP* **07** (2019) 142, [1903.04560].

[343] ATLAS collaboration, *Search for charged Higgs bosons decaying into a top-quark and a bottom-quark at $\sqrt{s} = 13$ TeV with the ATLAS detector*, ATLAS-CONF-2020-039, (2020).

[344] ALEPH, DELPHI, L3, OPAL, LEP Working Group for Higgs Boson Searches collaboration, S. Schael et al., *Search for neutral MSSM Higgs bosons at LEP*, *Eur. Phys. J. C* **47** (2006) 547–587, [hep-ex/0602042].

[345] ATLAS collaboration, *Search for resonances in the 65 to 110 GeV diphoton invariant mass range using 80 fb^{-1} of pp collisions collected at $\sqrt{s} = 13$ TeV with the ATLAS detector*, ATLAS-CONF-2018-025, (2018).

[346] ATLAS collaboration, G. Aad et al., *Search for Scalar Diphoton Resonances in the Mass Range $65-600$ GeV with the ATLAS Detector in pp Collision Data at $\sqrt{s} = 8$ TeV*, *Phys. Rev. Lett.* **113** (2014) 171801, [1407.6583].

[347] ATLAS collaboration, G. Aad et al., *Search for heavy Higgs bosons decaying into two tau leptons with the ATLAS detector using pp collisions at $\sqrt{s} = 13$ TeV*, *Phys. Rev. Lett.* **125** (2020) 051801, [2002.12223].

[348] CMS collaboration, A. M. Sirunyan et al., *Search for low-mass resonances decaying into bottom quark-antiquark pairs in proton-proton collisions at $\sqrt{s} = 13$ TeV*, *Phys. Rev. D* **99** (2019) 012005, [1810.11822].

[349] CMS collaboration, *Search for charged Higgs bosons with the $H^{\pm} \to \tau^{\pm}\nu_{\tau}$ decay channel in proton-proton collisions at $\sqrt{s} = 13$ TeV*, CMS-PAS-HIG-18-014, (2018).

[350] CMS collaboration, *Search for additional neutral Higgs bosons decaying to a pair of tau leptons in pp collisions at* $\sqrt{s}$ *= 7 and 8 TeV*, CMS-PAS-HIG-14-029, (2015).

[351] CMS collaboration, V. Khachatryan et al., *Search for neutral MSSM Higgs bosons decaying into a pair of bottom quarks*, *JHEP* **11** (2015) 071, [`1506.08329`].

[352] G. C. Dorsch, S. J. Huber, T. Konstandin and J. M. No, *A Second Higgs Doublet in the Early Universe: Baryogenesis and Gravitational Waves*, *JCAP* **05** (2017) 052, [`1611.05874`].

[353] P. S. Bhupal Dev and A. Pilaftsis, *Maximally Symmetric Two Higgs Doublet Model with Natural Standard Model Alignment*, *JHEP* **12** (2014) 024, [`1408.3405`].

[354] Anisha, D. Azevedo, L. Biermann, C. Englert and M. Mühlleitner, *Effective 2HDM Yukawa interactions and a strong first-order electroweak phase transition*, *JHEP* **02** (2024) 045, [`2311.06353`].

[355] P. Basler and M. Mühlleitner, *BSMPT (Beyond the Standard Model Phase Transitions): A tool for the electroweak phase transition in extended Higgs sectors*, *Comput. Phys. Commun.* **237** (2019) 62–85, [`1803.02846`].

[356] P. Basler, M. Mühlleitner and J. Müller, *BSMPT v2 a tool for the electroweak phase transition and the baryon asymmetry of the universe in extended Higgs Sectors*, *Comput. Phys. Commun.* **269** (2021) 108124, [`2007.01725`].

[357] L. Wang, J. M. Yang, M. Zhang and Y. Zhang, *Revisiting lepton-specific 2HDM in light of muon* $g-2$ *anomaly*, *Phys. Lett. B* **788** (2019) 519–529, [`1809.05857`].

[358] X.-F. Han, T. Li, L. Wang and Y. Zhang, *Simple interpretations of lepton anomalies in the lepton-specific inert two-Higgs-doublet model*, *Phys. Rev. D* **99** (2019) 095034, [`1812.02449`].

[359] S. M. Barr and A. Zee, *Electric Dipole Moment of the Electron and of the Neutron*, *Phys. Rev. Lett.* **65** (1990) 21–24.

[360] M. Cè et al., *Window observable for the hadronic vacuum polarization contribution to the muon g-2 from lattice QCD*, *Phys. Rev. D* **106** (2022) 114502, [`2206.06582`].

[361] Extended Twisted Mass collaboration, C. Alexandrou et al., *Lattice calculation of the short and intermediate time-distance hadronic vacuum polarization contributions to the*

muon magnetic moment using twisted-mass fermions, *Phys. Rev. D* **107** (2023) 074506, [2206.15084].

[362] G. Colangelo, A. X. El-Khadra, M. Hoferichter, A. Keshavarzi, C. Lehner, P. Stoffer et al., *Data-driven evaluations of Euclidean windows to scrutinize hadronic vacuum polarization*, *Phys. Lett. B* **833** (2022) 137313, [2205.12963].

[363] A. Crivellin, M. Hoferichter, C. A. Manzari and M. Montull, *Hadronic Vacuum Polarization: $(g-2)_\mu$ versus Global Electroweak Fits*, *Phys. Rev. Lett.* **125** (2020) 091801, [2003.04886].

[364] A. Keshavarzi, W. J. Marciano, M. Passera and A. Sirlin, *Muon $g-2$ and $\Delta\alpha$ connection*, *Phys. Rev. D* **102** (2020) 033002, [2006.12666].

[365] B. Malaescu and M. Schott, *Impact of correlations between a_μ and α_{QED} on the EW fit*, *Eur. Phys. J. C* **81** (2021) 46, [2008.08107].

[366] G. Colangelo, M. Hoferichter and P. Stoffer, *Constraints on the two-pion contribution to hadronic vacuum polarization*, *Phys. Lett. B* **814** (2021) 136073, [2010.07943].

[367] C. M. Carloni Calame, M. Passera, L. Trentadue and G. Venanzoni, *A new approach to evaluate the leading hadronic corrections to the muon g-2*, *Phys. Lett. B* **746** (2015) 325–329, [1504.02228].

[368] G. Abbiendi et al., *Measuring the leading hadronic contribution to the muon g-2 via μe scattering*, *Eur. Phys. J. C* **77** (2017) 139, [1609.08987].

[369] E. Balzani, S. Laporta and M. Passera, *Hadronic vacuum polarization contributions to the muon g-2 in the space-like region*, *Phys. Lett. B* **834** (2022) 137462, [2112.05704].

[370] P. Mastrolia, M. Passera, A. Primo and U. Schubert, *Master integrals for the NNLO virtual corrections to μe scattering in QED: the planar graphs*, *JHEP* **11** (2017) 198, [1709.07435].

[371] G. I. Gakh, M. I. Konchatnij, N. P. Merenkov, V. N. Kharkov and E. Tomasi-Gustafsson, *Leptonic radiative corrections to elastic deuteron-electron scattering*, *Phys. Rev. C* **98** (2018) 045212, [1804.01399].

[372] S. Di Vita, S. Laporta, P. Mastrolia, A. Primo and U. Schubert, *Master integrals for the*

NNLO virtual corrections to μe scattering in QED: the non-planar graphs, *JHEP* **09** (2018) 016, [1806.08241].

[373] C. M. Carloni Calame, M. Chiesa, S. M. Hasan, G. Montagna, O. Nicrosini and F. Piccinini, *Towards muon-electron scattering at NNLO*, *JHEP* **11** (2020) 028, [2007.01586].

[374] P. Banerjee, T. Engel, N. Schalch, A. Signer and Y. Ulrich, *Bhabha scattering at NNLO with next-to-soft stabilisation*, *Phys. Lett. B* **820** (2021) 136547, [2106.07469].

[375] E. Budassi, C. M. Carloni Calame, M. Chiesa, C. L. Del Pio, S. M. Hasan, G. Montagna et al., *NNLO virtual and real leptonic corrections to muon-electron scattering*, *JHEP* **11** (2021) 098, [2109.14606].

[376] P. S. B. Dev, W. Rodejohann, X.-J. Xu and Y. Zhang, *MUonE sensitivity to new physics explanations of the muon anomalous magnetic moment*, *JHEP* **05** (2020) 053, [2002.04822].

[377] A. Masiero, P. Paradisi and M. Passera, *New physics at the MUonE experiment at CERN*, *Phys. Rev. D* **102** (2020) 075013, [2002.05418].

[378] K. Asai, K. Hamaguchi, N. Nagata, S.-Y. Tseng and J. Wada, *Probing the $L_\mu - L_\tau$ gauge boson at the MUonE experiment*, *Phys. Rev. D* **106** (2022) L051702, [2109.10093].

[379] I. Galon, D. Shih and I. R. Wang, *Dark photons and displaced vertices at the MUonE experiment*, *Phys. Rev. D* **107** (2023) 095003, [2202.08843].

[380] T. Kinoshita, *Mass singularities of Feynman amplitudes*, *J. Math. Phys.* **3** (1962) 650–677.

[381] T. D. Lee and M. Nauenberg, *Degenerate Systems and Mass Singularities*, *Phys. Rev.* **133** (1964) B1549–B1562.

[382] G. 't Hooft and M. J. G. Veltman, *Scalar One Loop Integrals*, *Nucl. Phys. B* **153** (1979) 365–401.

[383] A. Denner, *Techniques for calculation of electroweak radiative corrections at the one loop level and results for W physics at LEP-200*, *Fortsch. Phys.* **41** (1993) 307–420, [0709.1075].

[384] CDF collaboration, T. Aaltonen et al., *High-precision measurement of the W boson mass with the CDF II detector*, *Science* **376** (2022) 170–176.

[385] H. Bahl, J. Braathen and G. Weiglein, *New physics effects on the W-boson mass from a doublet extension of the SM Higgs sector*, *Phys. Lett. B* **833** (2022) 137295, [2204.05269].

[386] H. Song, W. Su and M. Zhang, *Electroweak phase transition in 2HDM under Higgs, Z-pole, and W precision measurements*, *JHEP* **10** (2022) 048, [2204.05085].

[387] Y. Heo, D.-W. Jung and J. S. Lee, *Impact of the CDF W-mass anomaly on two Higgs doublet model*, *Phys. Lett. B* **833** (2022) 137274, [2204.05728].

[388] Y. H. Ahn, S. K. Kang and R. Ramos, *Implications of New CDF-II W Boson Mass on Two Higgs Doublet Model*, *Phys. Rev. D* **106** (2022) 055038, [2204.06485].

[389] S. Lee, K. Cheung, J. Kim, C.-T. Lu and J. Song, *Status of the two-Higgs-doublet model in light of the CDF mW measurement*, *Phys. Rev. D* **106** (2022) 075013, [2204.10338].

[390] R. Benbrik, M. Boukidi and B. Manaut, *Interpreting the $\boldsymbol{W}$-Mass and Muon $\boldsymbol{(g_\mu - 2)}$ Anomalies within a 2-Higgs Doublet Model*, 2204.11755.

[391] H. Abouabid, A. Arhrib, R. Benbrik, M. Krab and M. Ouchemhou, *Is the new CDF MW measurement consistent with the two-Higgs doublet model?*, *Nucl. Phys. B* **989** (2023) 116143, [2204.12018].

[392] F. J. Botella, F. Cornet-Gomez, C. Miró and M. Nebot, *Muon and electron $g-2$ anomalies in a flavor conserving 2HDM with an oblique view on the CDF M_W value*, *Eur. Phys. J. C* **82** (2022) 915, [2205.01115].

[393] J. Kim, *Compatibility of muon $g-2$, W mass anomaly in type-X 2HDM*, *Phys. Lett. B* **832** (2022) 137220, [2205.01437].

[394] J. Kim, S. Lee, P. Sanyal and J. Song, *CDF W-boson mass and muon g-2 in a type-X two-Higgs-doublet model with a Higgs-phobic light pseudoscalar*, *Phys. Rev. D* **106** (2022) 035002, [2205.01701].

[395] C.-T. Lu, L. Wu, Y. Wu and B. Zhu, *Electroweak precision fit and new physics in light of the W boson mass*, *Phys. Rev. D* **106** (2022) 035034, [2204.03796].

[396] T. Corbett, O. J. P. Eboli, D. Goncalves, J. Gonzalez-Fraile, T. Plehn and M. Rauch, *The Higgs Legacy of the LHC Run I*, *JHEP* **08** (2015) 156, [1505.05516].

[397] T. Corbett, O. J. P. Eboli, D. Goncalves, J. Gonzalez-Fraile, T. Plehn and M. Rauch, *The Non-Linear Higgs Legacy of the LHC Run I*, 1511.08188.

[398] C. Englert, R. Kogler, H. Schulz and M. Spannowsky, *Higgs coupling measurements at the LHC*, *Eur. Phys. J. C* **76** (2016) 393, [`1511.05170`].

[399] C. Englert, R. Kogler, H. Schulz and M. Spannowsky, *Higgs characterisation in the presence of theoretical uncertainties and invisible decays*, *Eur. Phys. J. C* **77** (2017) 789, [`1708.06355`].

[400] J. Ellis, V. Sanz and T. You, *The Effective Standard Model after LHC Run I*, *JHEP* **03** (2015) 157, [`1410.7703`].

[401] J. de Blas et al., *Higgs Boson Studies at Future Particle Colliders*, *JHEP* **01** (2020) 139, [`1905.03764`].

[402] J. De Blas, G. Durieux, C. Grojean, J. Gu and A. Paul, *On the future of Higgs, electroweak and diboson measurements at lepton colliders*, *JHEP* **12** (2019) 117, [`1907.04311`].

[403] J. Ellis, M. Madigan, K. Mimasu, V. Sanz and T. You, *Top, Higgs, Diboson and Electroweak Fit to the Standard Model Effective Field Theory*, *JHEP* **04** (2021) 279, [`2012.02779`].

[404] J. Brehmer, F. Kling, T. Plehn and T. M. P. Tait, *Better Higgs-CP Tests Through Information Geometry*, *Phys. Rev. D* **97** (2018) 095017, [`1712.02350`].

[405] J. Brehmer, K. Cranmer, F. Kling and T. Plehn, *Better Higgs boson measurements through information geometry*, *Phys. Rev. D* **95** (2017) 073002, [`1612.05261`].

[406] J. Brehmer, K. Cranmer, G. Louppe and J. Pavez, *Constraining Effective Field Theories with Machine Learning*, *Phys. Rev. Lett.* **121** (2018) 111801, [`1805.00013`].

[407] J. Brehmer, K. Cranmer, G. Louppe and J. Pavez, *A Guide to Constraining Effective Field Theories with Machine Learning*, *Phys. Rev. D* **98** (2018) 052004, [`1805.00020`].

[408] J. D'Hondt, A. Mariotti, K. Mimasu, S. Moortgat and C. Zhang, *Learning to pinpoint effective operators at the LHC: a study of the* $\mathrm{t\bar{t}b\bar{b}}$ *signature*, *JHEP* **11** (2018) 131, [`1807.02130`].

[409] S. Chatterjee, N. Frohner, L. Lechner, R. Schöfbeck and D. Schwarz, *Tree boosting for learning EFT parameters*, *Comput. Phys. Commun.* **277** (2022) 108385, [`2107.10859`].

[410] J. Y. Araz and M. Spannowsky, *Combine and Conquer: Event Reconstruction with Bayesian Ensemble Neural Networks*, *JHEP* **04** (2021) 296, [`2102.01078`].

[411] P. Konar, V. S. Ngairangbam and M. Spannowsky, *Energy-weighted message passing: an infra-red and collinear safe graph neural network algorithm*, *JHEP* **02** (2022) 060, [`2109.14636`].

[412] A. Buckley, C. Englert, J. Ferrando, D. J. Miller, L. Moore, M. Russell et al., *Global fit of top quark effective theory to data*, *Phys. Rev. D* **92** (2015) 091501, [`1506.08845`].

[413] A. Buckley, C. Englert, J. Ferrando, D. J. Miller, L. Moore, M. Russell et al., *Constraining top quark effective theory in the LHC Run II era*, *JHEP* **04** (2016) 015, [`1512.03360`].

[414] M. Vos et al., *Top physics at high-energy lepton colliders*, `1604.08122`.

[415] N. Castro, J. Erdmann, C. Grunwald, K. Kröninger and N.-A. Rosien, *EFTfitter—A tool for interpreting measurements in the context of effective field theories*, *Eur. Phys. J. C* **76** (2016) 432, [`1605.05585`].

[416] D. Barducci et al., *Interpreting top-quark LHC measurements in the standard-model effective field theory*, `1802.07237`.

[417] N. P. Hartland, F. Maltoni, E. R. Nocera, J. Rojo, E. Slade, E. Vryonidou et al., *A Monte Carlo global analysis of the Standard Model Effective Field Theory: the top quark sector*, *JHEP* **04** (2019) 100, [`1901.05965`].

[418] I. Brivio, S. Bruggisser, F. Maltoni, R. Moutafis, T. Plehn, E. Vryonidou et al., *O new physics, where art thou? A global search in the top sector*, *JHEP* **02** (2020) 131, [`1910.03606`].

[419] SMEFiT collaboration, J. J. Ethier, G. Magni, F. Maltoni, L. Mantani, E. R. Nocera, J. Rojo et al., *Combined SMEFT interpretation of Higgs, diboson, and top quark data from the LHC*, *JHEP* **11** (2021) 089, [`2105.00006`].

[420] J. Zhou, G. Cui, Z. Zhang, C. Yang, Z. Liu, L. Wang et al., *Graph neural networks: A review of methods and applications*, `1812.08434`.

[421] Z. Wu, S. Pan, F. Chen, G. Long, C. Zhang and P. S. Yu, *A comprehensive survey on graph neural networks*, *IEEE Transactions on Neural Networks and Learning Systems* **32** (2021) 4–24, [`1901.00596`].

[422] J. Gilmer, S. S. Schoenholz, P. F. Riley, O. Vinyals and G. E. Dahl, *Neural message*

passing for quantum chemistry, in *International Conference on Machine Learning*, pp. 1263–1272, PMLR, 2017. 1704.01212.

[423] Y. Wang, Y. Sun, Z. Liu, S. E. Sarma, M. M. Bronstein and J. M. Solomon, *Dynamic graph cnn for learning on point clouds*, *Acm Transactions On Graphics (tog)* **38** (2019) 1–12, [1801.07829].

[424] F. A. Dreyer and H. Qu, *Jet tagging in the Lund plane with graph networks*, *JHEP* **03** (2021) 052, [2012.08526].

[425] A. Blance and M. Spannowsky, *Unsupervised event classification with graphs on classical and photonic quantum computers*, *JHEP* **21** (2020) 170, [2103.03897].

[426] H. Qu and L. Gouskos, *ParticleNet: Jet Tagging via Particle Clouds*, *Phys. Rev. D* **101** (2020) 056019, [1902.08570].

[427] T. Dorigo, M. Fumanelli, C. Maccani, M. Mojsovska, G. C. Strong and B. Scarpa, *RanBox: anomaly detection in the copula space*, *JHEP* **01** (2023) 008, [2106.05747].

[428] V. Mikuni and F. Canelli, *ABCNet: An attention-based method for particle tagging*, *Eur. Phys. J. Plus* **135** (2020) 463, [2001.05311].

[429] O. Knapp, O. Cerri, G. Dissertori, T. Q. Nguyen, M. Pierini and J.-R. Vlimant, *Adversarially Learned Anomaly Detection on CMS Open Data: re-discovering the top quark*, *Eur. Phys. J. Plus* **136** (2021) 236, [2005.01598].

[430] V. Mikuni and F. Canelli, *Unsupervised clustering for collider physics*, *Phys. Rev. D* **103** (2021) 092007, [2010.07106].

[431] G. DeZoort, S. Thais, J. Duarte, V. Razavimaleki, M. Atkinson, I. Ojalvo et al., *Charged Particle Tracking via Edge-Classifying Interaction Networks*, *Comput. Softw. Big Sci.* **5** (2021) 26, [2103.16701].

[432] M. Abdughani, J. Ren, L. Wu and J. M. Yang, *Probing stop pair production at the LHC with graph neural networks*, *JHEP* **08** (2019) 055, [1807.09088].

[433] A. Alloul, N. D. Christensen, C. Degrande, C. Duhr and B. Fuks, *FeynRules 2.0 - A complete toolbox for tree-level phenomenology*, *Comput. Phys. Commun.* **185** (2014) 2250–2300, [1310.1921].

[434] I. Brivio, Y. Jiang and M. Trott, *The SMEFTsim package, theory and tools*, *JHEP* **12** (2017) 070, [`1709.06492`].

[435] I. Brivio, *SMEFTsim 3.0 — a practical guide*, *JHEP* **04** (2021) 073, [`2012.11343`].

[436] A. Buckley, C. Englert, J. Ferrando, D. J. Miller, L. Moore, K. Nördstrom et al., *Results from TopFitter*, *PoS* **CKM2016** (2016) 127, [`1612.02294`].

[437] S. Brown, A. Buckley, C. Englert, J. Ferrando, P. Galler, D. J. Miller et al., *TopFitter: Fitting top-quark Wilson Coefficients to Run II data*, *PoS* **ICHEP2018** (2019) 293, [`1901.03164`].

[438] S. Brown, A. Buckley, C. Englert, J. Ferrando, P. Galler, D. Miller et al., *New results from TopFitter*, *PoS* **ICHEP2020** (2021) 322.

[439] CMS collaboration, V. Khachatryan et al., *Measurement of differential cross sections for top quark pair production using the lepton+jets final state in proton-proton collisions at 13 TeV*, *Phys. Rev. D* **95** (2017) 092001, [`1610.04191`].

[440] A. Buckley, J. Butterworth, D. Grellscheid, H. Hoeth, L. Lonnblad, J. Monk et al., *Rivet user manual*, *Comput. Phys. Commun.* **184** (2013) 2803–2819, [`1003.0694`].

[441] C. Bierlich et al., *Robust Independent Validation of Experiment and Theory: Rivet version 3*, *SciPost Phys.* **8** (2020) 026, [`1912.05451`].

[442] Particle Data Group collaboration, R. L. Workman et al., *Review of Particle Physics*, *PTEP* **2022** (2022) 083C01.

[443] Y. Lecun, L. Bottou, Y. Bengio and P. Haffner, *Gradient-based learning applied to document recognition*, *Proceedings of the IEEE* **86** (1998) 2278–2324.

[444] M. Wang, D. Zheng, Z. Ye, Q. Gan, M. Li, X. Song et al., *Deep graph library: A graph-centric, highly-performant package for graph neural networks*, 2020.

[445] A. Paszke, S. Gross, F. Massa, A. Lerer, J. Bradbury, G. Chanan et al., *Pytorch: An imperative style, high-performance deep learning library*, 2019.

[446] H. K. Dreiner, A. Duff and D. Zeppenfeld, *How well do we know the three gluon vertex?*, *Phys. Lett. B* **282** (1992) 441–447.

[447] L. J. Dixon and Y. Shadmi, *Testing gluon selfinteractions in three jet events at hadron colliders*, *Nucl. Phys. B* **423** (1994) 3–32, [`hep-ph/9312363`].

[448] G. Louppe, M. Kagan and K. Cranmer, *Learning to Pivot with Adversarial Networks*, `1611.01046`.

[449] R. Kansal, J. Duarte, H. Su, B. Orzari, T. Tomei, M. Pierini et al., *Particle Cloud Generation with Message Passing Generative Adversarial Networks*, in *35th Conference on Neural Information Processing Systems*, 6, 2021. `2106.11535`.

[450] C. Englert, P. Galler, P. Harris and M. Spannowsky, *Machine Learning Uncertainties with Adversarial Neural Networks*, *Eur. Phys. J. C* **79** (2019) 4, [`1807.08763`].

[451] M. Bellagente, A. Butter, G. Kasieczka, T. Plehn and R. Winterhalder, *How to GAN away Detector Effects*, *SciPost Phys.* **8** (2020) 070, [`1912.00477`].

[452] C. Englert, P. Galler, A. Pilkington and M. Spannowsky, *Approaching robust EFT limits for CP-violation in the Higgs sector*, *Phys. Rev. D* **99** (2019) 095007, [`1901.05982`].

[453] S. Das Bakshi, J. Chakrabortty, C. Englert, M. Spannowsky and P. Stylianou, *CP violation at ATLAS in effective field theory*, *Phys. Rev. D* **103** (2021) 055008, [`2009.13394`].

[454] S. D. Bakshi, J. Chakrabortty, C. Englert, M. Spannowsky and P. Stylianou, *Landscaping CP-violating BSM scenarios*, *Nucl. Phys. B* **975** (2022) 115676, [`2103.15861`].

[455] J. H. Collins, P. Martín-Ramiro, B. Nachman and D. Shih, *Comparing weak- and unsupervised methods for resonant anomaly detection*, *Eur. Phys. J. C* **81** (2021) 617, [`2104.02092`].

[456] CMS collaboration, A. M. Sirunyan et al., *MUSiC: a model unspecific search for new physics in proton-proton collisions at* $\sqrt{s} = 13$ *TeV*, `2010.02984`.

[457] ATLAS collaboration, M. Aaboud et al., *A strategy for a general search for new phenomena using data-derived signal regions and its application within the ATLAS experiment*, *Eur. Phys. J. C* **79** (2019) 120, [`1807.07447`].

[458] J. H. Collins, K. Howe and B. Nachman, *Anomaly Detection for Resonant New Physics with Machine Learning*, *Phys. Rev. Lett.* **121** (2018) 241803, [`1805.02664`].

[459] A. Blance, M. Spannowsky and P. Waite, *Adversarially-trained autoencoders for robust unsupervised new physics searches*, *JHEP* **10** (2019) 047, [`1905.10384`].

[460] J. Hajer, Y.-Y. Li, T. Liu and H. Wang, *Novelty Detection Meets Collider Physics*, *Phys. Rev. D* **101** (2020) 076015, [`1807.10261`].

[461] A. De Simone and T. Jacques, *Guiding New Physics Searches with Unsupervised Learning*, *Eur. Phys. J. C* **79** (2019) 289, [`1807.06038`].

[462] B. Nachman and D. Shih, *Anomaly Detection with Density Estimation*, *Phys. Rev. D* **101** (2020) 075042, [`2001.04990`].

[463] B. Nachman, *Anomaly Detection for Physics Analysis and Less than Supervised Learning*, `2010.14554`.

[464] ATLAS collaboration, G. Aad et al., *Measurements of the W production cross sections in association with jets with the ATLAS detector*, *Eur. Phys. J. C* **75** (2015) 82, [`1409.8639`].

[465] D. E. Soper and M. Spannowsky, *Finding physics signals with shower deconstruction*, *Phys. Rev. D* **84** (2011) 074002, [`1102.3480`].

[466] D. E. Soper and M. Spannowsky, *Finding physics signals with event deconstruction*, *Phys. Rev. D* **89** (2014) 094005, [`1402.1189`].

[467] A. Hallin, J. Isaacson, G. Kasieczka, C. Krause, B. Nachman, T. Quadfasel et al., *Classifying anomalies through outer density estimation*, *Phys. Rev. D* **106** (2022) 055006, [`2109.00546`].

[468] T. Cheng, J.-F. Arguin, J. Leissner-Martin, J. Pilette and T. Golling, *Variational autoencoders for anomalous jet tagging*, *Phys. Rev. D* **107** (2023) 016002, [`2007.01850`].

[469] F. Canelli, A. de Cosa, L. L. Pottier, J. Niedziela, K. Pedro and M. Pierini, *Autoencoders for semivisible jet detection*, *JHEP* **02** (2022) 074, [`2112.02864`].

[470] M. Farina, Y. Nakai and D. Shih, *Searching for New Physics with Deep Autoencoders*, *Phys. Rev. D* **101** (2020) 075021, [`1808.08992`].

[471] T. Heimel, G. Kasieczka, T. Plehn and J. M. Thompson, *QCD or What?*, *SciPost Phys.* **6** (2019) 030, [`1808.08979`].

[472] T. S. Roy and A. H. Vijay, *A robust anomaly finder based on autoencoders*, `1903.02032`.

[473] C. K. Khosa and V. Sanz, *Anomaly Awareness*, *SciPost Phys.* **15** (2023) 053, [`2007.14462`].

[474] T. Finke, M. Krämer, A. Morandini, A. Mück and I. Oleksiyuk, *Autoencoders for unsupervised anomaly detection in high energy physics*, *JHEP* **06** (2021) 161, [2104.09051].

[475] J. Cogan, M. Kagan, E. Strauss and A. Schwartzman, *Jet-Images: Computer Vision Inspired Techniques for Jet Tagging*, *JHEP* **02** (2015) 118, [1407.5675].

[476] L. de Oliveira, M. Kagan, L. Mackey, B. Nachman and A. Schwartzman, *Jet-images — deep learning edition*, *JHEP* **07** (2016) 069, [1511.05190].

[477] B. Andersson, G. Gustafson, L. Lonnblad and U. Pettersson, *Coherence Effects in Deep Inelastic Scattering*, *Z. Phys. C* **43** (1989) 625.

[478] A. Lifson, G. P. Salam and G. Soyez, *Calculating the primary Lund Jet Plane density*, *JHEP* **10** (2020) 170, [2007.06578].

[479] Y. Iiyama et al., *Distance-Weighted Graph Neural Networks on FPGAs for Real-Time Particle Reconstruction in High Energy Physics*, *Front. Big Data* **3** (2020) 598927, [2008.03601].

[480] X. Ju and B. Nachman, *Supervised Jet Clustering with Graph Neural Networks for Lorentz Boosted Bosons*, *Phys. Rev. D* **102** (2020) 075014, [2008.06064].

[481] G. Kasieczka, B. Nachman, D. Shih, O. Amram, A. Andreassen, K. Benkendorfer et al., *The lhc olympics 2020: A community challenge for anomaly detection in high energy physics*, 2101.08320.

[482] T. N. Kipf and M. Welling, *Variational graph auto-encoders*, 1611.07308.

[483] P. V. Tran, *Learning to make predictions on graphs with autoencoders*, in *2018 IEEE 5th international conference on data science and advanced analytics (DSAA)*, pp. 237–245, IEEE, 2018. 1802.08352.

[484] G. Salha, R. Hennequin and M. Vazirgiannis, *Simple and effective graph autoencoders with one-hop linear models*, 2001.07614.

[485] S. Pan, R. Hu, G. Long, J. Jiang, L. Yao and C. Zhang, *Adversarially regularized graph autoencoder for graph embedding*, 1802.04407.

[486] J. Park, M. Lee, H. J. Chang, K. Lee and J. Y. Choi, *Symmetric graph convolutional autoencoder for unsupervised graph representation learning*, in *Proceedings of the*

IEEE/CVF International Conference on Computer Vision, pp. 6519–6528, 2019. `1908.02441`.

[487] B. M. Dillon, T. Plehn, C. Sauer and P. Sorrenson, *Better Latent Spaces for Better Autoencoders*, *SciPost Phys.* **11** (2021) 061, [`2104.08291`].

[488] ATLAS collaboration, *Performance of shower deconstruction in ATLAS*, ATLAS-CONF-2014-003, (2014).

[489] S. Catani, Y. L. Dokshitzer, M. Olsson, G. Turnock and B. R. Webber, *New clustering algorithm for multi - jet cross-sections in e+ e- annihilation*, *Phys. Lett. B* **269** (1991) 432–438.

[490] B. M. Dillon, D. A. Faroughy, J. F. Kamenik and M. Szewc, *Learning the latent structure of collider events*, *Journal of High Energy Physics* **2020** (Oct, 2020) .

[491] B. Bortolato, B. M. Dillon, J. F. Kamenik and A. Smolkovič, *Bump hunting in latent space*, `2103.06595`.

[492] B. M. Dillon, T. Plehn, C. Sauer and P. Sorrenson, *Better latent spaces for better autoencoders*, `2104.08291`.

[493] D. P. Kingma and M. Welling, *Auto-encoding variational bayes*, `1312.6114`.

[494] A. Makhzani, J. Shlens, N. Jaitly, I. Goodfellow and B. Frey, *Adversarial autoencoders*, `1511.05644`.

[495] G. Patrini, R. van den Berg, P. Forré, M. Carioni, S. Bhargav, M. Welling et al., *Sinkhorn autoencoders*, `1810.01118`.